UNDERWATER ACOUSTIC SIGNAL PROCESSING AND ITS APPLICATIONS

By

KEXIN ZHAO

A DISSERTATION PRESENTED TO THE GRADUATE SCHOOL
OF THE UNIVERSITY OF FLORIDA IN PARTIAL FULFILLMENT
OF THE REQUIREMENTS FOR THE DEGREE OF
DOCTOR OF PHILOSOPHY

UNIVERSITY OF FLORIDA

2014

© 2014 Kexin Zhao

I dedicate this work to my Mother, Ling Cao, and my fiancée, Yixue Zhang, without them this would have been impossible for me.

ACKNOWLEDGMENTS

First and foremost, I would like to express my deepest appreciation to my advisor, Dr. Jian Li of the Electrical and Computer Engineering Department, who has led me throughout my PhD training with her patience, great knowledge, and continuous encouragement. It has been an exceptional experience to participate in the underwater acoustic communication and the active sonar projects. Without her guidance and persistent help this dissertation would not have been possible.

I acknowledge my committee members at University of Florida: Dr. Mingzhou Ding, Dr. Tan Wong, and Dr. Jenshan Lin. I am truly thankful for their time and efforts that they spent on my dissertation.

I am truly grateful to have a nice group of fellow students at Dr. Li's lab. I highly appreciate all the help that I received from my lab members during my time at University of Florida. Research would have been much less colorful without them.

Last but not least, I am deeply indebted to my family, especially my mother. They have provided me with immense understanding and support all these years. This dissertation is dedicated to them.

TABLE OF CONTENTS

page

ACKNOWLEDGMENTS 4

LIST OF TABLES 7

LIST OF FIGURES 8

ABSTRACT 10

CHAPTER

1 INTRODUCTION 12

1.1 Challenges of UAC 13
1.2 Challenges of Active Sonar Systems 14
1.3 Notation 16

2 ENHANCED MOBILE MULTI-INPUT MULTI-OUTPUT UAC 22

2.1 System Outline 24
2.2 Double-Selective Channel with Doppler Scaling Effects 26
2.2.1 Channel Model 26
2.2.2 Temporal Resampling 28
2.2.3 Resampling Factor Estimation 28
2.3 Channel Estimation 29
2.3.1 Training-Directed Mode 29
2.3.2 Decision-Directed Mode 31
2.3.3 Channel Estimation Algorithm: GoSLIM 32
2.3.4 Channel Estimation Algorithm: GoSLIM-V 35
2.3.5 Complexity Analysis 36
2.4 Symbol Detection 37
2.4.1 Problem formulation 38
2.4.2 Phase Compensation 39
2.4.3 LMMSE Based Soft-Input Soft-Output Equalizer 40
2.4.3.1 *A priori* LLR pre-processor 40
2.4.3.2 LMMSE filtering 41
2.4.3.3 *A posteriori* LLR generator 43
2.4.4 Low-Complexity Approximate LMMSE Filtering 44
2.5 Numerical and Experimental Results 45
2.5.1 Numerical Results 45
2.5.2 MACE10 In-Water Experimentation Results 47
2.5.2.1 Experiment specifics 47
2.5.2.2 Performance evaluation 49

3 ENHANCED MULTISTATIC ACTIVE SONAR SIGNAL PROCESSING 64
3.1 System Description and Problem Formulation 66
3.2 Proposed Algorithms 67
3.2.1 Range-Doppler Imaging 68
3.2.1.1 Imaging problem formulation 68
3.2.1.2 Receiver filter for range-Doppler imaging 70
3.2.2 Generalized K-Means Clustering (GKC) Association Method 74
3.2.3 EXIP-WLS Method for Target Position Estimation 77
3.2.4 EXIP-WLS Method for Target Velocity Estimation 80
3.3 Simulation Results 82
3.3.1 Range-Doppler Imaging Results 83
3.3.2 Target Parameter Estimation Results 83
4 WIDEBAND SOURCE LOCALIZATION USING SLIM 91
4.1 Data Model 94
4.2 The Wideband SLIM Algorithms 96
4.2.1 WB-SLIM-0 96
4.2.2 WB-SLIM-1 98
4.2.3 Discussion 99
4.3 RELAX 100
4.4 Numerical Examples 102
5 CONCLUSIONS AND FUTURE WORK 112
APPENDIX
A THE DERIVATION OF THE DOPPLER SCALING FACTOR 115
B THE DERIVATION OF THE WEIGHT MATRIX 116
REFERENCES 118
BIOGRAPHICAL SKETCH 127

LIST OF TABLES

Table page

2-1 Coded BER results obtained by GoSLIM and GoSLIM-V 53

2-2 Complexity comparison (in s) between GoSLIM and GoSLIM-V 53

2-3 A summary of the performance of the three detection schemes 54

2-4 The average coded BER obtained by Exact LMMSE Turbo and Approximate LMMSE Turbo 55

3-1 The noise power and the norm of the target reflection coefficients 85

3-2 System parameters 85

3-3 RMSE of Parameter Estimates Using ULS and EXIP-WLS 85

4-1 WB-SLIM algorithms 110

4-2 The RELAX algorithm 111

LIST OF FIGURES

Figure page

1-1 Absorption coefficient versus frequency 18

1-2 Underwater channel impulse response (CIR) example 19

1-3 Scattering functions obtained at two different conditions 20

1-4 Normalized CIR evolution over approximately a one-minite period 21

2-1 An $N \times M$ MIMO UAC system 53

2-2 The structure of the LMMSE based soft-input soft-output equalizer 56

2-3 Simulation averaged over 500 Monte-Carlo trials 56

2-4 The structure of the package used in the MACE10 experiment 57

2-5 The structure of the transmitted symbols for the 4×12 MIMO BLAST scheme used in MACE10 57

2-6 The superimposed modulus of the CIR estimates 58

2-7 The effect of resampling 59

2-8 The relative speed between the transmitter and receiver array given by GPS and estimated during the temporal resampling stage 59

2-9 Doppler frequency evolution of the 1^{st} packet in epoch "E018" obtained by GoSLIM and GoSLIM-V 60

2-10 CIR estimation comparison between GoSLIM and GoSLIM-V 61

2-11 Grayscale mascot obtained from GoSLIM and GoSLIM-V 62

2-12 Grayscale mascot obtained from RELAX-BLAST and Turbo equalization 63

2-13 The LLR soft information about the source bits at the output of the decoder . . 63

3-1 The simulation geometry 86

3-2 A generic active sonar scenario 87

3-3 Description of the association problem 88

3-4 Range-Doppler images obtained at the first receiver 89

3-5 Range-Doppler images obtained at the second receiver 90

4-1 Spatial pseudo spectra obtained with a scalar sensor array 106

4-2 Spatial pseudo spectra obtained with a vector sensor array 107
4-3 Spatial pseudo spectra in the case of a weak source 108
4-4 Performance enhancement using RELAX 109
4-5 Empirical failure rate and RMSEs versus SNR 109

Abstract of Dissertation Presented to the Graduate School
of the University of Florida in Partial Fulfillment of the
Requirements for the Degree of Doctor of Philosophy

UNDERWATER ACOUSTIC SIGNAL PROCESSING AND ITS APPLICATIONS

By

Kexin Zhao

May 2014

Chair: Jian Li
Major: Electrical and Computer Engineering

Underwater acoustic signal processing has various applications in the underwater sensing systems, including the underwater acoustic communication (UAC) system and the active sonar system. A well-designed UAC system can achieve reliable and high data-rate communication to facilitate the operation of submarines, undersea sensors, and unmanned undersea vehicles (UUVs) while active sonar system demands effective and efficient signal processing techniques to accurately detect, localize, and even track the target of interest. The focus of this dissertation is to use the appropriate signal processing techniques to design such UAC and active sonar systems.

For the former, we focus on designing a mobile multi-input multi-output (MIMO) UAC system over double-selective channels subject to both inter-symbol interference and Doppler scaling effects. Temporal resampling is implemented to effectively convert the Doppler scaling effects to Doppler frequency shifts. By simplifying the assumption on the Doppler frequency shifts imposed on the channel taps across all the transmitter and receiver pairs, two sparse channel estimation algorithms, both as an extension of the original sparse learning via iterative minimization (SLIM) method, are proposed for channel estimation. Regarding symbol detection, we employ Turbo equalization and propose a fast implementation of the standard Turbo equalizer for retrieving the transmitted signal. The effectiveness of the considered mobile MIMO UAC scheme is

demonstrated using both simulated data and measurements recently acquired during the MACE10 in-water experiment.

For the latter, we consider a multistatic active sonar system that employs multiple stationary transmitters and receivers. Two signal processing aspects related to such a system design are addressed, namely target range-Doppler imaging and target parameter estimation. To enhance the range-Doppler imaging performance, a hybrid dense-sparse method is proposed to improve resolution and reduce sidelobe levels simultaneously while maintaining high accuracy. In the presence of multiple targets, each peak of the range-Doppler images need to be associated with a specified target before the target parameter estimation. To efficiently solve this problem, we develop a generalized K-Means clustering (GKC) method, which iteratively assigns peaks to targets and then estimates the target parameters based on the current association pattern. Moreover, based on fact that different transmitter-receiver pairs have different reflection coefficients, we develop a weighted least-squares method where the target parameters are refined in an iterative manner using weighting. Note that if each of the receivers is equipped with a large array that can provide accurate angle estimates of the targets, the peak association problem becomes an easy problem or even disappears entirely. For such case, the active sonar system demands an advanced source localization method. However, most existing techniques are developed under the narrowband assumption, which becomes invalid due to the nature of the sonar application. We thus develop two extensions of the SLIM algorithm to solve the wideband source localization problem, which will be demonstrated to provide satisfactory performance.

CHAPTER 1
INTRODUCTION

Underwater acoustic signal processing has various applications in the underwater sensing systems, including the UAC system and the active sonar system. In a simple UAC system, the transmitter sends a probing sequence into the underwater medium and by analyzing the measurement at the receiver, we can determine the properties of the acoustic channel via channel estimation. Similarly but still differently, in an active sonar system, the probing sequence is transmitted toward an area of interest and a target could reflect a fraction of the waveform to the direction of the receiver. This fraction of signal facilitates the receiver's ability to detect potential targets via range-Doppler imaging. The focus of this work is how we apply various signal processing techniques to solve the problem that we encounter in the receiver design of both an UAC system and an active sonar system.

Water forms a major part of the surface of the earth and enormous attempts have been made to explore the underwater environment. The advances in techniques during the past several decades have led to various underwater activities, including harbor monitoring and the exploration of the ocean. These tasks necessitate the employment of the underwater sensor networks and a reliable UAC is essential to ensure good communication between those sensor nodes. As we know, water is more suitable for acoustic waves to transmit than the electromagnetic waves. In contrast to well developed radio communication systems which already impact our everyday life, UAC is still in the experiment stage largely due to its various challenges. Section 1.1 will describe four main challenges. Similarly, the active sonar system has many applications and the challenges encountered are no less than those for the UAC system. Section 1.2 will briefly review the three major challenges. The notations of this whole dissertation is listed in Section 1.3.

1.1 Challenges of UAC

One of the main properties of the acoustic channel is that the absorption rate increases as the frequency of the signal rises [1]. The relation between absorption coefficient and the signal frequency can be found in Figure 1-1. Because of the severe absorption at high frequency, the power of a signal with frequency 120 k Hz will drop by almost 40 dB after an 1 km propagation. Consequently, the power of the corresponding received measurements could be very weak. To address this problem, limited bandwidth is adopted in typical UAC systems [1]. Such scarcely available bandwidth imposes an upper bound on the attainable symbol rate. Therefore, the pursuit of high data rate in UAC leverages the multi-input multi-output (MIMO) scheme, which offers increased data rates compared to its single-input counterpart [2].

The transmitted waveform can arrive at the receiver via multiple paths [3]. Figure 1-2A demonstrates a simple acoustic channel characterized by a direct path, a bottom-reflected path, and a surface-reflected path. Practical underwater channel is usually much more complicated than this one due to the presence of more reflection combinations [3]. Such multipath propagation along with the low underwater sound propagation speed results in large delay spread. The difference in the propagation time between the earliest and latest arrivals could span tens to hundreds of symbol periods, which translates into long channel impulse response (CIR) and severe inter-symbol interference (ISI) at the receiver side. Figure 1-2B shows a practical CIR estimate of length 80. Symbol detection in a MIMO setup is cumbersome because MIMO scheme introduces interferences across all the transmitters in addition to the presence of the ISI effects.

Besides the long delay spread, UAC channels also suffer from the Doppler effects [3, 4]. The presence of Doppler effects, owing to the relative motions between the transmitter and receiver platforms and the dynamic underwater acoustic medium, induces temporal scaling (stretching or compression) to the transmitted signals.

Doppler-induced scaling effects impair the reliability of UAC, especially in the case of a phase-coherent detection scheme. A preferable tool for characterizing a double spreading channel is the scattering function (SF), which decouples the acoustic channel into a bank of paths that experience different delays and Doppler frequencies [5]. Two SFs from different sea environment are shown in Figure 1-3. For the Arctic Ocean case as shown in Figure 1-3A, both main paths are centered around 0 Hz, which suggests that this channel experiences negligible Doppler effects. In comparison for the Bahamas windy weather case, Figure 1-3B shows that the two main paths suffer from severe Doppler effects.

The UAC channel is also quickly varying over time. Figure 1-4 shows an evolution of a practical CIR. We can see from Figure 1-4 that the channel taps after 4 ms are significantly variant over time. Hence such time-varying property only allows a short coherence processing time [6–9].

Chapter 2 focuses on single-carrier UAC system. We provide a detailed mobile MIMO UAC system design by presenting techniques for accurate temporal resampling, proper channel modeling, effective and efficient channel estimation and symbol detection. The effectiveness of the proposed mobile MIMO UAC system is verified using both numerical and experimental results.

1.2 Challenges of Active Sonar Systems

The final goal of an active sonar system is to detect, localize, and even track the potential targets. The first step to achieve this goal is to form range-Doppler images based on the received measurements and the know transmitted probing sequences. We can obtain the range and Doppler information from the dominant peaks of the range-Doppler images and then proceed to estimation the target parameters. One standard receiver design for the range-Doppler imaging application is the commonly used matched filter, which essentially correlates the received signal with the transmitted one. However, when severe interferences are present (this is quite normal for a

multistatic active sonar application), the multiple simultaneously transmitted probing sequences act as interferences to one another, making the matched filter based receiver ineffective. Therefore, it is necessary to design more advanced adaptive receiver filters capable of providing range-Doppler images with both low sidelobe levels and high accuracy.

In the presence of multiple targets in the field of view, once the multistatic range-Doppler images are available, we first need to determine the number of the targets in the area of interest and solve the target association problem before we can proceed with the target parameter estimation. The association approach aims to determine a proper one-to-one correspondence between the targets and the peak locations of each range-Doppler image. The brute-force association is applicable only when the numbers of transmitters, receivers, and targets are small; otherwise, the computational complexity will be too high to implement. Thus such application demands an efficient and effective target association approach and one that simultaneously deals with the target association problem and the target position estimation challenge is preferred.

After the association procedure, we can proceed to estimate the target parameters based on the range and Doppler estimates already obtained and assigned to each target. One standard approach would be using the quasi-Newton method (a.k.a. Gauss or Gauss-Newton interpolation) via iterative linearization. More specifically, the quasi-Newton method makes use of the Taylor expansion to approximate a collection of nonlinear algebraic position equations as linear ones, and refines the target position estimate in an iterative manner. Being conceptually simple and computationally attractive, the quasi-Newton method has become a standard algorithm implemented on the global positioning system (GPS) devices for the end user. Once the target position is available, its velocity is determined by solving a least-squares (LS) fitting problem. However, this approach treat the range and Doppler estimates equally while

estimating the target parameters despite the fact that different targets have different reflection coefficients. A preferable way to address this problem is to assign different weights to the range and Doppler estimates corresponding to different targets in order to enhance the estimation accuracy.

Chapter 3 focuses on a multistatic active sonar system. We provide thorough investigation of the sonar system design by providing a detailed treatment of every step involved in the receiver design from range-Doppler imaging to target parameter estimation. This is done by presenting approaches for range-Doppler imaging with improved resolution and highly suppressed sidelobe levels, efficient target association scheme that incorporates the target location estimation, and effective target parameter estimation with improved accuracy using calculated weights. Simulation results validate the effectiveness of the proposed overall receiver design for a multistatic active sonar system.

Note that if each of the receivers is equipped with a large array that can provide accurate angle estimates of the targets, the peak association problem becomes an easy problem or even disappears entirely. For such case, the active sonar system demands an advanced source localization method. However, most existing techniques are developed under the narrowband assumption, which becomes invalid due to the nature of the sonar application. Hence in Chapter 4, we develop two extensions of the SLIM algorithm to solve the wideband source localization problem, which will be demonstrated to provide satisfactory performance.

1.3 Notation

Vectors and matrices are denoted by boldface lowercase and uppercase letters, respectively, $\|\cdot\|$ denotes the Euclidean norm of a vector, $|\cdot|$ is the modulus and $(\cdot)^*$ is the complex conjugate of a scalar. $(\cdot)^T$ and $(\cdot)^H$ denote the transpose and conjugate transpose, respectively, of a matrix or vector, $\mathbf{I}$ denotes an identity matrix of appropriate dimension, and $\hat{\mathbf{x}}$ denotes the estimate of $\mathbf{x}$. $\mathrm{diag}\,(\mathbf{v})$ represents a diagonal matrix in

which the elements of $\mathbf{v}$ are on the diagonal. $\mathrm{Re}(\cdot)$ and $\mathrm{Im}(\cdot)$ represent the real and the imaginary components of a complex-valued scalar, respectively. $\mathbf{A} \otimes \mathbf{B}$ denotes the Kronecker product of two matrices $\mathbf{A}$ and $\mathbf{B}$. Other mathematical symbols are defined after their first appearance.

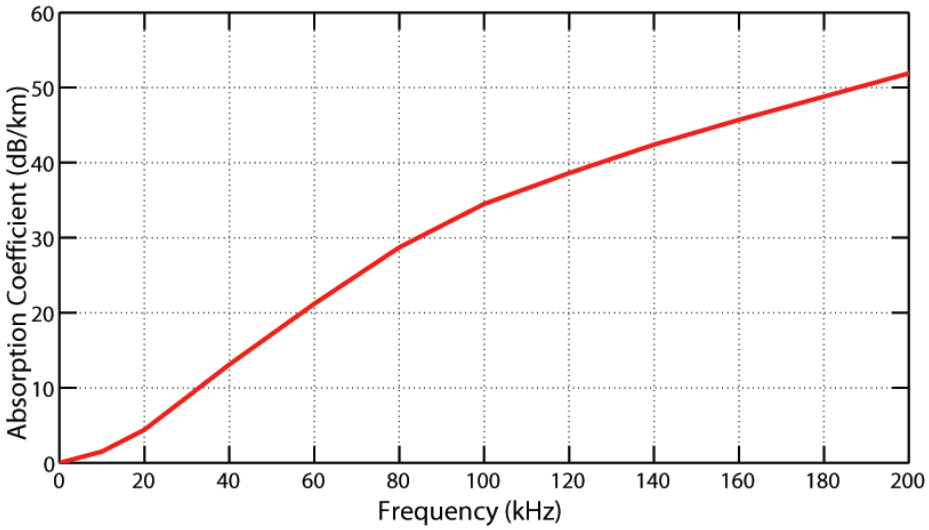

Figure 1-1. Absorption coefficient versus frequency. Copyright image courtesy of [1].

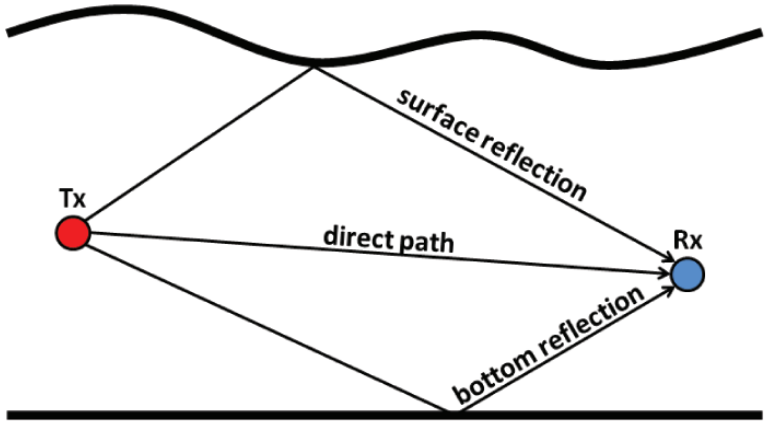

A

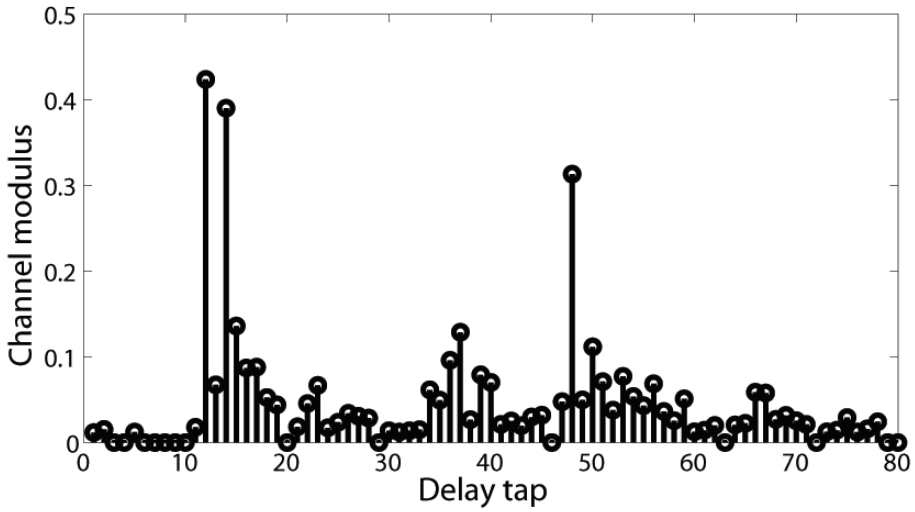

B

Figure 1-2. Underwater channel impulse response (CIR) example. A) An underwater acoustic channel with three multipaths. B) A practical CIR with 80 channel taps.

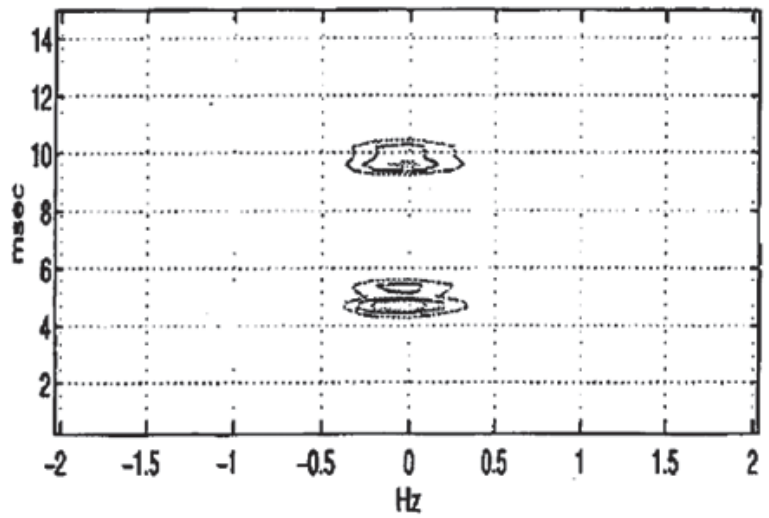

A

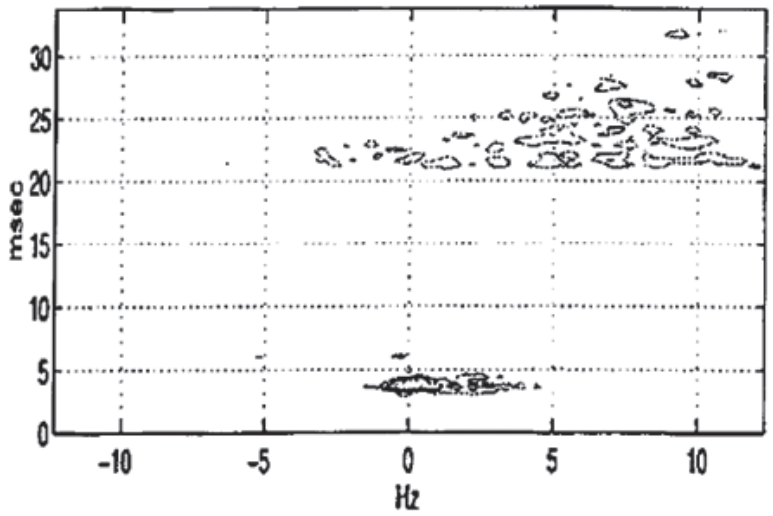

B

Figure 1-3. Scattering functions obtained at two different conditions. A) Arctic environment with frozen sea surface. B) Bahama Islands on a windy day. Copyright image courtesy of [10].

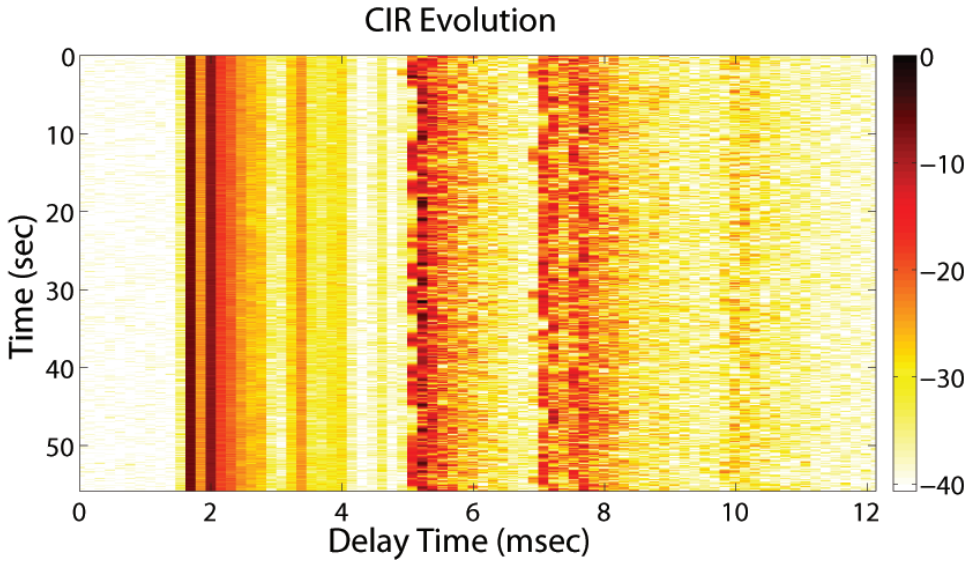

Figure 1-4. Normalized CIR evolution over approximately a one-minite period.

CHAPTER 2
ENHANCED MOBILE MULTI-INPUT MULTI-OUTPUT UAC

This chapter focuses on effective mobile MIMO UAC over double-selective acoustic channels suffering from both ISI and Doppler scaling effects. Converting the double-selective channel into an ISI channel via temporal resampling is an effective way to tackle mobile UAC difficulties [11]. Although the Doppler scaling effects can be largely mitigated via such a temporal resampling process, the residual Doppler still causes frequency shift on the received measurements. Coherent UAC requires the receiver to acquire knowledge of the underlying channel after temporal resampling via channel estimation [2]. Channel estimation could be conducted either in the training-directed mode, using known training sequences, or in the decision-directed mode, using the detected payload symbols [12–15]. A preferable tool to characterize a channel subject to both ISI and Doppler frequency shift is the scattering function (SF), which essentially decouples the acoustic channel into a bank of paths that experience different delays and Doppler frequencies [5]. The major concern in SF-based channel estimation is that the problem becomes over parameterized with too many degrees of freedom. It is practically more beneficial to look for a channel model with the smallest number of parameters, but one that still sufficiently reflects the defining characteristics of the acoustic channel of interest. Along this line of thought, we assume that at each receiver, the channel taps for all the transmitters experience the same Doppler frequency, but different receivers experience different Doppler shifts. The number of unknowns in the frequency dimension, as a consequence, is significantly reduced. Accordingly, we propose the generalization of the sparse learning via iterative minimization (GoSLIM) algorithm to estimate the CIRs and the underlying Doppler frequency in a joint manner.

The aforementioned channel model is further simplified by assuming that the channel taps for all the transmitter and receiver pairs experience the same Doppler frequency. As a consequence, the impact of the Doppler frequency shift on the received

measurements across all the receivers is taken into account through one unknown common frequency. Accordingly, a variation of GoSLIM, referred to as GoSLIM-V (V stands for variation), is also proposed for channel estimation. Like GoSLIM, GoSLIM-V addresses sparsity through a hierarchical Bayesian model, and because GoSLIM-V is user parameter free, it is easy to use in practical applications. We will demonstrate via experimental results that the employment of GoSLIM-V not only reduces the overall complexity in the channel estimation stage, but also slightly improves the detection performance compared to its GoSLIM counterpart.

Following the channel estimation is the design of the detection scheme for extracting the transmitted signals. The channel-induced phase shift should be first compensated out using the Doppler frequency estimate [10, 16, 17]. Such phase compensation task, along with the aforementioned temporal resampling process, effectively converts a double-selective channel subject to both Doppler scaling effects and ISI to an ISI channel, which allows for the employment of various equalization techniques that can effectively combat ISI. We use a linear minimum mean-squared error (LMMSE) based filter for symbol detection. In a MIMO setup, on top of ISI, multiple simultaneously transmitted signals act as interferences to one another. Therefore, interference cancellation scheme also plays a critical role in the overall detection performance. A hard decision based interference cancellation scheme, including vertical BLAST (V-BLAST) [17–19] and RELAX-BLAST [12], subtracts out the hard decisions of detected signals from the received measurements to aid the detection of the remaining signals. By combining V-BLAST with the cyclic principle of the RELAX algorithm [20], RELAX-BLAST provides superior detection performance over V-BLAST at the cost of slightly increased complexities [12, 13, 16, 21].

The detection performance can be further enhanced by employing a soft interference cancellation scheme, including Turbo equalization [22–25]. For a receiver employing Turbo equalization, both the equalizer and decoder involved are configured as soft-input

soft-output. The detection performance improves as the soft information cycles between the equalizer and decoder. The main drawback of the Turbo equalization scheme is the increased computational complexity compared to its hard decision based counterparts. To address this problem, we propose a low complexity approximation of soft-input soft-output equalizer. We will show via numerical and experimental examples that the employment of the proposed approximate equalizer enjoys a computational complexity comparable to RELAX-BLAST and provides only slightly degraded detection performance compared to a directly implemented equalizer.

The rest of this chapter is organized as follows. Section 2.1 presents a system outline. Section 2.2 describes a model for the acoustic channel subject to both ISI and Doppler scaling effects and reviews the temporal resampling procedure. Section 2.3 formulates the channel estimation problem in both training-directed and decision-directed modes and then introduces both GoSLIM and GoSLIM-V as the channel estimation algorithm. Section 2.4 first formulates the symbol detection problem, and then details the LMMSE based soft-input soft-output equalizer and its low complexity approximation. Section 2.5 presents the simulation results of the Turbo equalization scheme, followed by the experimental results obtained from analyzing the MACE10 in-water measured data.

2.1 System Outline

Consider an $N \times M$ mobile MIMO UAC system equipped with N transmit transducers and M receive hydrophones. The transmitted payload sequences are divided into multiple blocks, each of which is encoded separately. Figure 2-1A demonstrates the construction of a single payload symbol block (the construction of other blocks follows the same procedure). Denote $a(k) \in \{0, 1\}$ as the k^{th} source bit for $k = 1, \ldots, NK$. $\{a(k)\}_{k=1}^{NK}$ are first fed into a $1/2$ rate convolutional encoder with generator polynomials $(1\ 0\ 0\ 1\ 1)$ and $(1\ 1\ 0\ 1\ 1)$. The encoded bits $\{b(k)\}_{k=1}^{2NK}$ are then passed to a random interleaver, followed by a quadrature phase-shift keying (QPSK) modulation using Gray

code mapping. In Figure 2-1, interleaver and deinterleaver modules are represented by Π and Π^{-1}, respectively. Next, the so-obtained QPSK payload symbols $\{x(k)\}_{k=1}^{NK}$ are demultiplexed into the N payload blocks, each consisting of K symbols, across the N transmitters in a round-robin fashion (this is where the "DEMUX" module in Figure 2-1A comes into play). More specifically, in our design, $x(n+(q-1)N)$ corresponds to the q^{th} symbol sent by the n^{th} transmitter, denoted as $x_n(q)$, for $q = 1, \ldots, K$ and $n = 1, \ldots, N$. Accordingly, we denote $c_n(2q-1)$ and $c_n(2q)$ as the two consecutive interleaved bits in $\{c(k)\}_{k=1}^{2NK}$ that map to $x_n(q)$ according to the formula given below:

$$x_n(q) = \frac{1}{\sqrt{2}}\left[j(-1)^{c_n(2q-1)} + (-1)^{c_n(2q)}\right], \quad q = 1, \ldots, K, \quad n = 1, \ldots, N. \tag{2–1}$$

Since $c(k) \in \{0, 1\}$, the support of $\{x_n(k)\}$ is a 4-element alphabet set $\mathcal{S} = \{(\pm j \pm 1)/\sqrt{2}\}$.

The structure of a receiver employing a Turbo equalization scheme is shown in Figure 2-1B. The measurements acquired by the M receive hydrophones are first resampled, followed by channel estimation and phase compensation. After phase compensation, the double-selective channel is converted to an ISI channel, and the Turbo equalization scheme is employed herein to retrieve the transmitted information. The superior detection performance promised by Turbo equalization is mainly due to its mechanism of cycling soft information between the equalizer and the decoder [22, 26, 27]. Accordingly, Turbo equalization consists of two key modules, namely a soft-input soft-output equalizer and a soft-input soft-output decoder [28, 29]. The soft information of a generic bit $a \in \{0, 1\}$, commonly known as the log-likelihood ratio (LLR), is defined as:

$$L(a) = \ln \frac{P(a=0)}{P(a=1)}, \tag{2–2}$$

where $P(a = 0) \in [0, 1]$ represents the probability of a being 0. As shown in Figure 2-1B, the multiplexed and deinterleaved version of $\{L_e(c_n(k))\}_{n=1,k=1}^{N,2K}$, the *a posteriori extrinsic* LLR generated by the equalizer, forms the *a priori* inputs $\{L_e(b(k))\}_{k=1}^{2NK}$ to

the decoder. Conversely, the interleaved and demultiplexed version of $\{L_d(b(k))\}_{k=1}^{2NK}$, the *a posteriori extrinsic* LLR generated by the decoder, serves as *a priori* information to the equalizer. The subscript e or d reminds us that the LLRs are generated by the equalizer or the decoder, respectively. The soft information is cycled between the equalizer and the decoder multiple times before making hard decisions on the source bits. Note that the interleaver and deinterleaver involved at the transmitter and receiver have the same structure, whereas the "DEMUX" module inside the dashed rectangle in Figure 2-1B is different from that in Figure 2-1A in the sense that the former and the latter demultiplex, respectively, the soft information $\{L_d(c(k))\}_{k=1}^{2NK}$ and QPSK symbols $\{x(k)\}_{k=1}^{NK}$. Once $\{\tilde{a}(k)\}_{k=1}^{NK}$, the hard decisions on the source bits, are available, we follow the steps in the symbol generation process shown in Figure 2-1A: $\{\tilde{a}(k)\}_{k=1}^{NK}$ are fed into the convolutional encoder, followed by random interleaving, QPSK mapping, and demultiplexing. This way, an error free decoding ensures a perfect recovery of the transmitted QPSK symbols $\{x_n(k)\}_{n=1,k=1}^{N\ K}$. The recovered payload symbols will be used in the decision-directed channel estimation stage; see Figure 2-1B.

2.2 Double-Selective Channel with Doppler Scaling Effects

In this section, we start with the modeling of the double-selective channel suffering from both ISI and Doppler scaling effects. Then we describe the temporal resampling procedure to mitigate the Doppler scaling effects. After that, we provide a practical approach to estimate the Doppler scaling factor.

2.2.1 Channel Model

By adopting a single-carrier communication scheme, at the n^{th} transmitter, the continuous baseband signal $x_n(t)$ (generated by passing the discrete payload symbols $\{x_n(k)\}$ to a pulse shaping filer) and its corresponding frequency modulated signal $\breve{x}_n(t)$ are related through

$$\breve{x}_n(t) = \mathrm{Re}\{x_n(t)e^{j2\pi f_c t}\}, \quad n = 1, \ldots, N, \tag{2–3}$$

where f_c represents the carrier frequency. For simplicity, the pulse shaping filter, frequency modulation, and real component extraction operation are not shown in Figure 2-1A.

Due to multipath effects, the actual transmitted signals $\{\breve{x}_n(t)\}_{n=1}^{N}$ can reach the receive hydrophones via different propagation paths with different delays. Herein, the underlying acoustic channel between each transmitter and receiver pair is characterized by R resolved paths. The r^{th} path between the n^{th} transmitter and m^{th} receiver pair ($r = 1, \ldots, R$, $n = 1, \ldots, N$, and $M = 1, \ldots, M$) will affect the transmitted signal $\breve{x}_n(t)$ in three aspects, namely amplitude attenuation, Doppler scaling, and delay, which are denoted, respectively, by three real-valued scalars $\kappa_{n,m}(r)$, $\alpha_{n,m}(r)$, and $\tau_{n,m}(r)$. The signal transmitted via the r^{th} path and acquired by the m^{th} receiver can be written as $\kappa_{n,m}(r) \cdot \breve{x}_n(\alpha_{n,m}(r)t - \tau_{n,m}(r))$. By taking into account all of the N transducers and R resolved paths, the received signal at the m^{th} hydrophone can be expressed as (for simplicity, the noise term is omitted for the time being):

$$\breve{z}_m(t) = \sum_{n=1}^{N}\sum_{r=1}^{R} \kappa_{n,m}(r) \cdot \breve{x}_n(\alpha_{n,m}(r)t - \tau_{n,m}(r)), \quad m = 1, \ldots, M. \tag{2–4}$$

We assume that the propagation paths for all the transmitter and receiver pairs experience a common Doppler scaling factor and the resolved paths are synchronized among all the transmitter and receiver pairs, i.e., $\alpha_{n,m}(r) = \alpha$ and $\tau_{n,m}(r) = \tau(r)$. (Interested readers are referred to [30] for a detailed treatment of synchronization procedure.) By using these assumptions, (2–4) reduces to:

$$\breve{z}_m(t) = \sum_{n=1}^{N}\sum_{r=1}^{R} \kappa_{n,m}(r) \cdot \breve{x}_n(\alpha t - \tau(r)), \quad m = 1, \ldots, M. \tag{2–5}$$

Substituting (2–3) into (2–5) yields:

$$\breve{z}_m(t) = \mathrm{Re}\left\{ \sum_{n=1}^{N}\sum_{r=1}^{R} \kappa_{n,m}(r) \cdot x_n(\alpha t - \tau(r)) e^{j2\pi f_c(\alpha t - \tau(r))} \right\}. \tag{2–6}$$

2.2.2 Temporal Resampling

By resampling the received measurements $\{\breve{z}_m(t)\}$ using a factor β, the resampled signal $\breve{y}_m(t)$ is given by [11, 31, 32]:

$$\breve{y}_m(t) = \breve{z}_m\left(\frac{t}{\beta}\right). \tag{2–7}$$

Then, the baseband received signal $y_m(t)$, which is related to $\breve{y}_m(t)$ via $\breve{y}_m(t) = \mathrm{Re}\left\{y_m(t)e^{j2\pi f_c t}\right\}$, can be expressed as:

$$y_m(t) = e^{-2j\pi\left(\frac{\beta-\alpha}{\beta}\right)f_c t}\sum_{n=1}^{N}\sum_{r=1}^{R} h_{n,m,r}\cdot x_n\left(\frac{\alpha}{\beta}t-\tau(r)\right), \tag{2–8}$$

where $h_{n,m,r} \triangleq \kappa_{n,m}(r)e^{-j\pi f_c\tau(r)}$ represents the r^{th} channel tap between the n^{th} transmitter and the m^{th} receiver pair, for $r = 1,\ldots,R$, $n = 1,\ldots,N$, and $m = 1,\ldots,M$. It can be readily verified that as long as $\alpha/\beta \approx 1$, we have $x_n\left(\frac{\alpha}{\beta}t-\tau(r)\right) \approx x_n\left(t-\tau(r)\right)$. Accordingly, (2–8) can be approximated as:

$$y_m(t) \approx e^{-2j\pi\left(\frac{\beta-\alpha}{\beta}\right)f_c t}\sum_{n=1}^{N}\sum_{r=1}^{R} h_{n,m,r}\cdot x_n\left(t-\tau(r)\right). \tag{2–9}$$

One observes from (2–9) that effective temporal resampling (meaning $\alpha \approx \beta$) converts the Doppler scaling effects to Doppler frequency shifts with the frequency given below:

$$f = \left(\frac{\beta-\alpha}{\beta}\right)f_c. \tag{2–10}$$

Therefore, the determination of the resampling factor β plays a crucial role in the effective mitigation of the Doppler scaling effects.

2.2.3 Resampling Factor Estimation

We take advantage of the preamble and the postamble of a data packet to estimate β [31, 33] (the structure of a data packet will be discussed in Section 2.5). By cross-correlating the received signal with the known preamble and postamble, the receiver estimates the time duration of a packet $\hat{T}_{rx}$ [11, 34]. By comparing $\hat{T}_{rx}$ with T_{tx}, the duration of the same packet at the transmitter side, the Doppler scaling factor can be

estimated as:

$$\hat{\beta} = \frac{\hat{T}_{rx}}{T_{tx}}. \tag{2–11}$$

Although this method is conceptually simple and easy to implement, its accuracy is sensitive to the signal-to-noise-ratio (SNR).

More accurate Doppler scaling factor estimate can be achieved via channel estimation instead of cross-correlation. Based on the CIRs estimated from the two measurement segments in response to the preamble and postamble, the change in the time duration $\hat{T}_d$ imposed on the packet can be inferred from the tap shift of the principal arrivals of these two CIRs. Then the Doppler scaling factor estimate can be computed as

$$\hat{\beta} = \frac{T_{tx} + \hat{T}_d}{T_{tx}}. \tag{2–12}$$

The $\hat{\beta}$ obtained using (2–12) is more robust against the noise contamination than the one from (2–11). We will show later on in Section 2.5 via the MACE10 in-water experimental data that the method in (2–12) works well in practice.

2.3 Channel Estimation

Since the $\hat{\beta}$ obtained using (2–12) can never be perfectly accurate, after temporal resampling, Doppler frequency shifts (see (2–10)) still exist, although Doppler scaling effects become negligible. We start below with the problem formulation of channel estimation in both training-directed and decision-directed modes [12, 13]. Then, we propose the GoSLIM-V algorithm for jointly estimating the underlying CIRs and Doppler frequency.

In what follows, $\{y_m(t)\}_{m=1}^{M}$ and $\{x_n(t)\}_{n=1}^{N}$ in (2–9) are represented in discrete-time form. Unless otherwise stated, it is assumed that the channel taps for all the $N \times M$ transmitter-receiver pairs experience the same Doppler frequency f.

2.3.1 Training-Directed Mode

The initial task of the receiver is to acquire knowledge of the underlying channel between all transmitter and receiver pairs using the training sequences. By adopting the

cyclic prefix scheme in [2], the training sequence at the n^{th} transmitter ($n = 1, \ldots, N$) is given by

$$\mathbf{x}_n = [\underbrace{x_n(P - L_{\text{CP}} + 1), \ldots, x_n(P)}_{L_{\text{CP}} \text{ prefix symbols}}, \underbrace{x_n(1), x_n(2), \ldots, x_n(P)}_{P \text{ core training symbols}}], \tag{2–13}$$

where $[x_n(1), \ldots, x_n(P)]$ is the core training sequence and the leading L_{CP} symbols form the cyclic prefix. In general, we have $P > L_{\text{CP}} \geq R - 1$. From an amplifier efficiency point of view, it is practically desirable to use unit modulus (unimodular) training sequences, i.e., $|x_n(p)| = 1$ for $n = 1, \ldots, N$ and $p = 1, \ldots, P$.

For MIMO UAC over empirical acoustic channels subject to both ISI and Doppler frequency shifts, the measurement vectors can be written as [5, 35]

$$\mathbf{y}_m = \mathbf{\Lambda}_m \sum_{n=1}^{N} \mathbf{X}_n \mathbf{h}_{n,m} + \mathbf{e}_m, \quad m = 1, \ldots, M, \tag{2–14}$$

where

$$\mathbf{y}_m = [y_m(1), \ldots, y_m(P)]^T, \tag{2–15}$$

contains the P synchronized measured symbols (for instance, $\{y_m(1)\}$ maps to $\{x_n(1)\}$). $\mathbf{X}_n \in \mathbb{C}^{P \times R}$ is given by

$$\mathbf{X}_n = \begin{bmatrix} x_n(1) & x_n(P) & \ldots & x_n(P - R + 2) \\ x_n(2) & x_n(1) & \ldots & x_n(P - R + 3) \\ \vdots & \vdots & \ddots & \vdots \\ x_n(P) & x_n(P - 1) & \ldots & x_n(P - R + 1) \end{bmatrix}, \tag{2–16}$$

where $n = 1, \ldots, N$, and $\mathbf{e}_m$ represents additive noise. In addition,

$$\mathbf{h}_{n,m} = [h_{n,m,1}, \ldots, h_{n,m,R}]^T, \tag{2–17}$$

characterizes the channel of length R between the n^{th} transmitter and the m^{th} receiver for $n = 1, \ldots, N$ and $m = 1, \ldots, M$. Finally, the so-called Doppler shift matrix $\mathbf{\Lambda}_m \in \mathbb{C}^{P \times P}$ in (2–14) has the form:

$$\mathbf{\Lambda}_m = \text{diag}\left(\left[1, e^{-2j\pi f_m T_s}, \ \ldots \ , e^{-2j\pi f_m T_s (P-1)}\right]\right), \tag{2–18}$$

for $m = 1, \ldots, M$, where f_m and T_s represent the Doppler frequency and symbol period, respectively.

The ISI and Doppler shift effects can be viewed separately in (2–14). More specifically, the term $\sum_{n=1}^{N} \mathbf{X}_n \mathbf{h}_{n,m}$ characterizes the combined contributions of N ISI channels, whereas the impact of the Doppler effects on the measurements comes through $\mathbf{\Lambda}_m$ only, which corresponds to the assumption that all the NR CIR taps involved at the m^{th} receiver (recall that we have N transmit transducers and an R-tap channel between each transmitter and receiver pair) experience the same Doppler frequency f_m. The purpose of setting the first diagonal element of $\mathbf{\Lambda}_m$ to 1 is to eliminate ambiguities. In our example, relative to $y_m(1)$, a generic measurement, say $y_m(p)$, experiences a phase shift of $-f_m T_s(p-1)$.

We express (2–14) in a more compact form:

$$\mathbf{y}_m = \mathbf{\Lambda}_m \bar{\mathbf{X}} \mathbf{h}_m + \mathbf{e}_m, \tag{2–19}$$

where $\bar{\mathbf{X}} = [\mathbf{X}_1, \ldots, \mathbf{X}_N]$ and $\mathbf{h}_m = [\mathbf{h}_{1,m}^T, \ldots, \mathbf{h}_{N,m}^T]^T$. Then the training-directed channel estimation reduces to estimating $\mathbf{h}_m$ and f_m from the measurement vector $\mathbf{y}_m$ and known $\bar{\mathbf{X}}$ for $m = 1, \ldots, M$. The subject of synthesizing unimodular training sequences, coupled with the employment of the cyclic prefix scheme, to facilitate ISI channel estimation is treated in [13]. The shifted PeCAN waveforms [36] are used as the training sequences in the MACE10 in-water experimentations.

2.3.2 Decision-Directed Mode

The decision-directed channel estimation problem is only a slight twist of its training-directed counterpart. For the former, we use the previously estimated payload symbols, instead of the training symbols, to estimate the channels. Accordingly, (2–14) can still be used, where

$$\mathbf{y}_m = [y_m(t_i), \ldots, y_m(t_f)]^T, \quad m = 1, \ldots, M, \tag{2–20}$$

contains the measurements at the m^{th} receiver belonging to the time index interval $[t_i, t_f]$, and

$$\mathbf{X}_n = \begin{bmatrix} \hat{x}_n(t_i) & \hat{x}_n(t_i-1) & \dots & \hat{x}_n(t_i-R+1) \\ \hat{x}_n(t_i+1) & \hat{x}_n(t_i) & \dots & \hat{x}_n(t_i-R+2) \\ \vdots & \vdots & \ddots & \vdots \\ \hat{x}_n(t_f) & \hat{x}_n(t_f-1) & \dots & \hat{x}_n(t_f-R+1) \end{bmatrix}, \tag{2–21}$$

for $n = 1, \dots, N$, where $\hat{x}_n(t_i - R + 1)$ and $\hat{x}_n(t_f)$ represent the first and last previously estimated symbols (some of them could be the known training symbols), respectively, used for updating the channel. (For notational simplicity, $\mathbf{X}_n$ is used in both (2–16) and (2–21) to represent two similar but different quantities. The use of $\mathbf{X}_n$, however, should be clear from the context.) The tracking length is represented as $L_{\text{TR}} = t_f - t_i + 1$, i.e., the number of rows of $\mathbf{X}_n$. To conform with the matrix dimensions, the Doppler shift matrix $\mathbf{\Lambda}_m$ now has dimension L_{TR}, constructed as $\mathbf{\Lambda}_m = \text{diag}\left(\left[1, e^{-2j\pi f_m T_s}, \dots, e^{-2j\pi f_m T_s(L_{\text{TR}}-1)}\right]\right)$ for $m = 1, \dots, M$. Similarly to the training-directed mode, the channel estimation problem in the decision-directed mode aims to estimate $\mathbf{h}_m$ and f_m from the measurement vector $\mathbf{y}_m$ and known $\bar{\mathbf{X}}$ formed from the decision-directed $\{\mathbf{X}_n\}_{n=1}^N$ in (2–21), for $m = 1, \dots, M$.

2.3.3 Channel Estimation Algorithm: GoSLIM

The channel estimation algorithm at each receiver, in either training- or decision-directed mode, has the generic form given by (see (2–19))

$$\mathbf{y}_m = \mathbf{\Lambda}_m \bar{\mathbf{X}} \mathbf{h}_m + \mathbf{e}_m, \quad m = 1, \dots, M. \tag{2–22}$$

The noise vector $\mathbf{e}_m$ in (2–22) is assumed to contain circularly symmetric independent and identically distributed complex-valued Gaussian random variables with zero mean and variance η_m, denoted as $\mathbf{e}_m \sim \mathcal{CN}(\mathbf{0}, \eta_m \mathbf{I})$. The problem is then to estimate f_m and $\mathbf{h}_m$ given $\mathbf{y}_m$ and $\bar{\mathbf{X}}$. Channel estimation can be performed at each receiver in parallel. In UAC systems, the channel $\mathbf{h}_m$ is usually sparse, i.e., although it contains NR unknowns, many of them can be approximated as zero [37]. We use the GoSLIM algorithm to solve

this sparse channel estimation problem. Note that since $\mathbf{h}_m$ contains the CIRs for all N transmitters, GoSLIM will estimate them simultaneously.

Consider the following hierarchical Bayesian model:

$$\mathbf{y}_m|\mathbf{h}_m, \mathbf{\Lambda}_m, \eta_m \sim \mathcal{CN}(\mathbf{\Lambda}_m\bar{\mathbf{X}}\mathbf{h}_m, \eta_m\mathbf{I}), \tag{2–23}$$

$$\mathbf{h}_m|\mathbf{p}_m \sim \mathcal{CN}(\mathbf{0}, \mathbf{P}_m), \tag{2–24}$$

where (2–23) follows directly from the assumption $\mathbf{e}_m \sim \mathcal{CN}(\mathbf{0}, \eta_m\mathbf{I})$. Let $p_{n,m,r}$ be the variance of $h_{n,m,r}$ for $n = 1, \ldots, N$, $m = 1, \ldots, M$, and $r = 1, \ldots, R$, and define $\mathbf{p}_{n,m} = [p_{n,m,1}, p_{n,m,2}, \ldots, p_{n,m,R}]^T$ and $\mathbf{p}_m = [\mathbf{p}_{1,m}^T, \mathbf{p}_{2,m}^T, \ldots, \mathbf{p}_{N,m}^T]^T$. Then the covariance matrix $\mathbf{P}_m$ in (2–24) is constructed as $\mathbf{P}_m = \mathrm{diag}(\mathbf{p}_m)$.

Furthermore, by considering a flat prior on f_m, η_m, and $\{p_{n,m,r}\}_{n=1,r=1}^{N,R}$, the channel vector $\mathbf{h}_m$, Doppler frequency f_m, the covariance matrix $\mathbf{P}_m$ (or more precisely, its diagonal elements $\mathbf{p}_m$), and the noise power η_m can be estimated based on the maximum a posteriori criterion (2–25):

$$\max_{\mathbf{h}_m,\mathbf{p}_m,\eta_m,f_m} p(\mathbf{h}_m, \mathbf{p}_m, \eta_m, f_m|\mathbf{y}_m) = \max_{\mathbf{h}_m,\mathbf{p}_m,\eta_m,f_m} p(\mathbf{y}_m|\mathbf{h}_m, \eta_m, f_m)p(\mathbf{h}_m|\mathbf{p}_m) \tag{2–25}$$

By combining (2–23), (2–24), and (2–25), and by taking the negative logarithm of the cost function, the optimization problem formulated in (2–25) becomes (2–26)

$$\min_{\mathbf{h}_m,\mathbf{p}_m,\eta_m,f_m} \left(d_y \log \eta_m + \frac{\left\|\mathbf{y}_m - \mathbf{\Lambda}_m\bar{\mathbf{X}}\mathbf{h}_m\right\|^2}{\eta_m} + \sum_{n=1}^{N}\sum_{r=1}^{R} \log p_{n,m,r} + \sum_{n=1}^{N}\sum_{r=1}^{R} \frac{|h_{n,m,r}|^2}{p_{n,m,r}} \right), \tag{2–26}$$

which can be solved using a cyclic optimization approach: at each iteration, one of the parameter vectors $\mathbf{h}_m$, $\mathbf{p}_m$, η_m, and f_m is updated while keeping the other three fixed. In this way, a single difficult joint optimization problem is divided into four simpler separate subproblems. GoSLIM keeps iterating until a predefined iteration number is reached or a convergence criterion is met. Under mild conditions, the cyclic optimization scheme guarantees that the GoSLIM algorithm converges, at least to a local minimum of (2–26) [38].

The five steps of the GoSLIM algorithm at the t^{th} iteration are outlined below:

1. Given $\mathbf{h}_m^{(t-1)}$, the optimal $\mathbf{P}_m^{(t)}$ that minimizes the cost function in (2–26) is given by:

$$p_{n,m,r}^{(t)} = \left| h_{n,m,r}^{(t-1)} \right|^2, \quad n = 1, \ldots, N, \quad r = 1, \ldots, R. \tag{2–27}$$

For better numerical stability, we set $p_{n,m,r}^{(t)}$ (or equivalently $h_{n,m,r}^{(t)}$) to zero if $p_{n,m,r}^{(t)} < 10^{-15}$.

2. Once $\mathbf{P}_m^{(t)}$ is available, $\mathbf{h}_m^{(t)}$ is obtained as:

$$\mathbf{h}_m^{(t)} = \left[\bar{\mathbf{X}}^H \bar{\mathbf{X}} + \eta_m^{(t-1)} \left(\mathbf{P}_m^{(t)} \right)^{-1} \right]^{-1} \left(\mathbf{\Lambda}_m^{(t-1)} \bar{\mathbf{X}} \right)^H \mathbf{y}_m. \tag{2–28}$$

While inverting $\mathbf{P}_m^{(t)}$, its zero diagonal entries are removed, and the corresponding columns in $\bar{\mathbf{X}}$ are discarded.

3. Next, using the most recently obtained $\mathbf{h}_m^{(t)}$ in (2–28), we estimate the Doppler frequency f_m. For ease of exposition, we denote $z_m^{(t)}(i) = y_m^*(i)\tilde{x}_m^{(t)}(i)$, where $y_m(i)$ and $\tilde{x}_m^{(t)}(i)$ represent, respectively, the i^{th} element of the measurement vector $\mathbf{y}_m$ and $\tilde{\mathbf{x}}_m^{(t)}$ with $\tilde{\mathbf{x}}_m^{(t)} = \bar{\mathbf{X}}\mathbf{h}_m^{(t)}$ for $i = 1, \ldots, d_y$. It is easy to verify that

$$\left\| \mathbf{y}_m - \mathbf{\Lambda}_m \bar{\mathbf{X}} \mathbf{h}_m^{(t)} \right\|^2 = \text{const} - 2\text{Re}\left(\sum_{i=1}^{d_y} z_m^{(t)}(i) e^{-2j\pi f_m T_s (i-1)} \right). \tag{2–29}$$

Since the constant term in (2–29) is not a function of f_m, minimizing the cost function in (2–26) is equivalent to solving

$$f_m^{(t)} = \arg\max_{f_m} \text{Re}\left(\sum_{i=1}^{d_y} z_m^{(t)}(i) e^{-2j\pi f_m T_s (i-1)} \right). \tag{2–30}$$

Since the summation term within the parenthesis above is the discrete-time Fourier transform (DTFT) of the sequence $\{z_m^{(t)}(i)\}_{i=1}^{d_y}$ evaluated at frequency f_m, $f_m^{(t)}$ is obtained as the location of the dominant peak of the real part of the DTFT.

4. Using $\mathbf{h}_m^{(t)}$ and $\mathbf{\Lambda}_m^{(t)}$ most recently obtained in (2–28) and (2–30), respectively, we finally estimate the noise power as:

$$\eta_m^{(t)} = \frac{1}{d_y} \left\| \mathbf{y}_m - \mathbf{\Lambda}_m^{(t)} \bar{\mathbf{X}} \mathbf{h}_m^{(t)} \right\|^2. \tag{2–31}$$

5. Set $t = t + 1$. Go back to Step 1 if t is less than a predefined iteration number, or terminate otherwise.

In the training-directed mode, the channel characteristics in general are not available a priori. In our examples, $\mathbf{h}_m^{(0)}$ is initialized using the standard matched filter, $f_m^{(0)}$ is initialized as 0 and the noise power $\eta_m^{(0)}$ is initialized with a small positive number,

for instance, 10^{-10}. Our empirical experience suggests that the GoSLIM algorithm does not provide significant performance improvements after no more than 15 iterations.

2.3.4 Channel Estimation Algorithm: GoSLIM-V

The channel estimation problem formulated in (2–19), as previously mentioned, corresponds to an assumption that the NR channel taps seen by each receiver experience the same Doppler frequency, but the frequency value could vary at different receive hydrophones. We consider herein a further simplified assumption that the Doppler frequency is the same across M receivers, i.e., $f = f_1 = \cdots = f_M$. (The practical validity of this assumption will be verified by analyzing in-water experimental data in Section 2.5.2.) Accordingly, replacing f_m in (2–18) by f yields a Doppler shift matrix $\bar{\mathbf{\Lambda}}$ that is independent of the receiver index m:

$$\bar{\mathbf{\Lambda}} = \mathrm{diag}\left(\left[1,\, e^{-2j\pi f T_s},\ \ldots\ , e^{-2j\pi f T_s(P-1)}\right]\right). \tag{2–32}$$

Combining (2–19) with (2–32) gives $\mathbf{y}_m = \bar{\mathbf{\Lambda}}\bar{\mathbf{X}}\mathbf{h}_m + \mathbf{e}_m$. Then stacking the measurements from all the receivers follows

$$\mathbf{y} = \mathbf{\Lambda}\mathbf{X}\mathbf{h} + \mathbf{e}, \tag{2–33}$$

where $\mathbf{y} = [\mathbf{y}_1^T, \mathbf{y}_2^T, \ldots, \mathbf{y}_M^T]^T$, $\mathbf{h} = [\mathbf{h}_1^T, \mathbf{h}_2^T, \ldots, \mathbf{h}_M^T]^T$, $\mathbf{e} = [\mathbf{e}_1^T, \mathbf{e}_2^T, \ldots, \mathbf{e}_M^T]^T$, $\mathbf{\Lambda} = \mathbf{I}_{M\times M} \otimes \bar{\mathbf{\Lambda}}$, and $\mathbf{X} = \mathbf{I}_{M\times M} \otimes \bar{\mathbf{X}}$. Then the GoSLIM-V algorithm aims to estimate f and $\mathbf{h}$ given $\mathbf{y}$ and $\mathbf{X}$. Note that unlike GoSLIM, which can be employed at each receiver to estimate the channel in parallel, GoSLIM-V implicitly suggests that the measurements acquired at different receivers should be assembled in a central processor before performing channel estimation. Moreover, GoSLIM-V simultaneously estimates the CIRs among all of the MN transmitter and receiver pairs.

GoSLIM-V is developed based on the following hierarchical Bayesian model, similarly to (2–23) and (2–24):

$$\mathbf{y}|\mathbf{h}, \mathbf{\Lambda}, \eta \sim \mathcal{CN}(\mathbf{\Lambda}\mathbf{X}\mathbf{h}, \eta\mathbf{I}), \tag{2–34}$$

$$\mathbf{h}|\mathbf{p} \sim \mathcal{CN}(\mathbf{0}, \mathbf{P}), \tag{2–35}$$

where $\mathbf{p} = [\mathbf{p}_1^T, \mathbf{p}_2^T, \ldots, \mathbf{p}_M^T]^T$ and $\mathbf{P} = \mathrm{diag}(\mathbf{p})$. The five steps of GoSLIM-V at the t^{th} iteration are briefly listed below:

1. Given $\mathbf{h}^{(t-1)}$, the optimal $\mathbf{P}^{(t)}$ is given by:

$$p_{n,m,r}^{(t)} = \left| h_{n,m,r}^{(t-1)} \right|^2, \tag{2–36}$$

   for $n = 1, \ldots, N$, $m = 1, \ldots, M$, and $r = 1, \ldots, R$.

2. Once $\mathbf{P}^{(t)}$ is available, the CIR is updated as:

$$\mathbf{h}^{(t)} = \left[\mathbf{X}^H \mathbf{X} + \eta^{(t-1)} \left(\mathbf{P}^{(t)} \right)^{-1} \right]^{-1} \left(\mathbf{\Lambda}^{(t-1)} \mathbf{X} \right)^H \mathbf{y}. \tag{2–37}$$

3. The Doppler frequency $f^{(t)}$ is updated as:

$$f^{(t)} = \arg\max_f \mathrm{Re} \left[\sum_{i=1}^{d_y} \left(\sum_{m=1}^{M} z_m^{(t)}(i) \right) e^{-2j\pi f T_s (i-1)} \right]. \tag{2–38}$$

4. The noise power is estimated as:

$$\eta^{(t)} = \frac{1}{d_y M} \left\| \mathbf{y} - \mathbf{\Lambda}^{(t)} \mathbf{X} \mathbf{h}^{(t)} \right\|^2. \tag{2–39}$$

5. Set $t = t + 1$. Go back to Step 1 if t is less than a predefined iteration number, or terminate otherwise.

The initialization of GoSLIM-V is similar to that of GoSLIM. In our examples, $\mathbf{h}^{(0)}$ is initialized using the standard matched filter, $f^{(0)}$ is initialized as 0 and the noise power $\eta^{(0)}$ is initialized with a small positive number, for instance, 10^{-10}. Our empirical experience suggests that the GoSLIM-V algorithm does not provide significant performance improvements after no more than 15 iterations.

2.3.5 Complexity Analysis

Empirical experience indicates that the computational bottleneck of GoSLIM is in the update of the Doppler frequency; see (2–30). Previously in [21], at each GoSLIM iteration, we zero pad the sequence $\{z_m^{(t)}(i)\}_{i=1}^{d_y}$ to a length of 2^{20}, followed by the employment of fast Fourier transform (FFT) to obtain the frequency spectrum. Then, $f_m^{(t)}$ is obtained as the location of the dominant peak of the real part of the so-obtained spectrum. This procedure has approximately 2^{24} floating point operations

(flops). Alternatively, we can also establish a frequency grid of d_g grid points and calculate the DTFT of $\{z_m^{(t)}(i)\}_{i=1}^{d_y}$ evaluated at each frequency grid point using (2–30) directly. In this way, the complexity reduces to $\mathcal{O}(d_y d_g)$ per GoSLIM iteration. In our example, d_y is equal to 512 in the training-directed mode. The grid is from -5 Hz to 5 Hz with a step size of 0.001 Hz, and therefore, $d_g = 10001$. This setup corresponds to approximately 2^{22} flops, which is four times lower than that of using FFT. Therefore, the DTFT grid search is preferable over the FFT technique, and it is employed to analyze the in-water measurements. Although DTFT is more efficient than FFT, it still constitutes the computational bottleneck of the GoSLIM algorithm.

Since GoSLIM is employed at each receiver to conduct channel estimation in parallel, the overall complexity of the Doppler frequency update step is $\mathcal{O}(d_y d_g M)$ per GoSLIM iteration. In contrast, the complexity of the Doppler frequency update step in (2–38), by making use of DTFT, is $\mathcal{O}(d_y d_g)$ per GoSLIM-V iteration. The M times complexity reduction is mainly due to the fact that the frequency search is performed at each receiver for GoSLIM, but it is performed only once for GoSLIM-V. As a consequence, GoSLIM-V is computationally much more efficient than GoSLIM in a MIMO configuration, especially with a large number of receive elements. Due to the reduced number of unknowns, the GoSLIM-V data model is more parsimonious than that of GoSLIM, which could enhance the symbol detection performance if the model is reasonably accurate. We will show via MACE10 in-water experimentation results that GoSLIM-V slightly outperforms GoSLIM. Hence, GoSLIM-V is preferred and the subsequent symbol detection section is built upon employing GoSLIM-V in the channel estimation stage.

2.4 Symbol Detection

In this section, we proceed to study the detection of the payload symbols given the estimates of CIRs and Doppler frequency f obtained by GoSLIM-V. The detection task is achieved via two steps: phase compensation followed by Turbo equalization. As

shown in Figure 2-1B, Turbo equalization consists of an equalizer and a decoder, both configurated as soft-input soft-output. The decoder is conventionally implemented by the Max-Log-MAP algorithm [28], and our focus herein is on the soft-input soft-output equalizer. We first formulate the symbol detection problem and then describe the phase compensation procedure. After that, we elaborate the LMMSE based Turbo equalization design and discuss its low complexity approximation.

2.4.1 Problem formulation

Treating the transmitted symbols as the unknowns and the CIRs and Doppler frequency as known, the measurement vector in (2–14) can be expressed as [5, 35]:

$$\mathbf{y}_m(k) = \hat{\mathbf{\Lambda}}(k) \sum_{n=1}^{N} \hat{\mathbf{H}}_{n,m} \mathbf{x}_n(k) + \mathbf{e}_m, \quad m = 1, \dots, M, \tag{2–40}$$

where the estimated CIR matrix $\hat{\mathbf{H}}_{n,m} \in \mathbb{C}^{R \times (2R-1)}$ is given by

$$\hat{\mathbf{H}}_{n,m} = \begin{bmatrix} \hat{h}_{n,m,R} & \dots & \hat{h}_{n,m,1} & & \mathbf{0} \\ \vdots & \ddots & & \ddots & \vdots \\ \mathbf{0} & & \hat{h}_{n,m,R} & \dots & \hat{h}_{n,m,1} \end{bmatrix}, \tag{2–41}$$

for $n = 1, \dots, N$ and $m = 1, \dots, M$. The entry $\hat{h}_{n,m,r}$ here represents the estimate of $h_{n,m,r}$ in (2–17) given by GoSLIM-V at the conclusion of the iteration. Also,

$$\mathbf{x}_n(k) = [x_n(k-R+1), \dots, x_n(k), \dots, x_n(k+R-1)]^T, \quad n = 1, \dots, N, \tag{2–42}$$

and

$$\mathbf{y}_m(k) = [y_m(k), \dots, y_m(k+R-1)]^T, \qquad m = 1, \dots, M. \tag{2–43}$$

The variable k represents the time index corresponding to the payload symbols of current interest. Although $\mathbf{y}_m$ represents different portions of the received signal in (2–15), (2–20), and (2–43), its use should be clear from the context. Per the discussions following (2–18), once $\hat{f}$ is available, the estimated Doppler shift matrix $\hat{\mathbf{\Lambda}}(k)$ in (2–40)

can be constructed as:

$$\hat{\mathbf{\Lambda}}(k) = \text{diag}\left(\left[e^{-2j\pi\hat{f}\,T_s(k-1)},\ \ldots\ , e^{-2j\pi\hat{f}\,T_s(k+R-2)}\right]\right). \tag{2–44}$$

When detecting symbols, we use the estimates $\{\hat{\mathbf{h}}_{n,m}\}$ and $\hat{f}$ obtained from the previous channel update and we treat $\{\hat{\mathbf{H}}_{n,m}\}$ and $\hat{\mathbf{\Lambda}}(k)$ in (2–40) as known.

2.4.2 Phase Compensation

Stacking up all the measurements, (2–40) can be written as

$$\begin{bmatrix} \mathbf{y}_1(k) \\ \vdots \\ \mathbf{y}_M(k) \end{bmatrix} = \mathring{\mathbf{\Lambda}}(k) \sum_{n=1}^{N} \begin{bmatrix} \hat{\mathbf{H}}_{n,1} \\ \vdots \\ \hat{\mathbf{H}}_{n,M} \end{bmatrix} \mathbf{x}_n(k) + \begin{bmatrix} \mathbf{e}_1 \\ \vdots \\ \mathbf{e}_M \end{bmatrix}, \tag{2–45}$$

or, equivalently as,

$$\begin{aligned} \mathbf{y}(k) &= \mathring{\mathbf{\Lambda}}(k) \sum_{n=1}^{N} \hat{\mathbf{H}}_n \mathbf{x}_n(k) + \mathbf{e} \\ &= \mathring{\mathbf{\Lambda}}(k) \hat{\mathbf{H}} \mathbf{x}(k) + \mathbf{e}, \end{aligned} \tag{2–46}$$

where $\mathbf{y}(k)$ and $\mathbf{e} \in \mathbb{C}^{MR\times 1}$, $\mathring{\mathbf{\Lambda}}(k) = \mathbf{I}_{M\times M} \otimes \hat{\mathbf{\Lambda}}(k)$, $\{\hat{\mathbf{H}}_n\}_{n=1}^{N} \in \mathbb{C}^{MR\times(2R-1)}$, $\hat{\mathbf{H}} = [\hat{\mathbf{H}}_1, \ldots, \hat{\mathbf{H}}_N]$, and $\mathbf{x}(k) = [\mathbf{x}_1^T(k), \ldots, \mathbf{x}_N^T(k)]^T$. The phase compensation task is simply achieved by multiplying $[\mathring{\mathbf{\Lambda}}(k)]^H$ to both sides of (2–46), yielding

$$\mathring{\mathbf{y}}(k) = \hat{\mathbf{H}} \mathbf{x}(k) + \mathring{\mathbf{e}}, \tag{2–47}$$

where $\mathring{\mathbf{y}}(k) = [\mathring{\mathbf{\Lambda}}(k)]^H \mathbf{y}(k)$ and $\mathring{\mathbf{e}} = [\mathring{\mathbf{\Lambda}}(k)]^H \mathbf{e}$. Given $\mathbf{e} \sim \mathcal{CN}(\mathbf{0}, \eta\mathbf{I})$, $\mathring{\mathbf{e}}$ still has the distribution of $\mathcal{CN}(\mathbf{0}, \eta\mathbf{I})$ since $[\mathring{\mathbf{\Lambda}}(k)]^H$ is unitary.

Phase compensation, along with the aforementioned temporal resampling process, effectively converts the original double-selective channel to an ISI channel. Given the phase-compensated measurement vector $\mathring{\mathbf{y}}(k)$, the estimated CIR matrix $\hat{\mathbf{H}}$, and $\{L_d(c_n(k))\}_{n=1,k=1}^{N,2K}$, we consider using an LMMSE based soft-input soft-output equalizer to compute the *a posteriori extrinsic* information of the transmitted signal.

2.4.3 LMMSE Based Soft-Input Soft-Output Equalizer

As shown in Figure 2-2, an LMMSE based soft-input soft-output equalizer can be functionally divided into four modules. The *a priori* LLR pre-processor calculates the mean and the variance of each QPSK payload symbol $x_n(k)$, denoted as $\bar{x}_n(k)$ and $v_n(k)$, respectively, from the *a posteriori extrinsic* information $L_d(c_n(2k-1))$ and $L_d(c_n(2k))$ generated by the decoder for $n = 1, \ldots, N$ and $k = 1, \ldots, K$. Next, the transmitted symbol $x_n(k)$ is estimated via LMMSE filtering given $\mathring{\mathbf{y}}(k)$ and $\hat{\mathbf{H}}$ in (2–47), along with $\{\bar{x}_n(k)\}$ and $\{v_n(k)\}$. Specifically, as demonstrated in Figure 2-2, the LMMSE filter is applied to the residual signal generated by subtracting out the so-called soft interferences from the phase-compensated measurements. The soft interferences characterize the contributions of all the payload symbols except $x_n(k)$, the one of the current interest, in terms of soft information. Based on the symbol estimates $\hat{x}_n(k)$, the *a posteriori* LLR generator provides the *extrinsic* LLR outputs $L_e(c_n(2k-1))$ and $L_e(c_n(2k))$ ($n = 1, \ldots, N$, $k = 1, \ldots, K$), which will be fed into the soft-input soft-output decoder as *a priori* LLR, see Figure 2-1B. In the following, these modules will be elaborated further.

2.4.3.1 *A priori* LLR pre-processor

In this task, we calculate $\bar{x}_n(k)$ and $v_n(k)$ from $L_d(c_n(2k-1))$ and $L_d(c_n(2k))$. According to the definitions, the mean and variance of $x_n(k)$ are given by [22]:

$$\bar{x}_n(k) = \sum_{i=1}^{4} \alpha_i \cdot P(x_n(k) = \alpha_i), \tag{2–48}$$

$$v_n(k) = \sum_{i=1}^{4} |\alpha_i|^2 \cdot P(x_n(k) = \alpha_i) - |\bar{x}_n(k)|^2 = 1 - |\bar{x}_n(k)|^2, \tag{2–49}$$

where $\{\alpha_i\}_{i=1}^4$ denote the four QPSK constellation points of $\mathcal{S}$ and $|\alpha_i| = 1$ for $i = 1, \ldots, 4$; see the definition of $\mathcal{S}$ after (2–1). One can see from (2–49) that $v_n(k)$ depends on $\bar{x}_n(k)$, and the evaluation of $\bar{x}_n(k)$ in (2–48) requires $P(x_n(k) = \alpha_i)$ for $i = 1, \ldots, 4$. Since the interleaved bits $\{c(k)\}$ can be reasonably assumed to be independent of each other

due to the employment of the random interleaver (see Figure 2-1A), $P(x_n(k) = \alpha_i)$ is determined as the product of the probabilities of the two interleaved bits that map to α_i. For instance, $c_n(2k-1) = 0$ and $c_n(2k) = 1$ map to $x_n(k) = (-1+j)/\sqrt{2}$ according to (2–1), and therefore, $P(x_n(k) = (-1+j)/\sqrt{2}) = P(c_n(2k-1) = 0) \cdot P(c_n(2k) = 1)$, where for a generic interleaved bit $c_n(q)$ we have

$$\begin{aligned} P(c_n(q) = 0) &= \frac{e^{L_d(c_n(q))}}{1 + e^{L_d(c_n(q))}}, \\ P(c_n(q) = 1) &= \frac{1}{1 + e^{L_d(c_n(q))}}, \end{aligned} \tag{2–50}$$

for $n = 1, \ldots, N$ and $q = 1, \ldots, 2K$. Equation (2–50) follows from (2–2) and $P(c_n(q) = 0) + P(c_n(q) = 1) = 1$.

Plugging (2–50) into (2–48) gives:

$$\bar{x}_n(k) = \frac{1}{\sqrt{2}} \left\{ j \tanh\left[\frac{L_d(c_n(2k-1))}{2}\right] + \tanh\left[\frac{L_d(c_n(2k))}{2}\right] \right\}, \quad n = 1, \ldots, N, \quad k = 1, \ldots, K, \tag{2–51}$$

which, combined with (2–49), yields $v_n(k)$.

2.4.3.2 LMMSE filtering

Depending on whether the *a priori* LLR information is incorporated or not, two types of LMMSE filters are studied in the following.

In the absence of *a priori* knowledge. The equalizer is performed in the absence of *a priori* knowledge at the very first iteration before using the decoder. This scenario amounts to setting $L_d(c_n(k)) = 0$ for $n = 1, \ldots, N$ and $k = 1, \ldots, 2K$, which implies that $\bar{x}_n(k) = 0$ and $v_n(k) = 1$ according to (2–51) and (2–49) for $n = 1, \ldots, N$ and $k = 1, \ldots, K$. In this case, the LMMSE filter coefficient vector, denoted as $\mathbf{f}_n$, is given by [12, 39]:

$$\mathbf{f}_n = \left(\hat{\mathbf{H}}\hat{\mathbf{H}}^H + \hat{\eta}\mathbf{I}\right)^{-1} \mathbf{s}_n. \tag{2–52}$$

Here, $\hat{\eta}$ represents the noise power estimate given by GoSLIM-V at the conclusion of the iteration, $\mathbf{s}_n = [\hat{\mathbf{h}}_{n,1}^T, \ldots, \hat{\mathbf{h}}_{n,M}^T]^T$ denotes the steering vector corresponding to $x_n(k)$ in

(2–46) for $n = 1, \ldots, N$, and $\hat{\mathbf{h}}_{n,m}$ is the estimate of $\mathbf{h}_{n,m}$ defined in (2–17). An estimate of $x_n(k)$ is obtained by applying $\mathbf{f}_n$ to the phase-compensated measurement vector obtained in (2–47):

$$\hat{x}_n(k) = \mathbf{f}_n^H \mathring{\mathbf{y}}(k), \quad n = 1, \ldots, N. \tag{2–53}$$

In the presence of *a priori* knowledge. In this case, the LMMSE estimate of $x_n(k)$ is given by [22]:

$$\hat{x}_n(k) = \bar{x}_n(k) + v_n(k)\mathbf{f}_n'(k)^H \left[\mathring{\mathbf{y}}(k) - \hat{\mathbf{H}}\mathrm{E}(\mathbf{x}(k))\right], \tag{2–54}$$

where

$$\mathbf{f}_n'(k) = \left[\hat{\mathbf{H}}\mathbf{V}(k)\hat{\mathbf{H}}^H + \hat{\eta}\mathbf{I}\right]^{-1}\mathbf{s}_n \tag{2–55}$$

represents the LMMSE filter coefficient vector. In (2–54), each component of $\mathrm{E}(\mathbf{x}(k))$ is the expected value of the corresponding component of $\mathbf{x}(k)$ calculated in (2–48). In (2–55), the covariance matrix $\mathbf{V}(k) = \mathrm{diag}\left(\left[\mathbf{v}_1(k)^T, \ldots, \mathbf{v}_N(k)^T\right]\right)$, and

$$\mathbf{v}_n(k) = [v_n(k-R+1), \ldots, v_n(k), \ldots, v_n(k+R-1)]^T, \quad n = 1, \ldots, N. \tag{2–56}$$

Each component of $\mathbf{v}_n(k)$ is obtained according to (2–49).

Equation (2–54) suggests that the estimation of $x_n(k)$ depends on its own *extrinsic* LLR information $L_d(c_n(2k-1))$ and $L_d(c_n(2k))$, whose impact on $\hat{x}_n(k)$ comes through $\bar{x}_n(k)$ and $v_n(k)$. From the belief propagation theory point of view, the generation of *extrinsic* information of a payload symbol needs to avoid such dependency [40]. To achieve this goal, we modify (2–54) as:

$$\hat{x}_n(k) = \mathbf{s}_n^H \left[\hat{\mathbf{H}}\mathbf{V}(k)\hat{\mathbf{H}}^H + \hat{\eta}\mathbf{I} + (1 - v_n(k))\mathbf{s}_n\mathbf{s}_n^H\right]^{-1} \left[\mathring{\mathbf{y}}(k) - \hat{\mathbf{H}}\mathrm{E}(\mathbf{x}(k)) + \bar{x}_n(k)\mathbf{s}_n\right]. \tag{2–57}$$

Compared to (2–54), the presence of the two additional terms in (2–57), namely $(1 - v_n(k))\mathbf{s}_n\mathbf{s}_n^H$ and $\bar{x}_n(k)\mathbf{s}_n$, resembles a scenario of $\bar{x}_n(k) = 0$ and $v_n(k) = 1$ (or equivalently, $L_d(c_n(2k-1)) = L_d(c_n(2k)) = 0$) in (2–54), as if $x_n(k)$ is estimated without incorporating its own LLR information.

Define

$$\mathbf{f}_n''(k) = \left[\hat{\mathbf{H}}\mathbf{V}(k)\hat{\mathbf{H}}^H + \hat{\eta}\mathbf{I} + (1 - v_n(k))\mathbf{s}_n\mathbf{s}_n^H\right]^{-1}\mathbf{s}_n, \tag{2–58}$$

and

$$\dot{\mathbf{y}}_n(k) = \mathring{\mathbf{y}}(k) - \left[\hat{\mathbf{H}}\mathrm{E}(\mathbf{x}(k)) - \bar{x}_n(k)\mathbf{s}_n\right]. \tag{2–59}$$

Then, (2–57) can be rewritten as:

$$\hat{x}_n(k) = \mathbf{f}_n''(k)^H\dot{\mathbf{y}}_n(k). \tag{2–60}$$

In (2–59), the terms within the square brackets correspond to the output of the soft interference generator in Figure 2-2. To get $\hat{x}_n(k)$, the LMMSE filter coefficient vector in (2–58) is applied to the residual measurement vector $\dot{\mathbf{y}}_n(k)$. Note that (2–60) includes (2–53) as a special case when no *a priori* knowledge is available, i.e., $L_d(c_n(k)) = 0$ for $n = 1, \ldots, N$ and $k = 1, \ldots, 2K$.

2.4.3.3 *A posteriori* LLR generator

This task calculates the *extrinsic* LLR $L_e(c_n(2k-1))$ and $L_e(c_n(2k))$ from the symbol estimates $\hat{x}_n(k)$ obtained in (2–53) or (2–60) for $n = 1, \ldots, N$ and $k = 1, \ldots, K$.

We assume that given $x_n(k) = \alpha_i$, $\hat{x}_n(k)$ is a circularly symmetric i.i.d. complex-valued Gaussian random process, i.e., $P(\hat{x}_n(k)|x_n(k) = \alpha_i) \sim \mathcal{CN}(\mu_i, \sigma^2)$, where the mean μ_i and variance σ^2 are calculated, respectively, as $\mu_i = \alpha_i\mathbf{f}_n''(k)^H\mathbf{s}_n$ and $\sigma^2 = \mathbf{f}_n''(k)^H\mathbf{s}_n - \mathbf{f}_n''(k)^H\mathbf{s}_n\mathbf{s}_n\mathbf{f}_n''(k)$ [22]. Under this assumption, the output LLR of the two consecutive bits mapping to $x_n(k)$ is calculated as [22]:

$$\begin{aligned} L_e(c_n(2k-1)) &= \frac{\sqrt{8}\mathrm{Im}(\mathbf{f}_n''(k)^H\dot{\mathbf{y}}_n(k))}{1 - \mathbf{s}_n^H\mathbf{f}_n''(k)}, \\ L_e(c_n(2k)) &= \frac{\sqrt{8}\mathrm{Re}(\mathbf{f}_n''(k)^H\dot{\mathbf{y}}_n(k))}{1 - \mathbf{s}_n^H\mathbf{f}_n''(k)}, \end{aligned} \tag{2–61}$$

for $n = 1, \ldots, N$ and $k = 1, \ldots, K$.

Let $\mathbf{R}'(k) = \hat{\mathbf{H}}\mathbf{V}(k)\hat{\mathbf{H}}^H + \hat{\eta}\mathbf{I}$ and $\mathbf{R}_n''(k) = \hat{\mathbf{H}}\mathbf{V}(k)\hat{\mathbf{H}}^H + \hat{\eta}\mathbf{I} + (1 - v_n(k))\mathbf{s}_n\mathbf{s}_n^H$. Then $\mathbf{f}_n'(k)$ in (2–55) and $\mathbf{f}_n''(k)$ in (2–58) can be rewritten as $\mathbf{f}_n'(k) = \mathbf{R}'(k)^{-1}\mathbf{s}_n$ and $\mathbf{f}_n''(k) = \mathbf{R}_n''(k)^{-1}\mathbf{s}_n$,

respectively. One observes that the derivation of $\{\mathbf{f}_n''(k)\}$ requires the inversion of $\mathbf{R}_n''(k)$ for each transmitter at each time index, whereas the computation of $\{\mathbf{f}_n'(k)\}$ needs to invert $\mathbf{R}'(k)$ at each time index. Consequently, by following (2–55) and (2–58) directly, the computational complexity of calculating $\{\mathbf{f}_n''(k)\}$ is approximately N times more expensive than obtaining $\{\mathbf{f}_n'(k)\}$.

Since $\mathbf{R}_n''(k) = \mathbf{R}'(k) + (1 - v_n(k))\mathbf{s}_n\mathbf{s}_n^H$, the use of the matrix inversion lemma gives:

$$\mathbf{R}_n''(k)^{-1} = \mathbf{R}'(k)^{-1} - \frac{(1 - v_n(k))\mathbf{R}'(k)^{-1}\mathbf{s}_n\mathbf{s}_n^H\mathbf{R}'(k)^{-1}}{1 + (1 - v_n(k))\mathbf{s}_n^H\mathbf{R}'(k)^{-1}\mathbf{s}_n}. \tag{2–62}$$

Right multiplying $\mathbf{s}_n$ on both sides of (2–62) yields:

$$\mathbf{f}_n''(k) = \frac{\mathbf{f}_n'(k)}{1 + (1 - v_n(k))\mathbf{s}_n^H\mathbf{f}_n'(k)}, \tag{2–63}$$

which, combined with (2–61), follows

$$\begin{aligned} L_e(c_n(2k-1)) &= \frac{\sqrt{8}\mathrm{Im}(\mathbf{f}_n'(k)\dot{\mathbf{y}}_n(k))}{1 - v_n(k)\mathbf{s}_n^H\mathbf{f}_n'(k)}, \\ L_e(c_n(2k)) &= \frac{\sqrt{8}\mathrm{Re}(\mathbf{f}_n'(k)\dot{\mathbf{y}}_n(k))}{1 - v_n(k)\mathbf{s}_n^H\mathbf{f}_n'(k)}. \end{aligned} \tag{2–64}$$

Complexity-wise, the LLR calculation formula in (2–64) is preferable over (2–61) since as we just remarked, it is more efficient to calculate $\{\mathbf{f}_n'(k)\}$ than $\{\mathbf{f}_n''(k)\}$. Due to this reason, LLR is calculated according to (2–64) in our numerical and experimental examples provided later on.

2.4.4 Low-Complexity Approximate LMMSE Filtering

Although the calculation of *a posteriori* LLR according to (2–64) is more efficient than (2–61), it still constitutes the major computational bottleneck in Turbo equalization mainly because $\{\mathbf{f}_n'(k)\}$ needs to be calculated at each time index. To further reduce the computational complexity, we consider a low-complexity approximate LMMSE filter whose coefficient vector is given by:

$$\mathbf{f}_n' = \left(\hat{\mathbf{H}}\bar{\mathbf{V}}\hat{\mathbf{H}}^H + \hat{\eta}\mathbf{I}\right)^{-1}\mathbf{s}_n, \tag{2–65}$$

where $\bar{\mathbf{V}} = \frac{1}{K}\sum_{k=1}^{K}\mathbf{V}(k)$. Since $\{\mathbf{f}'_n\}$ is constant for each transmitter over one payload block (hence the time index k is dropped in (2–65)), the overall complexity of calculating $\{\mathbf{f}'_n\}$ is approximately K times faster than deriving $\{\mathbf{f}'_n(k)\}$ according to (2–55). Substituting $\mathbf{f}'_n(k)$ in (2–64) with $\mathbf{f}'_n$ yields:

$$\begin{aligned} L_e(c_n(2k-1)) &= \frac{\sqrt{8}\mathrm{Im}(\mathbf{f}'^{H}_n \dot{\mathbf{y}}_n(k))}{1 - v_n(k)\mathbf{s}_n^H \mathbf{f}'_n}, \\ L_e(c_n(2k)) &= \frac{\sqrt{8}\mathrm{Re}(\mathbf{f}'^{H}_n \dot{\mathbf{y}}_n(k))}{1 - v_n(k)\mathbf{s}_n^H \mathbf{f}'_n}. \end{aligned} \tag{2–66}$$

We hereafter refer to the Turbo equalization scheme that calculates the *a posteriori extrinsic* information according to (2–64) and (2–66) as Exact-LMMSE-Turbo and Approximate-LMMSE-Turbo, respectively.

Note that matrix inversion is an indispensable stage in calculating the LMMSE filter coefficients in (2–52), (2–55), and (2–65). To expedite the calculation, we can make use of the conjugate gradient (CG) method and fast Fourier transform (FFT) operations, as elaborated in [41]. Although [41] focuses on the efficient calculation of the LMMSE filter coefficients in the form of (2–52), the extension to a more general scenario in (2–55) or (2–65) is straightforward. In the work, both Exact-LMMSE-Turbo and Approximate-LMMSE-Turbo are implemented using the FFT-based CG method.

2.5 Numerical and Experimental Results

2.5.1 Numerical Results

Consider transmitting four payload blocks simultaneously over time-invariant ISI channels using a MIMO UAC system equipped with $N = 4$ transmitters and $M = 12$ receivers. Block length is fixed at $K = 250$. The four payload blocks across the $N = 4$ transmitters are constructed from a randomly generated binary source sequence of length $NK = 1000$ according to the procedure detailed in Section 2.1. We simulate $N \times M = 48$ frequency-selective channels involved in the MIMO UAC system. To resemble practical UAC scenarios, these simulated CIRs are estimated from MACE10 in-water experimental data and each CIR has $R = 50$ taps. CIRs have been normalized

to 1, i.e., $\|\mathbf{h}_{n,m}\|^2 = 1$ for $n = 1, \ldots, N$ and $m = 1, \ldots, M$. The received data samples are then constructed according to (2–14). Since Doppler effects are not considered in this example, $\bar{\mathbf{\Lambda}} = \mathbf{I}$. The noise vector $\{\mathbf{e}_m\}$ is assumed to contain circularly symmetric i.i.d. complex-valued Gaussian random variables with zero-mean and variance σ^2. The simulation of ISI channels, combined with the assumption that each receiver has perfect knowledge on the channel characteristics $\{\mathbf{h}_{n,m}\}$, suggests that we can bypass the temporal resampling, channel estimation, and phase compensation modules in Figure 2-1B and apply Exact-LMMSE-Turbo, Approximate-LMMSE-Turbo, and RELAX-BLAST directly to the received measurements. Figures 2-3A and 2-3B show the average coded bit error rate (BER) given by Exact-LMMSE-Turbo and Approximate-LMMSE-Turbo, respectively, along with the RELAX-BLAST performance at different SNRs, where SNR is defined as $1/\sigma^2$. Each point is averaged over 500 Monte-Carlo trials. The binary source sequence and the noise pattern vary from one trial to another. The curve labeled as "No Iteration" is obtained by employing the equalizer and the decoder only once, i.e., the feedback loop is yet to be formed. In addition, the average coded BER given by RELAX-BLAST is obtained after three iterations. We can see from Figure 2-3 that both types of Turbo equalization schemes effectively reduce the coded BER as the iteration proceeds and significantly outperform RELAX-BLAST, and Exact-LMMSE-Turbo provides only slightly better detection performance than Approximate-LMMSE-Turbo. Complexity-wise, the average time required to finish one trial is 18.64 s, 0.49 s, and 0.19 s on an ordinary workstation (Intel Xeon E5506 processor 2.13G Hz, 12GB RAM, Windows 7 64-bit, and MATLAB R2010b) for Exact-LMMSE-Turbo, Approximate-LMMSE-Turbo, and RELAX-BLAST, respectively. Consequently, Approximate-LMMSE-Turbo is preferred over its Exact-LMMSE-Turbo counterpart since the former provides almost the same detection performance as the latter but with a computational complexity on the same order as RELAX-BLAST.

2.5.2 MACE10 In-Water Experimentation Results

2.5.2.1 Experiment specifics

The MACE10 in-water experiment was conducted by the Woods Hole Oceanographic Institution (WHOI) off the coast of Martha's Vineyard, MA in June 2010. A source array consisting of 4 transducers was vertically deployed at a depth of 80 m and towed by a vessel. At the receiver side, a 12-element hydrophone array was mounted on a buoy. The vessel moved from the minimum range of 500 m away from the receiving array outbound to the maximum range of 4000 m and then inbound back to the minimum range. The carrier frequency, sampling frequency, and symbol rate employed in the MACE10 experiment were 13 kHz, 39.0625 kHz, and 3.90625 kHz, respectively. By transmitting $N = 4$ sequences simultaneously and incorporating the measurements acquired from all of the $M = 12$ receiver elements for analysis, we established a 4×12 MIMO UAC system.

The structure of a transmitted data package is shown in Figure 2-4. Each package consists of 4 packets. The 1^{st} packet conveys a grayscale Gator mascot and the subsequent 3 packets combined form a colored mascot. The RGB components of the colored image were transmitted in the 2^{nd}, 3^{rd}, and 4^{th} packets, respectively. Each pixel of the Gator grayscale image is represented by 5 bits, corresponding to 32 different intensities (e.g., pure white and pure dark pixels are represented by 11111 and 00000, respectively). The 64-pixel by 100-pixel grayscale mascot image, as a consequence, is represented by a total of 32 k source bits. Accordingly, a colored mascot image is represented by 96 k bits. The contrast of the grayscale image, as well as the hue of the colored image, has been carefully adjusted so that the image carries approximately equal numbers of 1's and 0's.

As shown in Figure 2-4, each packet is constructed as follows: time-marking sequences are placed at the beginning of each packet to facilitate the temporal resampling procedure; two guard intervals, each containing 500 silent symbols, are

placed, respectively, before and after the segments containing the payload symbols and training sequences. The payload symbols contain the information of the Gator mascot image. We herein elaborate how to generate the 1^{st} packet from the grayscale Gator mascot image (the packet generation for each of the RGB components of the colored image follows the same procedure). Specifically, the 32 k source bits are first interleaved so that the bits feeding into the convolutional encoder module have an equal chance of being 0 or 1; see Figure 2-5. The so-obtained 32 k interleaved source bits are then divided into 32 groups, each containing 1 k bits. The bits in the i^{th} group ($i = 1, \ldots, 32$) will be used to construct the i^{th} payload symbol block across the 4 transmitted sequences, and the construction procedure follows Figure 2-1A. Note that in Figure 2-5, the depth of the interleavers Π' and Π is 32 k and 2 k, respectively. Figure 2-5 illustrates a scenario with $i = 1$. The shifted PeCAN training sequences with length $P = 512$, in conjunction with $L_{\mathrm{CP}} = 99$ cyclic prefix symbols, form the training section, which is located between the 16^{th} and 17^{th} payload blocks. This MIMO UAC design leads to a net coded data rate of 11.7 kbps. The data package was transmitted periodically and recorded by the receiver array. A total of 120 epochs were available and they are referred to as "E001"$-$"E120", respectively.

To estimate the Doppler scaling factor, we treat the time-marking sequences at the beginning of a packet as its preamble and those at the beginning of the subsequent packet as the postamble. Take the 2^{nd} packet of epoch "E002" for example. For the channel between the 1^{st} transmitter and the 1^{st} receiver, the superimposed modulus of the CIRs obtained by GoSLIM-V from the preamble and postamble is shown in Figure 2-6. The indexes of the principal arrivals for the preamble and postamble are 12 and 21, respectively. Hence, the time duration change imposed on the packet is $\hat{T}_d = (21 - 12)\, T_s$, where T_s is the symbol period defined after (2–18). Then the Doppler scaling factor $\hat{\beta}$ can be estimated according to (2–12).

To assess the performance of the resampling process, the CIR and Doppler frequency evolutions obtained by GoSLIM-V before we resample the 2^{nd} packet of epoch "E002" are shown in Figures 2-7A and 2-7C, respectively. In comparison, Figures 2-7B and 2-7D demonstrate the corresponding CIR and Doppler frequency evolutions obtained after resampling the packet, respectively. We can see from Figure 2-7 that the temporal resampling procedure successfully reduces the Doppler scaling effects to Doppler frequency shifts. The relative speed between the transmitter and the receiver arrays can be estimated as $\hat{v} = \left(\hat{\beta} - 1\right) \cdot c$, using a common underwater sound speed of $c = 1500$ m/s. It is interesting to look at Figure 2-8 where the vessel speed estimated during the resampling stage is plotted on top of the GPS reference information provided by WHOI (the GPS device was equipped on the moving vessel). The good agreement between these two curves verifies the effectiveness of the resampling procedure we employ. The analysis presented hereafter is based on the resampled measurements.

2.5.2.2 Performance evaluation

We choose the 1^{st} packet of epoch "E018" to verify the channel model behind GoSLIM-V (other epochs give similar observations). The evolution of the Doppler frequencies produced by GoSLIM for all the 12 receive hydrophones are plotted superimposed in Figure 2-9 along with the evolution of the Doppler frequency obtained by GoSLIM-V. One observes that the curves show good agreement with each other, which verifies the validity of the key assumption that different receivers experience the same Doppler frequency. Moreover, the CIR evolution between the 1^{st} transmitter and the 1^{st} (2^{nd}) receiver obtained by GoSLIM is shown in Figure 2-10A (Figure 2-10B), and the CIR evolution between the 1^{st} transmitter and the 1^{st} (2^{nd}) receiver obtained by GoSLIM-V is shown in Figure 2-10C (Figure 2-10D). By comparing Figure 2-10A (Figure 2-10B) with Figure 2-10C (Figure 2-10D), we observe no visible difference between the CIR estimates obtained by the two algorithms.

Next, we proceed to assess the impact of the channel estimation algorithm on the resulting detection performance. The tracking length is fixed at $L_{\mathrm{TR}} = 450$ for all of the 120 epochs. The channel tracking starts with training-directed channel estimation using GoSLIM or GoSLIM-V. Then we perform phase compensation separately at each receiving hydrophone as done in (2–47) before proceeding to employ RELAX-BLAST to detect the first 250 payload symbols contained in the 17^{th} payload block for each transmitted sequence; see Figure 2-5. Next, the channels are updated in the decision-directed mode using 450 symbols (containing the previously detected payload symbols, as well as a portion of the training sequence as well). With the updated CIRs and Doppler frequency (frequencies), after phase compensation, the subsequent 250 payload symbols contained in the 18^{th} block are detected using RELAX-BLAST. This process continues until all of the 16 payload blocks to the right-hand side of the training sequences are detected. This same tracking scheme can be applied in a reverse manner to the detection of the 16 payload blocks ahead of the training sequences.

There is a total of 480 packets available and we deem a packet to be successfully detected if its coded BER is less than 0.1. When GoSLIM is employed as the channel estimation algorithm, we have succeeded in tracking the entire 32 payload blocks for 391 packets. A coded BER of 1.7×10^{-2} is achieved after averaging over the 391 successful packets. In comparison, when GoSLIM-V is used, 396 packets are successfully retrieved with an average coded BER of 1.6×10^{-2}. When GoSLIM is employed, Figures 2-11A, 2-11B, and 2-11C show the recovered grayscale mascots for “E013”, “E016”, and “E018”, respectively. The corresponding coded BERs and the computational time consumed at the channel estimation stage on an ordinary workstation (two Intel Xeon E5506 processors 2.13G Hz, 12GB RAM, Windows 7 64-bit, and MATLAB R2010b) are listed in the first row of Tables 2-1 and 2-2, respectively. In comparison, when GoSLIM-V is employed, the recovered grayscale mascots are shown in Figures 2-11D, 2-11E, and

2-11F, with the corresponding BERs and computational complexities listed in the second row of Tables 2-1 and 2-2, respectively. One observes from Table 2-1 that GoSLIM-V yields slightly better BER results than its GoSLIM counterpart. Moreover, Table 2-2 demonstrates that GoSLIM-V is about 4 times faster than GoSLIM. (Note that, by taking into account the complexity of all the steps other than the Doppler frequency update, the computational saving provided by GoSLIM-V against GoSLIM is thus less than 12 times.)

We then proceed to access the performance of the various symbol detection schemes with applying GoSLIM-V in the channel estimation stage. After analyzing the 480 packets available, Table 2-3 summarizes the successfully detected packet percentage, the zero BER packet percentage, the coded BER averaged over the successful packets, and the time ratio of the time consumed to process a packet on the workstation specified in Section 2.5.1 to $T_{tx} = 2.741s$ (T_{tx} is defined in (2–12)) obtained using Exact-LMMSE-Turbo, Approximate-LMMSE-Turbo, and the RELAX-BLAST scheme, respectively. The results are obtained by applying 3 iterations for all of the three types of detection schemes considered. One observes from Table 2-3 that 1) BER-wise, both Exact-LMMSE-Turbo and Approximate-LMMSE-Turbo outperform RELAX-BLAST significantly, 2) compared to Exact-LMMSE-Turbo, Approximate-LMMSE-Turbo greatly reduces the computational time at the cost of slight BER performance degradation, and 3) compared to RELAX-BLAST, Approximate-LMMSE-Turbo improves the BER performance by two orders of magnitude without significantly increasing the computational complexities. These observations are in line with those made from the numerical examples in Section 2.5.1. Moreover, we analyze epoch “E054” that leads to perfect recovery of both the grayscale and colored mascots (see Figures 2-12B and 2-12D) using either Exact-LMMSE-Turbo or Approximate-LMMSE-Turbo. In comparison, the grayscale and colored mascots recovered from epoch “E054” using RELAX-BLAST are shown in Figures 2-12A and 2-12C, respectively, with the corresponding coded

BERs being 1.8×10^{-1} and 1.5×10^{-1}. We note that the Turbo equalization schemes are highly effective.

To further illustrate the detection performance of Turbo equalization, Table 2-4 shows the coded BER averaged over all of the 480 packets at different iteration numbers obtained by Exact-LMMSE-Turbo and Approximate-LMMSE-Turbo. We can see from Table 2-4 that the coded BER improves with iteration. Empirical experience indicates that the detection performance for both types of Turbo equalization converges after three iterations. Next, we choose one payload block and denote $\{L_d(a(k))\}_{k=1}^{1000}$ as the LLR soft information of the corresponding 1 k source bits $\{a(k)\}_{k=1}^{1000}$ generated by the Max-Log-MAP decoder. Figures 2-13A-2-13D and 2-13E-2-13H show $\{L_d(a(k))\}_{k=1}^{1000}$ obtained by Exact-LMMSE-Turbo and Approximate-LMMSE-Turbo, respectively, at different iteration numbers. $\{\tilde{a}(k)\}$ in Figure 2-1B are the hard decisions determined from $\{L_d(a(k))\}$. Specifically, if $L_d(a(k)) > 0$ then $\tilde{a}(k) = 0$, otherwise $\tilde{a}(k) = 1$ (see (2–2)). In Figure 2-13, the circles indicate bit errors. We can see from Figure 2-13 that the LLR of source bits are moving away from zero as the iteration proceeds (the first iteration has the most significant impact), which suggests that with the help of cycling soft information, the decoder is more and more confident about the corresponding source bits being 0 or 1.

Table 2-1. Coded BER results obtained by GoSLIM and GoSLIM-V, respectively.

	E013	E016	E018
GoSLIM	3.6×10^{-2}	3.6×10^{-3}	1.6×10^{-4}
GoSLIM-V	2.3×10^{-2}	3.1×10^{-3}	9.4×10^{-5}

Table 2-2. Complexity comparison (in s) between GoSLIM and GoSLIM-V.

	E013	E016	E018
GoSLIM (15 iterations)	122.8	121.1	123.0
GoSLIM-V (15 iterations)	32.1	31.8	32.3

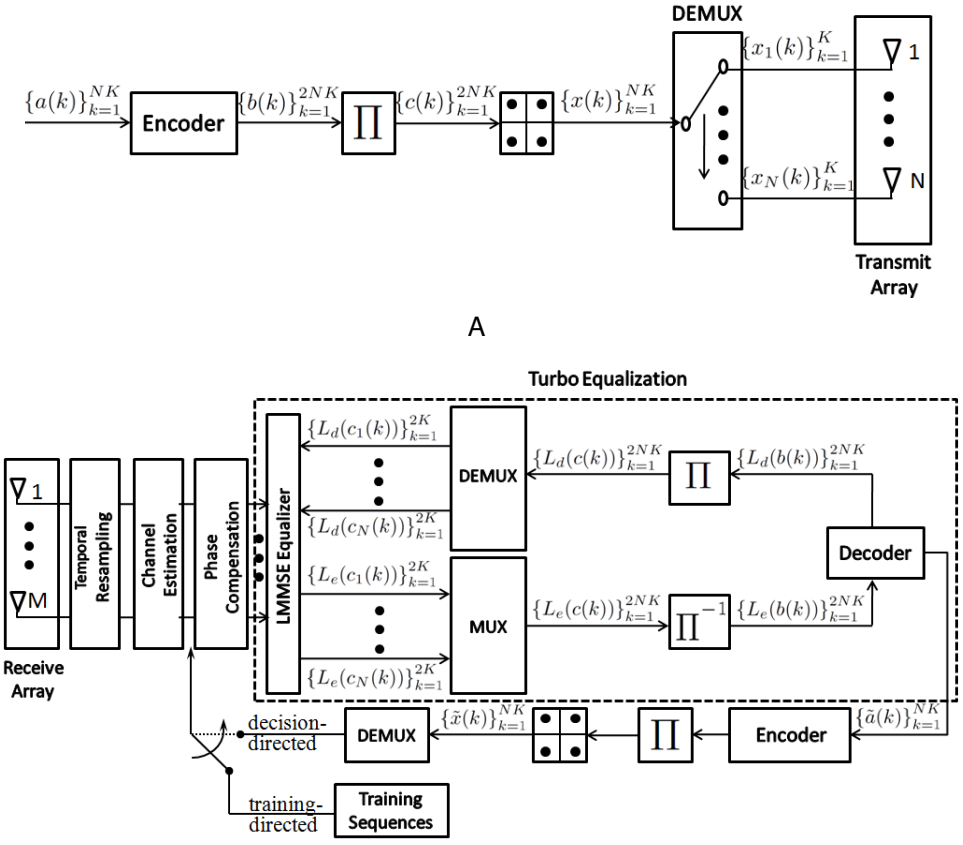

Figure 2-1. An $N \times M$ MIMO UAC system. A) Transmitter structure. B) Receiver structure by employing Turbo equalization.

Table 2-3. A summary of the performance of the three detection schemes (3 iterations applied).

	successful packet percentage (%)	zero BER packet percentage (%)	average coded BER	time ratio
Exact-LMMSE-Turbo	100	76.7	9.2×10^{-5}	488.1
Approximate-LMMSE-Turbo	100	74.4	2.1×10^{-4}	17.2
RELAX-BLAST	82.5	4.8	1.6×10^{-2}	16.9

Table 2-4. The average coded BER obtained by Exact LMMSE Turbo and Approximate LMMSE Turbo, respectively.

	No iteration	1 iteration	2 iterations	3 iterations
Exact-LMMSE-Turbo	2.7×10^{-1}	8.1×10^{-4}	1.3×10^{-4}	9.2×10^{-5}
Approximate-LMMSE-Turbo	2.7×10^{-1}	2.2×10^{-3}	3.2×10^{-4}	2.1×10^{-4}

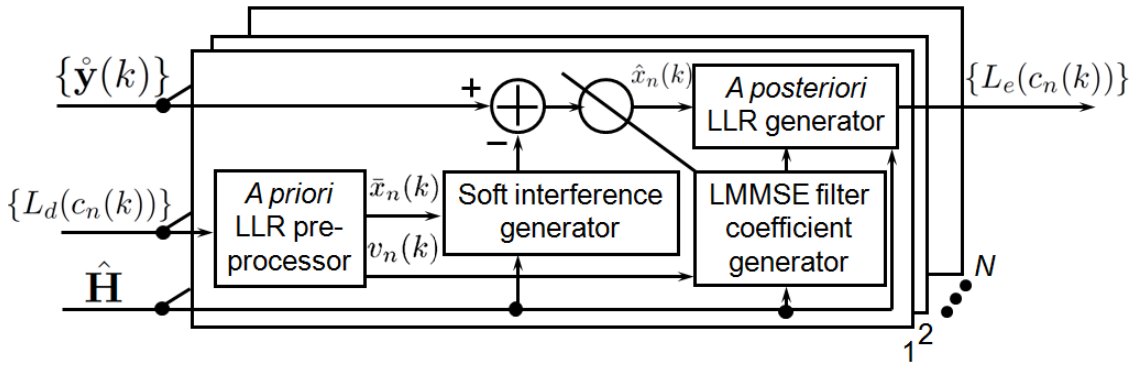

Figure 2-2. The structure of the LMMSE based soft-input soft-output equalizer.

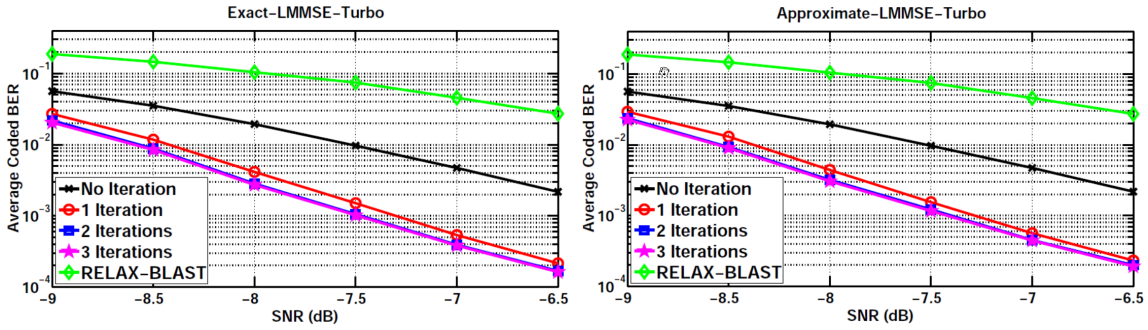

Figure 2-3. A) Coded BER performance by using Exact-LMMSE-Turbo along with RELAX-BLAST performance. B) Coded BER performance by using Approximate-LMMSE-Turbo along with RELAX-BLAST performance. Each point is averaged over 500 Monte-Carlo trials. In this simulation, $N = 4$, $M = 12$, $R = 50$ and $K = 250$.

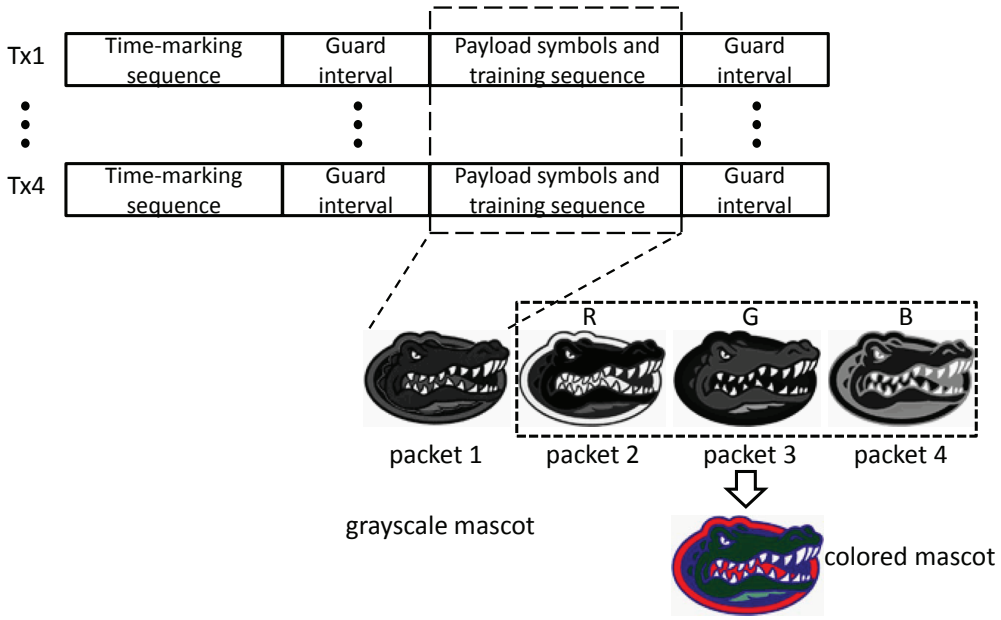

Figure 2-4. The structure of the package used in the MACE10 experiment.

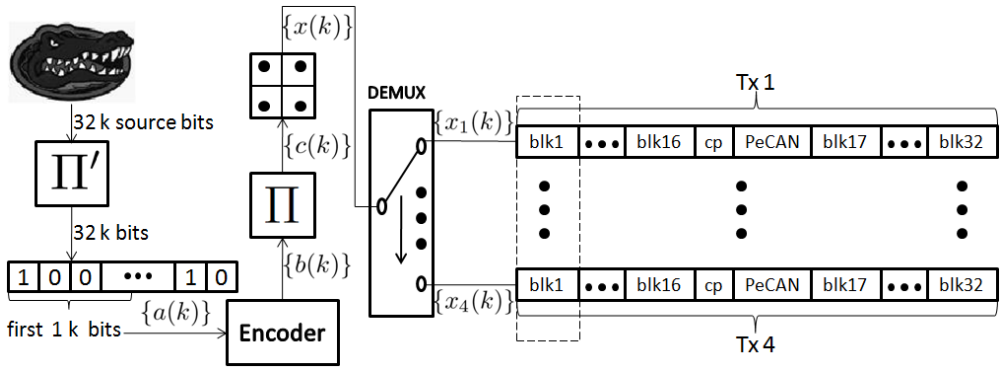

Figure 2-5. The structure of the transmitted symbols for the 4×12 MIMO BLAST scheme used in MACE10.

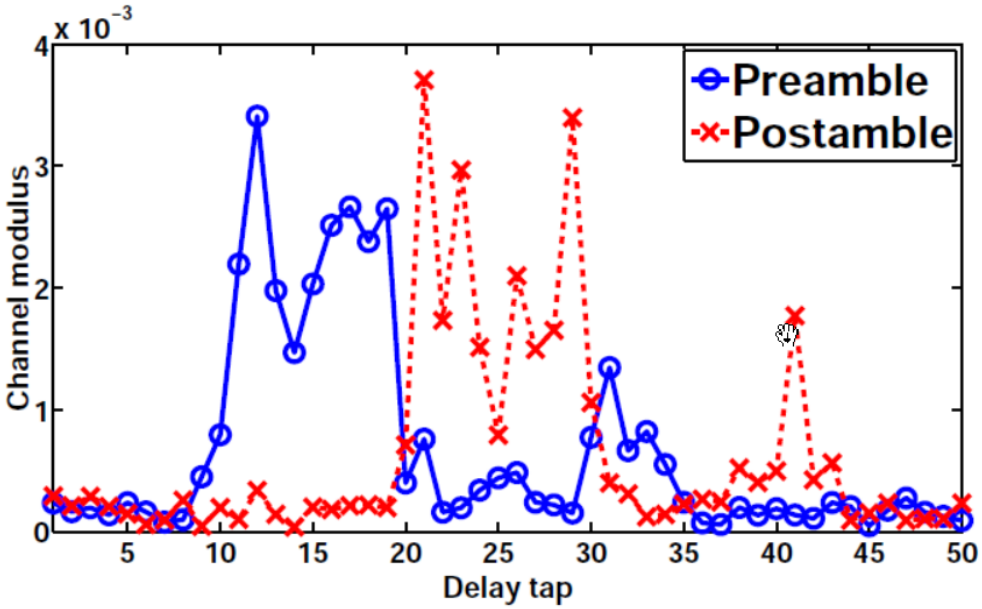

Figure 2-6. The superimposed modulus of the CIRs obtained from the preamble and postamble, respectively.

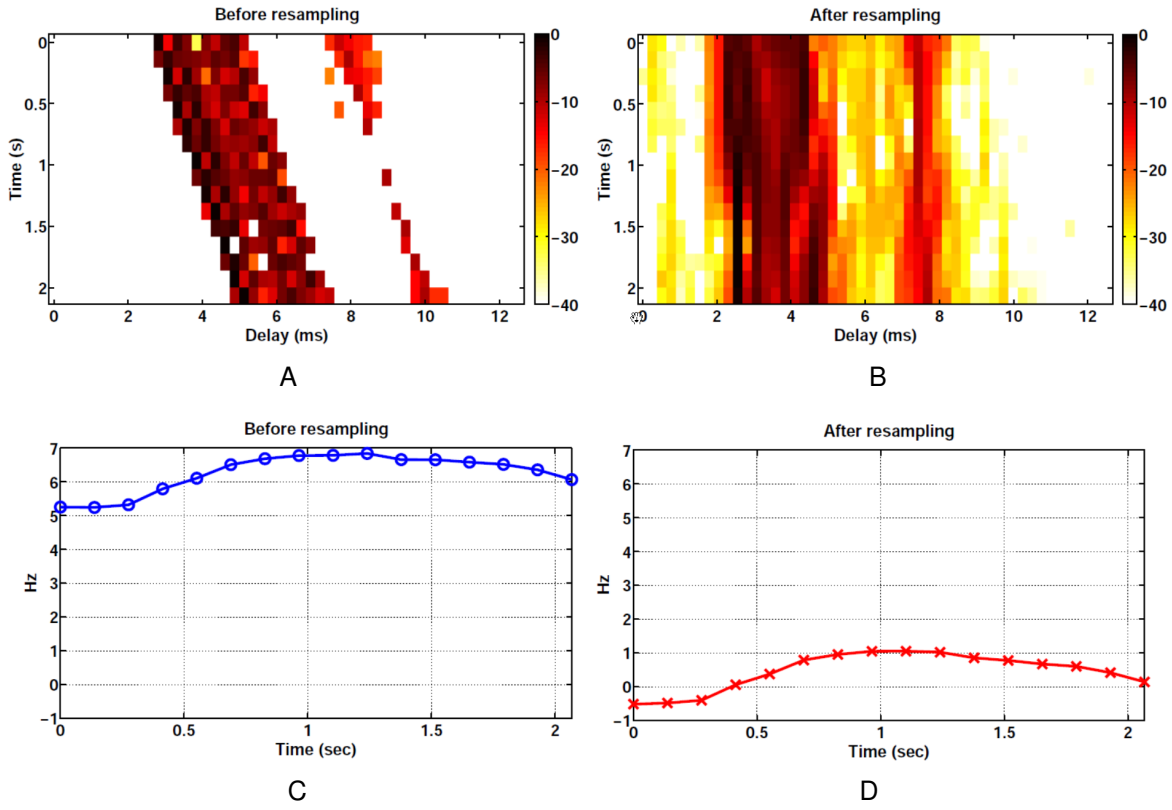

Figure 2-7. A) CIR evolution of Epoch “E002” before resampling. B) CIR evolution of Epoch “E002” after resampling. C) Doppler frequency evolution of Epoch “E002” before resampling. D) Doppler frequency evolution of Epoch “E002” after resampling.

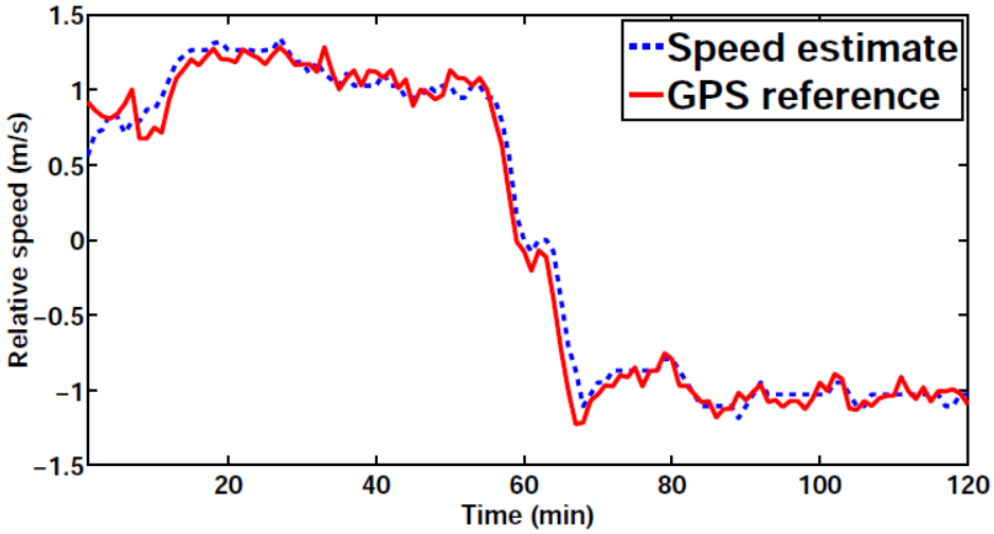

Figure 2-8. The relative speed between the transmitter and receiver array given by GPS and estimated during the temporal resampling stage (courtesy of Milica Stojanovic’s group).

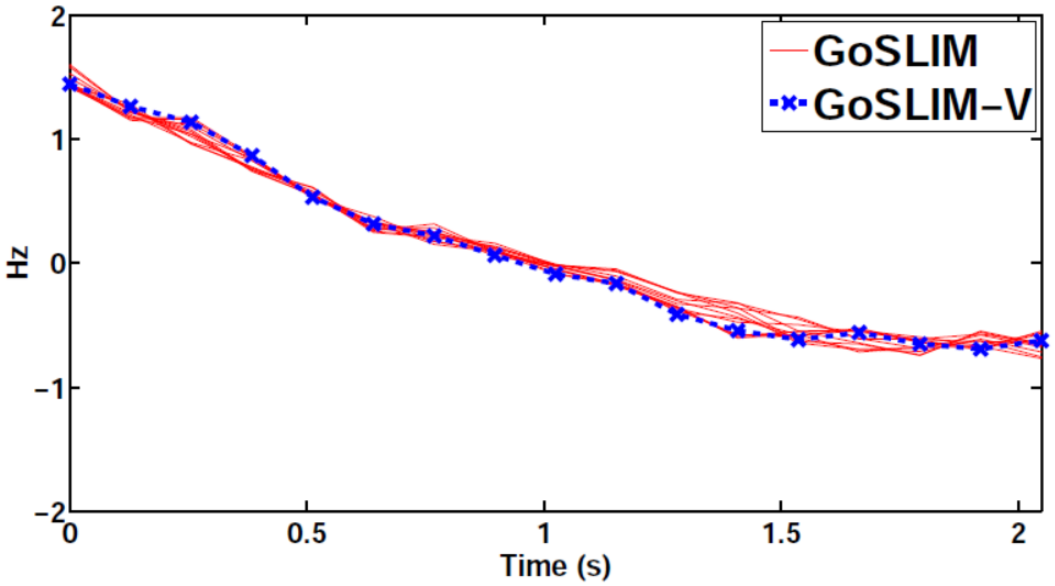

Figure 2-9. Doppler frequency evolution of the 1^{st} packet in epoch “E018” obtained by GoSLIM and GoSLIM-V, respectively.

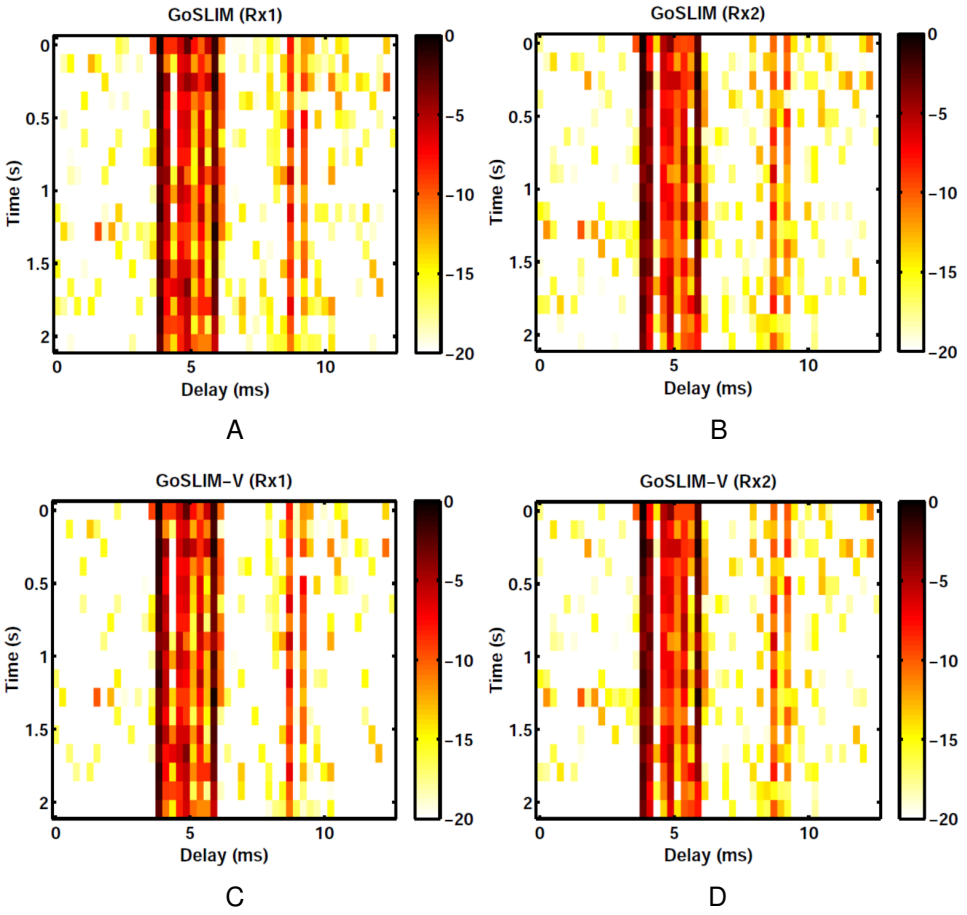

Figure 2-10. A) CIR evolution between the 1st transmitter and the 1st receiver obtained by GoSLIM. B) CIR evolution between the 1st transmitter and the 2nd receiver obtained by GoSLIM. C) CIR evolution between the 1st transmitter and the 1st receiver obtained by GoSLIM-V. D) CIR evolution between the 1st transmitter and the 2nd receiver obtained by GoSLIM-V.

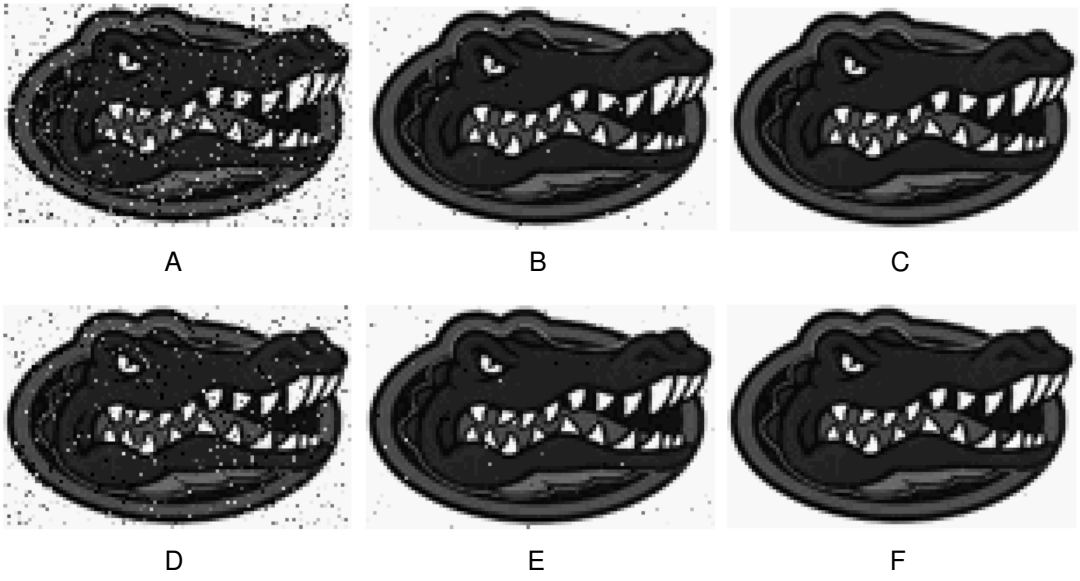

Figure 2-11. A) Grayscale mascot recovered from epoch “E013”. B) Grayscale mascot recovered from epoch “E016”. C) Grayscale mascot recovered from epoch “E018”. D) Grayscale mascot recovered from epoch “E013”. E) Grayscale mascot recovered from epoch “E016”. F) Grayscale mascot recovered from epoch “E018”. A)-C) are obtained by GoSLIM. D)-F) are obtained by GoSLIM-V.

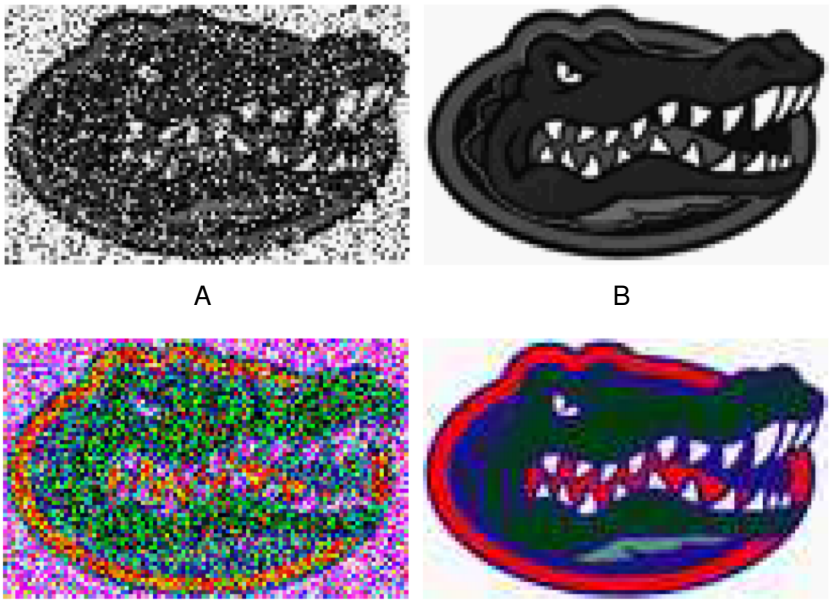

Figure 2-12. A) Grayscale mascot recovered from epoch “E054” using RELAX-BLAST. B) Grayscale mascot recovered from epoch “E054” using Turbo equalization. C) Colored mascot recovered from epoch “E054” using RELAX-BLAST. D) Colored mascot recovered from epoch “E054” using Turbo equalization.

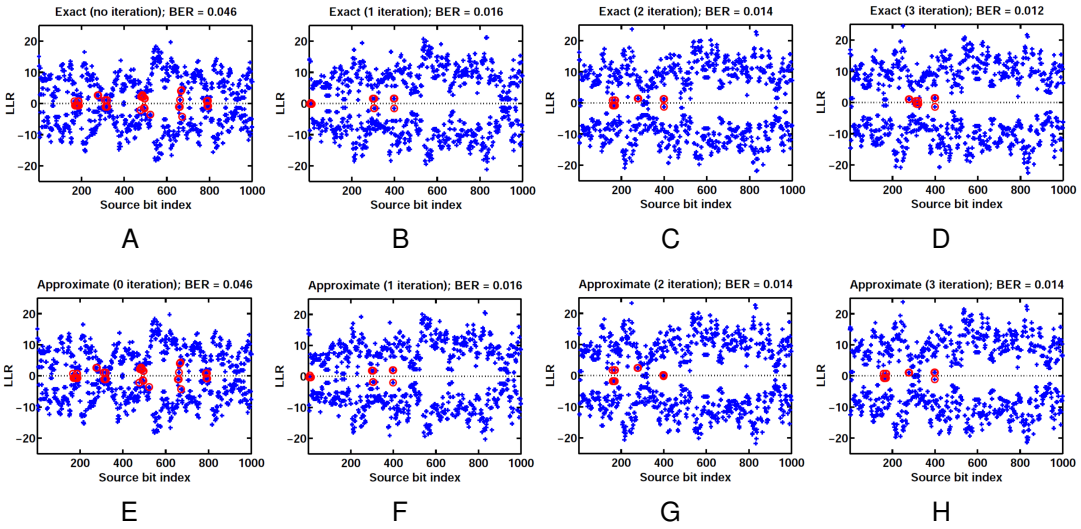

Figure 2-13. The LLR soft information about the source bits at the output of the decoder. A)-D) are obtained by Exact-LMMSE-Turbo from no iteration to 3 iterations, respectively. E)-H) are obtained by Approximate-LMMSE-Turbo from no iteration to 3 iterations, respectively.

CHAPTER 3
ENHANCED MULTISTATIC ACTIVE SONAR SIGNAL PROCESSING

Multistatic active sonar systems involve the transmission and reception of multiple probing sequences and can achieve significantly enhanced performance of target detection and localization through exploiting spatial diversity [42, 43]. The reflected acoustic signals acquired by the receivers carry the range and Doppler information of potential targets, which provides a basis for the estimation of the target parameters, including their positions and velocities [43, 44]. In this chapter, we consider a multistatic active sonar system that employs multiple stationary transmitters and receivers [42]. Two signal processing aspects related to such a system design are addressed, namely target range-Doppler imaging and target parameter estimation.

The receiver filter design plays a critical role in the overall performance of a multistatic active sonar system since it directly determines the quality of range-Doppler imaging and affects the accuracy of the subsequent target parameter estimation. As a classical receiver filter [45, 46], the matched filter is the optimal linear filter for maximizing the signal-to-noise ratio (SNR) for the case of a single target in the presence of additive white noise. However, in a multistatic active sonar system, the multiple simultaneously transmitted probing sequences act as interferences to one another, making the matched filter-based receiver ineffective. Therefore, it is necessary to design more advanced adaptive receiver filters capable of providing range-Doppler images with both low sidelobe levels and high accuracy. In this chapter, we present a hybrid dense-sparse range-Doppler imaging method, which first applies the iterative adaptive approach (IAA) [37] to obtain accurate and dense range-Doppler images, and then achieve sparsity by using one step of the SLIM method [47]. Since SLIM is a maximum *a posteriori* (MAP) approach, we refer to this hybrid method as IAA-MAP. We show that IAA-MAP can improve resolution and reduce sidelobe levels simultaneously while maintaining high accuracy, which is desirable for improved target parameter estimation.

The target parameters are estimated using the peaks (after the direct blasts are removed) of the range-Doppler images. However, in the presence of multiple targets in the field of view, each peak needs to be associated with a specific target. The failure in associating the said peaks with the targets could cause severe performance degradations [48]. This association problem can also be viewed as a range fitting problem. This is a combinatorial optimization problem involving both the peak association and target position estimation. To efficiently solve this problem, we develop a generalized K-Means clustering (GKC) method for peak association, which iteratively solves an optimization problem. Each iteration consists of two steps, the "Means" update step, where the target position is estimated for the current association pattern, and the Label assignment step, where the association pattern is selected based on the current target position estimates. (We remark that if each of the receivers is equipped with a large array that can provide accurate angle estimates of the targets, the peak association problem becomes an easy problem or even disappears entirely.)

Based on the fact that different transmitter-receiver pairs have different reflection coefficients, we develop an extended invariance principle-based weighted least-squares (EXIP-WLS) method for target position determination (which is the aforementioned "Means" update step) and velocity estimation. More specifically, nonlinear algebraic position equations are approximated as linear ones via Taylor expansion and the target position and velocity estimates are refined in an iterative manner using weighting [49]. The weighting matrices we use are the blocks of the Fisher information matrix (FIM) corresponding to an unstructured data model.

The rest of this chapter is organized as follows. Section 3.1 outlines the multistatic active sonar system model and formulates the problem of interest. Section 3.2 presents the IAA-MAP method for range-Doppler imaging, the GKC method for peak association, and the EXIP-WLS method for target parameter estimation. In Section 3.3, we present the simulation results.

3.1 System Description and Problem Formulation

Consider a two-dimensional (2D) multistatic active sonar system equipped with N stationary transmitters and M stationary receivers with known locations. (Although this chapter pays attention to the 2D case, extension to the three-dimensional (3D) case is straightforward.) Assume further that there are Q moving targets in the region of interest and that their locations and velocities are sought. Denote $\mathbf{t}_n = [x_n^t, y_n^t]^T$, $\mathbf{r}_m = [x_m^r, y_m^r]^T$, and $\boldsymbol{\theta}_q = [x_q^\theta, y_q^\theta]^T$ as the Cartesian coordinate vectors of the n^{th} transmitter, the m^{th} receiver, and the q^{th} target, respectively, for $n = 1, \ldots, N$, $m = 1, \ldots, M$, and $q = 1, \ldots, Q$. Further, denote $s_n(t)$ as the ping sent by the n^{th} transmitter for $n = 1, \ldots, N$. The N pings $\{s_n(t)\}_{n=1}^N$ are transmitted simultaneously and every receiver is assumed to have the perfect knowledge on $\{s_n(t)\}_{n=1}^N$. Figure 3-2 shows a generic sensing scenario for the n^{th} transmitter, the m^{th} receiver, and the q^{th} target, in which $\mathbf{v}_q = [x_q^v, y_q^v]^T$ is the velocity vector of the q^{th} target in the Cartesian coordinate. Additionally,

$$\phi_{q,n} = \cos^{-1}\left(\frac{x_q^\theta - x_n^t}{\|\boldsymbol{\theta}_q - \mathbf{t}_n\|}\right) \tag{3–1}$$

and

$$\varphi_{q,m} = \cos^{-1}\left(\frac{x_q^\theta - x_m^r}{\|\boldsymbol{\theta}_q - \mathbf{r}_m\|}\right) \tag{3–2}$$

are the bearing angles measured from the east to the line connecting $\boldsymbol{\theta}_q$ and $\mathbf{t}_n$ and the line connecting $\boldsymbol{\theta}_q$ and $\mathbf{r}_m$, respectively.

A transmitted signal $s_n(t)$ is reflected on the q^{th} target and the echo is received by the m^{th} receiver. The reflected echo $s_{n,q,m}(t)$ and the transmitted ping $s_n(t)$ are related through:

$$s_{n,q,m}(t) = \kappa_{n,q,m} \cdot s_n\left(\alpha_{n,q,m}\left(t - \tau_{n,q,m}\right)\right). \tag{3–3}$$

Here $\kappa_{n,q,m}$ is the complex-valued reflection coefficient, the propagation time delay

$$\tau_{n,q,m} = \frac{\|\boldsymbol{\theta}_q - \mathbf{t}_n\| + \|\boldsymbol{\theta}_q - \mathbf{r}_m\|}{c} \tag{3–4}$$

is determined as the ratio of the target range to the underwater speed c (the target range is $\|\boldsymbol{\theta}_q - \mathbf{t}_n\| + \|\boldsymbol{\theta}_q - \mathbf{r}_m\|$, which geometrically represents the sum of the distance between the n^{th} transmitter and the q^{th} target and the distance between the q^{th} target and the m^{th} receiver), and

$$\alpha_{n,q,m} = \frac{c + x_q^v \cos\phi_{q,n} + y_q^v \sin\phi_{q,n}}{c - x_q^v \cos\varphi_{q,m} - y_q^v \sin\varphi_{q,m}} \tag{3–5}$$

is the Doppler scaling factor (please refer to Appendix A for its derivation).

In addition to the target reflections, the received measurements are also subject to direct blasts, which are the transmitted signals propagating directly from the transmitters to the receivers [43]. The direct blast from the n^{th} transmitter to the m^{th} receiver, say $s_{n,m}(t)$, can be written as:

$$s_{n,m}(t) = \kappa_{n,m} \cdot s_n\left(t - \tau_{n,m}\right). \tag{3–6}$$

Note that the direct blast does not suffer from Doppler scaling for stationary transmitter and receiver platforms, and thus it is characterized by only the complex amplitude $\kappa_{n,m}$ and time delay $\tau_{n,m}$. Intensity-wise, the direct blasts tend to be much stronger than the target reflections [43].

By taking into account the contributions from all of the N transmitters and Q targets, the received signal $y_m(t)$ acquired at the m^{th} receiver can be represented as:

$$y_m(t) = \sum_{n=1}^{N}\sum_{q=1}^{Q} s_{n,q,m}(t) + \sum_{n=1}^{N} s_{n,m}(t) + e_m(t), \quad m = 1, \ldots, M, \tag{3–7}$$

where $e_m(t)$ represents the additive noise. The main goal of this chapter is to recover the target positions and velocities from the transmitted signals $\{s_n(t)\}_{n=1}^{N}$ and the received measurements $\{y_m(t)\}_{m=1}^{M}$.

3.2 Proposed Algorithms

In this section, we first present the IAA-MAP method for range-Doppler imaging to obtain the range and Doppler estimates of the targets. Then the GKC method is

introduced to associate these orderless range estimates with the corresponding targets and the EXIP-WLS method is presented to estimate the target positions and velocities.

3.2.1 Range-Doppler Imaging

In this subsection, we focus on the estimating the ranges and Dopplers of the targets, i.e., the range-Doppler imaging problem, where targets are characterized by the time delay (range)-Doppler pair instead of the position-velocity pair.

3.2.1.1 Imaging problem formulation

The time delay and Doppler regions of interest are divided into R and L points respectively, hence there are RL pixels in the range-Doppler image. Let $\{\tau_r, \alpha_l\}$ be the time delay-Doppler pair of the potential target and $\kappa_{n,m,r,l}$ be the target reflection coefficient associated with the $\{\tau_r, \alpha_l\}$ pair and with respect to the n^{th} transmitter and the m^{th} receiver. Then the received signal $y_m(t)$ acquired at the m^{th} receiver can be rewritten according to $\{\kappa_{n,m,r,l}, \tau_r, \alpha_l\}$ as

$$y_m(t) = \sum_{n=1}^{N} \sum_{r=1}^{R} \sum_{l=1}^{L} s_{n,m,r,l}(t) + e_m(t), \tag{3–8}$$

where

$$s_{n,m,r,l}(t) = \kappa_{n,m,r,l} \cdot s_n(\alpha_l(t - \tau_r)) \tag{3–9}$$

is the reflected echo corresponding to the n^{th} transmitted ping $s_n(t)$ and the $\{\tau_r, \alpha_l\}$ pair. The direct blasts (see (3–6)) are also contained in (3–8), where the related Doppler scaling factors are equal to 1. Note that in general RL is much larger than the actual number of the targets Q and thus only a few components of $\{\kappa_{n,m,r,l}\}$ will be non-zero.

Let $\tilde{\mathbf{s}}_{n,l} = [s_{n,l}(1), \cdots, s_{n,l}(P_l)]^T$ be the sampled sequence with length P_l of the Doppler-scaled signal $s_n(\alpha_l t)$ for the l^{th} Doppler bin. In addition, let d_m is the length of the sampled received signal $y_m(t)$ and $\tilde{\tau}_r$ is the rounded ratio of τ_r to the sampling

period. Thus, the sampled version of $s_n(\alpha_l(t-\tau_r))$ can be expressed in terms of $\tilde{\mathbf{s}}_{n,l}$ as

$$\begin{aligned}\mathbf{s}_{n,m,r,l} &= [s_{n,m,r,l}(1), s_{n,m,r,l}(2), \ldots, s_{n,m,r,l}(d_m)]^T \\ &= \begin{bmatrix} \mathbf{0}_{\tilde{\tau}_r \times P_l} & \mathbf{0}_{\tilde{\tau}_r \times (d_m - P_l)} \\ \mathbf{I}_{P_l \times P_l} & \mathbf{0}_{P_l \times (d_m - P_l)} \\ \mathbf{0}_{(d_m - P_l - \tilde{\tau}_r) \times P_l} & \mathbf{0}_{(d_m - P_l - \tilde{\tau}_r) \times (d_m - P_l)} \end{bmatrix} \begin{bmatrix} \tilde{\mathbf{s}}_{n,l} \\ \mathbf{0}_{(d_m - P_l) \times 1} \end{bmatrix} \end{aligned} \tag{3–10}$$

Then the sampled version of $y_m(t)$ is given by

$$\begin{aligned}\mathbf{y}_m &= [y_m(1), y_m(2), \ldots, y_m(d_m)]^T \\ &= \sum_{n=1}^{N} \sum_{r=1}^{R} \sum_{l=1}^{L} \kappa_{n,m,r,l} \cdot \mathbf{s}_{n,m,r,l} + \mathbf{e}_m, \end{aligned} \tag{3–11}$$

where $\mathbf{e}_m \in \mathbb{C}^{d_m \times 1}$ is the sampled version of $e_m(t)$. In order to write this more compactly, define

$$\begin{aligned} \boldsymbol{\kappa}_{n,m,l} &= [\kappa_{n,m,1,l}, \cdots, \kappa_{n,m,R,l}]^T, \\ \boldsymbol{\kappa}_{n,m} &= [\boldsymbol{\kappa}_{n,m,1}^T, \cdots, \boldsymbol{\kappa}_{n,m,L}^T]^T, \\ \boldsymbol{\kappa}_{m} &= [\boldsymbol{\kappa}_{1,m}^T, \cdots, \boldsymbol{\kappa}_{N,m}^T]^T, \end{aligned} \tag{3–12}$$

and similarly, define

$$\begin{aligned} \mathbf{S}_{n,m,l} &= [\mathbf{s}_{n,m,1,l}, \cdots, \mathbf{s}_{n,m,R,l}], \\ \mathbf{S}_{n,m} &= [\mathbf{S}_{n,m,1}, \cdots, \mathbf{S}_{n,m,L}], \\ \mathbf{S}_{m} &= [\mathbf{S}_{1,m}, \cdots, \mathbf{S}_{N,m}]. \end{aligned} \tag{3–13}$$

Thus, $\mathbf{y}_m$ can be rewritten as

$$\begin{aligned}\mathbf{y}_m &= \sum_{n=1}^{N} \mathbf{S}_{n,m} \boldsymbol{\kappa}_{n,m} + \mathbf{e}_m \\ &= \mathbf{S}_m \boldsymbol{\kappa}_m + \mathbf{e}_m, \end{aligned} \tag{3–14}$$

where $\mathbf{S}_m \in \mathbb{C}^{d_m \times NRL}$ and $\boldsymbol{\kappa}_m \in \mathbb{C}^{NRL \times 1}$.

Equation (3–14) may be viewed as a sparse representation problem, where a sparse vector $\boldsymbol{\kappa}_m$ is sought given the measurement vector $\mathbf{y}_m$ and the dictionary $\mathbf{S}_m$. Once the vector $\boldsymbol{\kappa}_{n,m}$ defined in (3–12) is obtained, the range-Doppler image of size $R \times L$ is formed with respect to the n^{th} transmitter and the m^{th} receiver. Hence, we can form a total of MN range-Doppler images from $\{\mathbf{y}_m\}_{m=1}^{M}$. The M sets of N range-Doppler images can be formed in parallel.

3.2.1.2 Receiver filter for range-Doppler imaging

Herein we address the range-Doppler imaging problem at the m^{th} receiver, the same methodology can be readily applied to other receivers directly. Four different receiver filters, namely matched filter, IAA, SLIM, and IAA-MAP are presented below to estimate $\boldsymbol{\kappa}_m$.

Matched Filter (MF): As one of the classical receiver filters for the active sensing applications [45, 46], the matched filter (MF) correlates the received signal with the time-aligned and Doppler-scaled version of the transmitted ping, i.e.,

$$\hat{\kappa}_{n,m,r,l} = \frac{\mathbf{s}_{n,m,r,l}^H \mathbf{y}_m}{\mathbf{s}_{n,m,r,l}^H \mathbf{s}_{n,m,r,l}}, \quad n = 1, \ldots, N, \quad r = 1, \ldots, R, \quad l = 1, \ldots, L. \tag{3–15}$$

In a single-transmitter single-target case, MF is the optimal receiver filter for maximizing the SNR in the presence of additive white noise. However, in multistatic active sonar systems, the multiple simultaneously transmitted probing sequences act as interferences to one another, making the performance of MF unsatisfactory.

Iterative Adaptive Approach (IAA): As one of the nonparametric methods, the iterative adaptive approach (IAA) [37] has been shown to possess superior performance in a wide variety of applications, including passive array processing [37], underwater acoustic communications [50], and MIMO radar imaging [51].

The IAA algorithm obtains $\boldsymbol{\kappa}_m$ by iteratively solving the following weighted least squares problem:

$$\min_{\kappa_{n,m,r,l}} ||\mathbf{y}_m - \kappa_{n,m,r,l}\mathbf{s}_{n,m,r,l}||^2_{\mathbf{Q}^{-1}_{n,m,r,l}}, \quad n = 1, \ldots, N, \quad r = 1, \ldots, R, \quad l = 1, \ldots, L, \tag{3–16}$$

where $||\mathbf{u}||^2_{\mathbf{Q}^{-1}} \triangleq \mathbf{u}^H\mathbf{Q}^{-1}\mathbf{u}$. In (3–16), the interference and noise covariance matrix $\mathbf{Q}_{n,m,k,l}$ is given by:

$$\mathbf{Q}_{n,m,r,l} = \mathbf{R}_m - |\kappa_{n,m,r,l}|^2\mathbf{s}_{n,m,r,l}\mathbf{s}^H_{n,m,r,l}, \tag{3–17}$$

where

$$\mathbf{R}_m = \sum_{n=1}^{N}\sum_{r=1}^{R}\sum_{l=1}^{L}|\kappa_{n,m,r,l}|^2\mathbf{s}_{n,m,r,l}\mathbf{s}^H_{n,m,r,l}. \tag{3–18}$$

The minimization of (3–16) with respect to $\kappa_{n,m,r,l}$ gives:

$$\hat{\kappa}_{n,m,r,l} = \frac{\mathbf{s}^H_{n,m,r,l}\mathbf{Q}^{-1}_{n,m,r,l}\mathbf{y}_m}{\mathbf{s}^H_{n,m,r,l}\mathbf{Q}^{-1}_{n,m,r,l}\mathbf{s}_{n,m,r,l}}, \quad n = 1, \ldots, N, \quad r = 1, \ldots, R, \quad l = 1, \ldots, L, \tag{3–19}$$

By using the definition of $\mathbf{Q}_{n,m,r,l}$ in (3–17) and the matrix inversion lemma, (3–19) can be rewritten as:

$$\hat{\kappa}_{n,m,r,l} = \frac{\mathbf{s}^H_{n,m,r,l}\mathbf{R}^{-1}_m\mathbf{y}_m}{\mathbf{s}^H_{n,m,r,l}\mathbf{R}^{-1}_m\mathbf{s}_{n,m,r,l}}, \quad n = 1, \ldots, N, \quad r = 1, \ldots, R, \quad l = 1, \ldots, L, \tag{3–20}$$

which avoids the computation of $\mathbf{Q}_{n,m,r,l}$ for $n = 1, \ldots, N$, $r = 1, \ldots, R$, and $l = 1, \ldots, L$ (i.e., NRL times in total), and thus significantly reduces the computational complexity. Once $\mathbf{R}_m$ is available, $\kappa_{n,m,r,l}$ for $n = 1, \ldots, N$, $r = 1, \ldots, R$, and $l = 1, \ldots, L$ can be computed in parallel. Since (3–20) requires $\mathbf{R}_m$, which in turn depends on the unknown target parameters (see (3–18)), IAA needs to be implemented in an iterative manner. Empirical results show that IAA, initialized with the MF output in (3–15), typically converges in no more than 15 iterations (a local convergence proof for IAA is given in [51]).

Sparse learning via iterative minimization (SLIM): As one of the sparse signal recovery approaches, the sparse learning via iterative minimization (SLIM) method

(referred to as SLIM-1 in [47]) considers the following hierarchical Bayesian model:

$$\mathbf{y}_m|\boldsymbol{\kappa}_m, \eta_m \sim \mathcal{CN}(\mathbf{S}_m\boldsymbol{\kappa}_m, \eta_m\mathbf{I}), \tag{3–21}$$

$$\boldsymbol{\kappa}_m|\mathbf{p}_m \sim \mathcal{CN}(\mathbf{0}, \mathbf{P}_m), \tag{3–22}$$

$$p_{n,m,r,l} \sim \mathcal{G}(2,1), \quad n = 1, \ldots, N, \quad r = 1, \ldots, R, \quad l = 1, \ldots, L, \tag{3–23}$$

where $\mathbf{p}_m = [p_{1,m,1,1}, \cdots, p_{N,m,R,L}]$, $\mathbf{P}_m = \text{diag}\{\mathbf{p}_m\}$, and the *a priori* probability density function of η_m is assumed to be flat, i.e., $f(\eta_m) \propto 1$.

Thus, the objective function for SLIM can be represented as:

$$\max_{\boldsymbol{\kappa}_m, \mathrm{p}_m, \eta_m} p(\boldsymbol{\kappa}_m, \mathbf{p}_m, \eta_m|\mathbf{y}_m) = \max_{\boldsymbol{\kappa}_m, \mathrm{p}_m, \eta_m} p(\mathbf{y}_m|\boldsymbol{\kappa}_m, \eta_m)p(\boldsymbol{\kappa}_m|\mathbf{p}_m)\prod_{n=1}^{N}\prod_{r=1}^{R}\prod_{l=1}^{L} p(p_{n,m,r,l}). \tag{3–24}$$

By combining (3–21)–(3–24), the optimization problem formulated in (3–24) can be rewritten in a negative logarithm form as:

$$\min_{\boldsymbol{\kappa}_m, \mathrm{P}_m, \eta_m} \left(d_m \log \eta_m + \frac{\|\mathbf{y}_m - \mathbf{S}_m\boldsymbol{\kappa}_m\|^2}{\eta_m} + \sum_{n=1}^{N}\sum_{r=1}^{R}\sum_{l=1}^{L} \frac{|\kappa_{n,m,r,l}|^2}{p_{n,m,r,l}} + \sum_{n=1}^{N}\sum_{r=1}^{R}\sum_{l=1}^{L} p_{n,m,r,l} \right). \tag{3–25}$$

Besides the target reflection coefficient vector $\boldsymbol{\kappa}_m$, the cost function introduces the covariance matrix $\mathbf{P}_m$ (or equivalently, its diagonal elements in $\mathbf{p}_m$) and the noise power η_m. We solve (3–25) by using the following cyclic approach: at each iteration, one of the parameter vectors $\boldsymbol{\kappa}_m$, $\mathbf{p}_m$, and η_m is updated while keeping the other two fixed. SLIM keeps iterating until a predefined number of iterations is reached or until convergence. The three steps of the SLIM algorithm at the ith iteration are outlined below:

1. Given $\mathbf{P}_m^{(i-1)}$ and $\eta_m^{(i-1)}$ from the previous SLIM iteration, setting the partial derivative of (3–25) with respect to $\boldsymbol{\kappa}_m^H$ to 0 yields the optimal $\boldsymbol{\kappa}_m^{(i)}$

$$\boldsymbol{\kappa}_m^{(i)} = \mathbf{P}_m^{(i-1)}\mathbf{S}_m^H\left[\eta_m^{(i-1)}\mathbf{I} + \mathbf{S}_m\mathbf{P}_m^{(i-1)}\mathbf{S}_m^H\right]^{-1}\mathbf{y}_m. \tag{3–26}$$

2. Once $\boldsymbol{\kappa}_m^{(i)}$ is available, by taking the partial derivation of (3–25) with respect to $p_{n,m,r,l}$ and setting the result to zero, the optimal $p_{n,m,r,l}$ is obtained as

$$p_{n,m,r,l}^{(i)} = \left|\kappa_{n,m,r,l}^{(i)}\right|, \quad n = 1, \ldots, N, \quad r = 1, \ldots, R, \quad l = 1, \ldots, L. \tag{3–27}$$

3. Using the most recently obtained $\boldsymbol{\kappa}_m^{(i)}$, we finally estimate the noise power by taking the partial derivation of (3–25) with respect to η_m and the solution is given by:

$$\eta_m^{(i)} = \frac{1}{d_m} \left\| \mathbf{y}_m - \mathbf{S}_m \boldsymbol{\kappa}_m^{(i)} \right\|^2 . \tag{3–28}$$

It generally takes SLIM no more than 15 iterations to converge [47].

IAA-MAP: IAA and SLIM methods possess various merits and limitations, with IAA being dense and accurate and SLIM being sparse and biased downward. Below, we consider a hybrid method that takes advantages of these merits while overcoming the limitations of the separate methods. Indeed, IAA is a nonparametric, robust, and user parameter free algorithm, which has also been found to be more accurate than the corresponding SLIM estimates, although with a notably higher sidelobe level. In order to achieve sidelobe levels comparable to those of SLIM, one may instead form a hybrid approach that first uses IAA to compute a dense range-Doppler image, which is then, upon convergence, followed by a single step of SLIM-0 [47]:

$$\hat{\kappa}_{n,m,r,l} = \left| \hat{\kappa}_{n,m,r,l}^{(\mathrm{IAA})} \right|^2 \mathbf{s}_{n,m,r,l}^H \left[\mathbf{R}_m^{(\mathrm{IAA})} \right]^{-1} \mathbf{y}_m, \qquad n = 1, \ldots, N, \quad r = 1, \ldots, R, \quad l = 1, \ldots, L, \tag{3–29}$$

where $\hat{\kappa}_{n,m,r,l}^{(\mathrm{IAA})}$ and $\mathbf{R}_m^{(\mathrm{IAA})}$ denote the corresponding estimates obtained at the conclusion of the IAA iterations.

Since SLIM achieves sparsity based on solving a hierarchical Bayesian model through maximizing *a posteriori* probability density function [47], this single step of SLIM-0 is referred to as a MAP step, and the resulting algorithm as the IAA-MAP algorithm. Compared to SLIM-1, SLIM-0 provides sparser results but is more sensitive to noise and disturbances. IAA tends to be more robust against noise and disturbances than SLIM. Due to the accurate and robust IAA result and a single step of SLIM-0, IAA-MAP is robust, sparse and accurate. The merits of IAA-MAP are desirable for achieving improved target parameter estimation.

3.2.2 Generalized K-Means Clustering (GKC) Association Method

Given the range-Doppler images, we use a model-order selection tool, i.e., the Bayesian information criterion (BIC) [52, 53], to estimate the target number and locate the corresponding peaks before moving on to the task of target parameter estimation. For ease of exposition, we assume that we can successfully locate the Q peaks (each corresponds to one target) on each one of the NM range-Doppler images and the range estimates obtained from those peaks are utilized to estimate the target positions. We remark that the proposed association scheme can be easily modified to suit more complicated cases, i.e., when the estimated target numbers for all transmitter-receiver pairs are not equal to the true target number Q.

As shown in Figure 3-2, the target position cannot be uniquely determined from the range value and the positions of a single transmitter and receiver pair. Rather, the target could be at any point on an ellipse. In a 2D multistatic active sonar system equipped with N transmitters and M receivers, it is well-known that unique target position estimation in general requires at least three range values (or equivalently, three ellipses) [49], i.e., $NM \geq 3$. Additionally, more range measurements can yield more accurate target position estimates. Therefore, we collect range information from all of the NM images to determine the position of a target.

However, when there are multiple targets in the field of interest, we need to solve the target association problem, which aims to determine a proper one-to-one correspondence between the Q targets and the Q peaks of each range-Doppler image. To describe the problem more clearly, we take the imaging results shown in Figure 3-3 as an example, where there are two transmitters, two receivers, and two targets, i.e., $\{N = 2, M = 2, Q = 2\}$. If we assign Label 1, i.e., the 1^{st} target, to the peak at the right-hand side of the first subfigure, then we need to determine which three peaks in the rest of the three subfigures correspond to the same target. Given an assumed association pattern, all the range values obtained from peaks that are assigned to a

specific target are collected to estimate the target position and the incorrect association assumption would lead to severe performance degradations. Therefore, solving the association problem plays a critical role in the overall performance of the sonar system in the presence of multiple targets and in the absence of target angle estimates.

A possible answer is the brute-force association (BFA), which estimates the target positions for every possible association pattern (to be more exact, there are a total of $(Q!)^{NM-1}$ association patterns that need to be checked), and then selects the association pattern that yields the minimum cost value as the optimal one. Although conceptionally simple, the BFA approach is computationally intensive (NP-hard).

To alleviate the computational burden, we develop a new association method, inspired by the K-Means clustering (KMC) idea in the machine learning field [54], as a generalization of the conventional KMC method, and referred to as the GKC method. This clustering-based method aims to partition all the NMQ range measurements into Q classes, and ensures that: i) each class contains NM samples (i.e., range values); ii) the Q range measurements obtained from the peaks of each range-Doppler image have different labels $(1, 2, \ldots, Q)$; and iii) the range estimates assigned to the same label correspond to a unique target. Let $\{\rho_{n,q,m}\}$ denote a collection of target range estimates obtained from the range-Doppler images, the GKC method can then be formulated to solve the following optimization problem:

$$\min \quad \sum_{i=1}^{Q}\sum_{q=1}^{Q}\sum_{n=1}^{N}\sum_{m=1}^{M}\delta(i,q,n,m)\left|\rho_{n,q,m}-\left(\|\boldsymbol{\theta}_i-\mathbf{t}_n\|+\|\boldsymbol{\theta}_i-\mathbf{r}_m\|\right)\right|, \tag{3–30}$$

where $\delta(i,q,n,m)=1$ if and only if $\rho_{n,q,m}$ is classified into the ith class; otherwise, $\delta(i,q,n,m)=0$. Equation (3–30) implies that this is actually a range fitting problem, and only the correct association pattern and target position estimation are able to provide the best fit to these range estimates. Therefore, it is a combined optimization problem of the peak association and target position estimation. From the clustering point of view, the range estimate $\rho_{n,q,m}$ and $\|\boldsymbol{\theta}_i-\mathbf{t}_n\|+\|\boldsymbol{\theta}_i-\mathbf{r}_m\|$ (a function of the

target position) represent a virtual “sample” and a particular “mean”, respectively. In the classical K-Means algorithm, the mean of a class is updated by averaging all samples in this class. However, in the “clustering” problem described herein, the “mean” of a class depends on the related target position, which needs to be estimated before re-assigning these labels. For ease of exposition, a new target position estimation algorithm will be elaborated in the next subsection and the outline of the proposed GKC method, which omits the details of target position estimation, is as follows:

1. *Initialization*: Randomly assign Q ranges estimates (peaks) of each image with labels $1, 2, \ldots, Q$;

2. *Update of “Means”*:
   For $i = 1$ to Q
   From the NM range estimates (or equivalently, “samples” in the machine learning field) assigned to Label i currently, we determine the i^{th} target position denoted as $\hat{\boldsymbol{\theta}}_i$ (the estimation algorithm will be developed in the next subsection);
   Plugging $\hat{\boldsymbol{\theta}}_i$ into $\|\boldsymbol{\theta}_i - \mathbf{t}_n\| + \|\boldsymbol{\theta}_i - \mathbf{r}_m\|$ yields the new “means” $\|\hat{\boldsymbol{\theta}}_i - \mathbf{t}_n\| + \|\hat{\boldsymbol{\theta}}_i - \mathbf{r}_m\|$ for $n = 1, \ldots, N$, and $m = 1, \ldots, M$.

3. *Re-assignment of Labels*:
   For $n = 1, \ldots, N$, $m = 1, \ldots, M$, and $q = 1, \ldots, Q$
   Assign the range estimate $\rho_{n,q,m}$ to the i^{th} class (Label i) if and only if

$$\left|\rho_{n,q,m} - \left(\|\hat{\boldsymbol{\theta}}_i - \mathbf{t}_n\| + \|\hat{\boldsymbol{\theta}}_i - \mathbf{r}_m\|\right)\right| = \min_{p \in (1,2,\ldots,Q)} \left|\rho_{n,q,m} - \left(\|\hat{\boldsymbol{\theta}}_p - \mathbf{t}_n\| + \|\hat{\boldsymbol{\theta}}_p - \mathbf{r}_m\|\right)\right| \tag{3–31}$$

   In the actual implementation, we swap $\rho_{n,q,m}$ and $\rho_{n,i,m}$ (after the re-assignment of $\rho_{n,q,m}$ to the i^{th} class), for $q = 1, \ldots, Q$ successively, to ensure that $\rho_{n,q,m}$ always represents the range estimate corresponding to the q^{th} target after Step 3.

4. *Repeat Steps 2 and 3 until convergence*.

The proposed GKC approach is more efficient than the BFA method because the latter considers all possible associations while the former initializes with one candidate and converge to the correct association pattern after a few iterations. We remark that if the target number estimates obtained via BIC are different for different range-Doppler images, the final target number estimate $\hat{Q}$ can be determined according to some

add-hoc criterion and then the GKC approach can be easily modified to be applicable to this case.

3.2.3 EXIP-WLS Method for Target Position Estimation

In this subsection, we apply the EXtended Invariance Principle (EXIP) [55] to estimate $\boldsymbol{\theta}_q$ from the NM range estimates $\rho_{n,q,m}(\boldsymbol{\theta}_q)$ assigned to Label q. We will focus on estimating the position parameters of the q^{th} target throughout this subsection and the same methodology can be readily applied to deal with other targets in a straightforward manner.

Theorem 1: Assume that a one-to-one function f exists and satisfies

$$\boldsymbol{\xi} = f(\boldsymbol{\theta}) \in D_{\boldsymbol{\xi}}, \qquad \forall \boldsymbol{\theta} \in D_{\boldsymbol{\theta}}, \tag{3–32}$$

where the sets $D_{\boldsymbol{\xi}}$ and $D_{\boldsymbol{\theta}}$ represents the domain of the generic parameter vectors $\boldsymbol{\xi}$ and $\boldsymbol{\theta}$, respectively.

If

$$\lim_{Ł\to\infty} \hat{\boldsymbol{\xi}} = \lim_{Ł\to\infty} f(\hat{\boldsymbol{\theta}}), \tag{3–33}$$

then

$$\hat{\hat{\boldsymbol{\theta}}} = \arg\min_{\boldsymbol{\theta}} \left[\hat{\boldsymbol{\xi}} - f(\boldsymbol{\theta})\right]^T \mathbf{W} \left[\hat{\boldsymbol{\xi}} - f(\boldsymbol{\theta})\right] \tag{3–34}$$

is asymptotically (when the number of data samples Ł is large) equivalent to the estimate $\hat{\boldsymbol{\theta}}$, with

$$\mathbf{W} = E\left[\frac{\partial^2 V(\boldsymbol{\xi})}{\partial \boldsymbol{\xi} \partial \boldsymbol{\xi}^T}\right]\Big|_{\boldsymbol{\xi}=\hat{\boldsymbol{\xi}}}, \tag{3–35}$$

where $E[\cdot]$ denotes the expectation operation and $V(\boldsymbol{\xi})$ represents a loss function that can be parameterized in terms of $\boldsymbol{\xi}$. The related proof can be found in [55].

The weighting matrix $\mathbf{W} \in \mathcal{R}^{(NM)\times(NM)}$ can be obtained from the corresponding block of FIM that is related to the signal parameter vector $\boldsymbol{\xi}$; see Appendix B for more details on this subject.

Based on EXIP, we define

$$\boldsymbol{\xi}_1 = \begin{bmatrix} \rho_{1,q,1} \cdots \rho_{N,q,1} & \rho_{1,q,2} \cdots \rho_{N,q,M} \end{bmatrix}^T \tag{3–36}$$

as the parameter vector of the unstructured model, which can be obtained from range-Doppler imaging results. In addition,

$$f_1(\boldsymbol{\theta}_q) = \begin{bmatrix} \|\boldsymbol{\theta}_q - \mathbf{t}_1\| + \|\boldsymbol{\theta}_q - \mathbf{r}_1\| \\ \vdots \\ \|\boldsymbol{\theta}_q - \mathbf{t}_N\| + \|\boldsymbol{\theta}_q - \mathbf{r}_1\| \\ \|\boldsymbol{\theta}_q - \mathbf{t}_1\| + \|\boldsymbol{\theta}_q - \mathbf{r}_2\| \\ \vdots \\ \|\boldsymbol{\theta}_q - \mathbf{t}_N\| + \|\boldsymbol{\theta}_q - \mathbf{r}_M\| \end{bmatrix} \tag{3–37}$$

is the one-to-one function of the parameter vector $\boldsymbol{\theta}_q$ in the unstructured model (see the definition of the structured and unstructured models in Appendix B, or refer to [55] for more details).

Equation (3–34) provides an estimate of $\boldsymbol{\theta}_q$ that is asymptotically equivalent to the maximum likelihood estimate of the structured model. However, it is a nonlinear function of $\boldsymbol{\theta}_q$ and thus a search over a two-dimensional space is required.

To avoid such a computationally intensive search, we approximate these nonlinear equations using only the linear parts of their Taylor expansion to refine the target position estimate in an iterative manner, and develop an EXIP-based iterative and weighted least square (EXIP-WLS) method for target position estimation.

Given an initial guess of the target location, denoted as $\hat{\boldsymbol{\theta}}_q = [\hat{x}_q \quad \hat{y}_q]^T$, and the error $\boldsymbol{\Delta}_q^{\theta}$ between the true target position $\boldsymbol{\theta}_q$ and the estimate $\hat{\boldsymbol{\theta}}_q$ can be given by

$$\boldsymbol{\Delta}_q^{\theta} = \boldsymbol{\theta}_q - \hat{\boldsymbol{\theta}}_q. \tag{3–38}$$

Thus, the true target range $\|\boldsymbol{\theta}_q - \mathbf{t}_n\| + \|\boldsymbol{\theta}_q - \mathbf{r}_m\|$ can be represented in its Taylor expansion form as:

$$\begin{aligned}
&\|\boldsymbol{\theta}_q - \mathbf{t}_n\| + \|\boldsymbol{\theta}_q - \mathbf{r}_m\| \\
=&\|\hat{\boldsymbol{\theta}}_q - \mathbf{t}_n\| + \|\hat{\boldsymbol{\theta}}_q - \mathbf{r}_m\| + \left(\boldsymbol{\Delta}_q^{\theta}\right)^T \left[\nabla\Big(\|\hat{\boldsymbol{\theta}}_q - \mathbf{t}_n\| + \|\hat{\boldsymbol{\theta}}_q - \mathbf{r}_m\|\Big)\right] + \dots \\
\approx&\|\hat{\boldsymbol{\theta}}_q - \mathbf{t}_n\| + \|\hat{\boldsymbol{\theta}}_q - \mathbf{r}_m\| + \left(\boldsymbol{\Delta}_q^{\theta}\right)^T \left[\nabla\Big(\|\hat{\boldsymbol{\theta}}_q - \mathbf{t}_n\| + \|\hat{\boldsymbol{\theta}}_q - \mathbf{r}_m\|\Big)\right]
\end{aligned} \tag{3–39}$$

where $\nabla(\cdot)$ denotes the gradient vector. In (3–39), the nonlinear terms after the first-order derivatives are truncated, and

$$\begin{aligned}
&\nabla\Big(\|\hat{\boldsymbol{\theta}}_q - \mathbf{t}_n\| + \|\hat{\boldsymbol{\theta}}_q - \mathbf{r}_m\|\Big) \\
=&\left[\frac{\partial\Big(\|\hat{\boldsymbol{\theta}}_q - \mathbf{t}_n\| + \|\hat{\boldsymbol{\theta}}_q - \mathbf{r}_m\|\Big)}{\partial \hat{x}_q^{\theta}}, \ \frac{\partial\Big(\|\hat{\boldsymbol{\theta}}_q - \mathbf{t}_n\| + \|\hat{\boldsymbol{\theta}}_q - \mathbf{r}_m\|\Big)}{\partial \hat{y}_q^{\theta}}\right]^T \\
=&\left[\cos\hat{\phi}_{q,n} + \cos\hat{\varphi}_{q,m}, \ \ \sin\hat{\phi}_{q,n} + \sin\hat{\varphi}_{q,m}\right]^T,
\end{aligned} \tag{3–40}$$

where the bearing angles $\{\hat{\phi}_{q,n}\}$ and $\{\hat{\varphi}_{q,m}\}$ are defined in (3–1) and (3–2), respectively, only with the true target position $\boldsymbol{\theta}_q$ replaced by the current estimate $\hat{\boldsymbol{\theta}}_q$.

Define

$$\mathbf{D}_1 = \begin{bmatrix}
\cos\hat{\phi}_{q,1} + \cos\hat{\varphi}_{q,1} & \sin\hat{\phi}_{q,1} + \sin\hat{\varphi}_{q,1} \\
\vdots & \vdots \\
\cos\hat{\phi}_{q,N} + \cos\hat{\varphi}_{q,1} & \sin\hat{\phi}_{q,N} + \sin\hat{\varphi}_{q,1} \\
\cos\hat{\phi}_{q,1} + \cos\hat{\varphi}_{q,2} & \sin\hat{\phi}_{q,1} + \sin\hat{\varphi}_{q,2} \\
\vdots & \vdots \\
\cos\hat{\phi}_{q,N} + \cos\hat{\varphi}_{q,M} & \sin\hat{\phi}_{q,N} + \sin\hat{\varphi}_{q,M}
\end{bmatrix} \tag{3–41}$$

and

$$\mathbf{a}_1 = \boldsymbol{\xi}_1 - f_1(\hat{\boldsymbol{\theta}}_q). \tag{3–42}$$

Let $\mathbf{W}_1$ be the block matrix of FIM that is related to the signal parameter vector $\boldsymbol{\xi}_1$ (see Appendix B for more details on how to obtain $\mathbf{W}_1$). Then (3–34) can be approximately

transformed into the following problem:

$$\hat{\mathbf{\Delta}}_q^{\theta} = \arg\min_{\mathbf{\Delta}_q^{\theta}} \left[\mathbf{a}_1 - \mathbf{D}_1\mathbf{\Delta}_q^{\theta}\right]^T \mathbf{W}_1 \left[\mathbf{a}_1 - \mathbf{D}_1\mathbf{\Delta}_q^{\theta}\right]. \tag{3–43}$$

The solution to (3–43) is given by

$$\hat{\mathbf{\Delta}}_q^{\theta} = \left(\mathbf{D}_1^T\mathbf{W}_1\mathbf{D}_1\right)^{-1}\mathbf{D}_1^T\mathbf{W}_1\mathbf{a}_1. \tag{3–44}$$

Once $\hat{\mathbf{\Delta}}_q^{\theta}$ is available, the target position estimate is updated as $\hat{\boldsymbol{\theta}}_q + \hat{\mathbf{\Delta}}_q^{\theta}$. To refine the estimate, we repeat the above procedure from (3–41)-(3–44) until convergence (e.g., when $\|\hat{\mathbf{\Delta}}_q^{\theta}\|$ becomes essentially zero).

We remark that when $\mathbf{W}_1 = \mathbf{I}$, the EXIP-WLS-based target position estimation approach degrades into an Unweighted Least Square (ULS) one, which treats all range measurements equally. However, in practice different transmitter-receiver pairs encounter different reflection coefficients. The EXIP-based weighting scheme exploits the fact that not all transmitter-receiver pairs are created equally for a particular target and thus should improve the accuracy of the target position estimation.

3.2.4 EXIP-WLS Method for Target Velocity Estimation

By applying the proposed GKC method, we can jointly obtain the optimal association pattern and the target position estimates which also facilitate the subsequent target velocity estimation. Similarly to the methodology described in Section 3.2.3, we can also apply the extended invariance principle to determine the target velocities given the associated Doppler scaling factor measurements $\alpha_{n,q,m}$ and the target position estimate $\hat{\boldsymbol{\theta}}_q$.

Define

$$\boldsymbol{\xi}_2 = \left[\alpha_{1,q,1} \ldots \alpha_{N,q,1} \quad \alpha_{1,q,2} \ldots \alpha_{N,q,M}\right]^T \tag{3–45}$$

as the related parameter vector of the unstructured model, which can be obtained from the range-Doppler imaging results, and

$$f_2(\mathbf{v}_q) = \begin{bmatrix} \frac{c+x_q^v \cos\phi_{q,1}+y_q^v \sin\phi_{q,1}}{c-x_q^v \cos\varphi_{q,1}-y_q^v \sin\varphi_{q,1}} \\ \vdots \\ \frac{c+x_q^v \cos\phi_{q,N}+y_q^v \sin\phi_{q,N}}{c-x_q^v \cos\varphi_{q,1}-y_q^v \sin\varphi_{q,1}} \\ \frac{c+x_q^v \cos\phi_{q,1}+y_q^v \sin\phi_{q,1}}{c-x_q^v \cos\varphi_{q,2}-y_q^v \sin\varphi_{q,2}} \\ \vdots \\ \frac{c+x_q^v \cos\phi_{q,N}+y_q^v \sin\phi_{q,N}}{c-x_q^v \cos\varphi_{q,M}-y_q^v \sin\varphi_{q,M}} \end{bmatrix}, \tag{3–46}$$

which is a one-to-one function of the parameter vector $\mathbf{v}_q$ in the unstructured model.

Given an initial guess of the target velocity $\hat{\mathbf{v}}_q = [\hat{x}_q^v \quad \hat{y}_q^v]^T$, and the error between the true target velocity $\mathbf{v}_q$ and the estimate $\hat{\mathbf{v}}_q$ is $\boldsymbol{\Delta}_q^v = \mathbf{v}_q - \hat{\mathbf{v}}_q$. Let $\mathbf{W}_2$ be the block matrix of FIM that is related to the signal parameter vector $\boldsymbol{\xi}_2$ (see Appendix B for more details on how to obtain $\mathbf{W}_2$). Then we can solve the velocity estimation problem similarly to that in Section 3.2.3):

$$\hat{\boldsymbol{\Delta}}_q^v = arg \min_{\boldsymbol{\Delta}_q^v} \left[\mathbf{a}_2 - \mathbf{D}_2 \boldsymbol{\Delta}_q^v\right]^T \mathbf{W}_2 \left[\mathbf{a}_2 - \mathbf{D}_2 \boldsymbol{\Delta}_q^v\right], \tag{3–47}$$

where

$$\mathbf{a}_2 = \boldsymbol{\xi}_2 - f_2(\hat{\mathbf{v}}_q), \tag{3–48}$$

and

$$\mathbf{D}_2 = \begin{bmatrix} \frac{(\cos\hat{\phi}_{q,1}+\cos\hat{\varphi}_{q,1})c+\sin(\hat{\phi}_{q,1}-\hat{\varphi}_{q,1})\hat{y}_q^v}{\left(c-\hat{x}_q^v \cos\hat{\varphi}_{q,1}-\hat{y}_q^v \sin\hat{\varphi}_{q,1}\right)^2} & \frac{(\sin\hat{\phi}_{q,1}+\sin\hat{\varphi}_{q,1})c+\sin(\hat{\varphi}_{q,1}-\hat{\phi}_{q,1})\hat{y}_q^v}{\left(c-\hat{x}_q^v \cos\hat{\varphi}_{q,1}-\hat{y}_q^v \sin\hat{\varphi}_{q,1}\right)^2} \\ \vdots & \vdots \\ \frac{(\cos\hat{\phi}_{q,N}+\cos\hat{\varphi}_{q,1})c+\sin(\hat{\phi}_{q,N}-\hat{\varphi}_{q,1})\hat{y}_q^v}{\left(c-\hat{x}_q^v \cos\hat{\varphi}_{q,1}-\hat{y}_q^v \sin\hat{\varphi}_{q,1}\right)^2} & \frac{(\sin\hat{\phi}_{q,N}+\sin\hat{\varphi}_{q,1})c+\sin(\hat{\varphi}_{q,1}-\hat{\phi}_{q,N})\hat{y}_q^v}{\left(c-\hat{x}_q^v \cos\hat{\varphi}_{q,1}-\hat{y}_q^v \sin\hat{\varphi}_{q,1}\right)^2} \\ \frac{(\cos\hat{\phi}_{q,1}+\cos\hat{\varphi}_{q,2})c+\sin(\hat{\phi}_{q,1}-\hat{\varphi}_{q,2})\hat{y}_q^v}{\left(c-\hat{x}_q^v \cos\hat{\varphi}_{q,2}-\hat{y}_q^v \sin\hat{\varphi}_{q,2}\right)^2} & \frac{(\sin\hat{\phi}_{q,1}+\sin\hat{\varphi}_{q,2})c+\sin(\hat{\varphi}_{q,2}-\hat{\phi}_{q,1})\hat{y}_q^v}{\left(c-\hat{x}_q^v \cos\hat{\varphi}_{q,2}-\hat{y}_q^v \sin\hat{\varphi}_{q,2}\right)^2} \\ \vdots & \vdots \\ \frac{(\cos\hat{\phi}_{q,N}+\cos\hat{\varphi}_{q,M})c+\sin(\hat{\phi}_{q,N}-\hat{\varphi}_{q,M})\hat{y}_q^v}{\left(c-\hat{x}_q^v \cos\hat{\varphi}_{q,M}-\hat{y}_q^v \sin\hat{\varphi}_{q,M}\right)^2} & \frac{(\sin\hat{\phi}_{q,N}+\sin\hat{\varphi}_{q,M})c+\sin(\hat{\varphi}_{q,M}-\hat{\phi}_{q,N})\hat{y}_q^v}{\left(c-\hat{x}_q^v \cos\hat{\varphi}_{q,M}-\hat{y}_q^v \sin\hat{\varphi}_{q,M}\right)^2} \end{bmatrix}. \tag{3–49}$$

Note that in (3–48) $\alpha_{n,q,m}$ is replaced by the actual Doppler measurement and $\{\cos\varphi_{q,m}, \sin\varphi_{q,m}, \cos\phi_{q,n}, \sin\phi_{q,n}\}$ is obtained by plugging $\hat{\boldsymbol{\theta}}_q$ into (3–1) and (3–2). In (3–47), only the linear terms of the Taylor expansion are kept and $\mathbf{D}_2$ is the related gradient vector of $f_2(\cdot)$ at $\hat{\mathbf{v}}_q$. Similar iterative and weighted least-squares method is applied to refine the velocity estimate. Specifically, the solution to (3–47) can be given by $\hat{\boldsymbol{\Delta}}_q^v = \left(\mathbf{D}_2^T\mathbf{W}_2\mathbf{D}_2\right)^{-1}\mathbf{D}_2^T\mathbf{W}_2\mathbf{a}_2$, and the target velocity estimate is then updated as $\hat{\mathbf{v}}_q + \hat{\boldsymbol{\Delta}}_q^v$. When $\mathbf{W}_2 = \mathbf{I}$, the EXIP-WLS-based target velocity estimation approach also degenerates into an ULS one. Since the Doppler and range measurements are paired, the velocity and position estimates are paired naturally.

3.3 Simulation Results

Consider a multistatic active sonar system equipped with $N = 2$ transmitters and $M = 2$ receivers. The system geometry is illustrated in Figure 3-1. The coordinate vectors of the two receivers Rx1 and Rx2 are $\mathbf{r}_1 = [2000, 0]^T$ and $\mathbf{r}_2 = [0, 2000]^T$, respectively (the unit of distance is meter). Two transmitters, Tx1 and Tx2, are located at $\mathbf{t}_1 = [0, 0]^T$ and $\mathbf{t}_2 = [2000, 2000]^T$, respectively, and transmit two random phase (RP) sequences simultaneously. The RP sequences are unimodular with phases independently and uniformly distributed over $[0, 2\pi)$. There are $Q = 2$ targets moving in the filed of view. The first target, located at $\boldsymbol{\theta}_1 = [1000, 995]^T$, is moving at a velocity of $\mathbf{v}_1 = [\frac{-1.8}{\sqrt{2}}, \frac{-1.8}{\sqrt{2}}]^T$ knots. The second target is located at $\boldsymbol{\theta}_2 = [1050, 965]^T$ and is moving at $\mathbf{v}_2 = [0, -2]^T$ knots. The Doppler bins correspond to Doppler scaling factors ranging from 0.9976 to 1.0024 with a step size of 0.0003. The zero-mean white Gaussian noise with a power of η_1 or η_2 is added to the measurements acquired at Rx1 or Rx2, respectively. The noise power, the norm of the target reflection coefficients, and the norm of the amplitude and phase modifications associated with the direct blasts are listed in Table 3-1, and the remaining system parameters are summarized in Table 3-2.

3.3.1 Range-Doppler Imaging Results

The receiver outputs are processed using MF, IAA, SLIM, and IAA-MAP. The intensity of all range-Doppler images is normalized so that the peak is at 0 dB and is clipped at -40 dB. For the sake of clarity and also due to the fact that the location of the direct blast in the range-Doppler images is predictable given the positions of the transmitters and receivers, the range-Doppler images presented henceforth show the target range only. Figure 3-4 and Figure 3-5 show the range-Doppler images produced by the four receiver filter designs. The MF images with respect to the two transmitters formed by Rx1 (Rx2) are shown in Figures 3-4A and 3-4B (Figures 3-5A and 3-5B), respectively. One observes that due to the mutual interferences of the target reflections and strong direct blasts, the MF images are mired with background noise, making it difficult to detect the two targets, which is in agreement with the analysis in Section 3.2. The range-Doppler images produced by IAA, SLIM and IAA-MAP are shown in Figures 3-4C-3-4D (Figures 3-5C and 3-5D), Figures 3-4E-3-4F (Figures 3-5E-3-5F) and Figures 3-4G-3-4H (Figures 3-5G-3-5H), respectively. We can see that IAA, SLIM, and IAA-MAP all possess excellent interference suppression capabilities and produce much sharper images than MF. In particular, IAA can provide quite accurate estimation results, but the resulting dense sidelobes may bury targets with weak reflection coefficients. In contrast, SLIM enforces sparsity and provides range-Doppler images with much less sidelobes than IAA. As the hybrid of IAA and SLIM, the IAA-MAP method takes advantages of their merits while overcoming their limitations. Specifically, IAA-MAP provides more accurate estimates than SLIM, while maintaining a significantly lower sidelobe level than IAA. IAA-MAP provides the cleanest range-Doppler images among all methods considered herein.

3.3.2 Target Parameter Estimation Results

From the two peaks of each range-Doppler image given by IAA-MAP, we obtain four pairs of range measurements (in unit of kilometer), i.e.,$\{2.7825, 2.8200\}$, $\{2.7600, 2.8275\}$,

$\{2.8275, 2.9025\}$, and $\{2.8350, 2.8800\}$. For this multistatic active sonar system equipped with 2 transmitters and 2 receivers, there are 8 possible associations for the case of 2 targets. The brute-force approach needs to consider all possibilities, and obtains the correct association pattern at the cost of 1.23 seconds on an ordinary workstation (Intel Xeon E5506 processor 2.13G Hz, 12GB RAM, Windows 7 64-bit, and MATLAB R2010b). In comparison, the proposed GKC method only requires 0.56 seconds due to its efficient search. (The more targets are present in the field of view, the more computational saving the GKC method can provide. For example, when there are 3 targets, GKC requires 3.47 seconds while the brute-force method needs a much longer 26.01 seconds.) Finally, two groups of associated range measurements are obtained as: $\{2.7825, 2.7600, 2.9025, 2.8800\}$ and $\{2.8200, 2.8275, 2.8275, 2.8350\}$. Actually, the "Means" update step in the association procedure involves the estimation of the positions of the targets under the current association assignment. Therefore, the association pattern and the corresponding target position estimates are obtained simultaneously at the conclusion of the GKC iterations. Once the target position estimates are available, we can determine their velocity estimates as specified in Section 3.2.4. To evaluate the performance of the proposed EXIP-WLS algorithm, the root mean-squared error (RMSE) of the estimated target positions and velocities obtained via the EXIP-WLS and ULS methods (for both methods, the so-obtained target position estimates are utilized to facilitate the subsequent velocity estimation) from 100 Monte Carlo trials are listed in Table 3-3, from which we can see that the EXIP-based weighting scheme significantly improves the estimation accuracy.

Table 3-1. The noise power and the norm of the target reflection coefficients.

With respect to Rx1						
$\lvert\kappa_{1,1,1}\rvert$	$\lvert\kappa_{1,2,1}\rvert$	$\lvert\kappa_{2,1,1}\rvert$	$\lvert\kappa_{2,2,1}\rvert$	$\lvert\kappa_{1,1}\rvert$	$\lvert\kappa_{2,1}\rvert$	η_1
0.08	0.2	0.2	0.3	0.9	0.9	-10 dB
With respect to Rx2						
$\lvert\kappa_{1,1,2}\rvert$	$\lvert\kappa_{1,2,2}\rvert$	$\lvert\kappa_{2,1,2}\rvert$	$\lvert\kappa_{2,2,2}\rvert$	$\lvert\kappa_{1,2}\rvert$	$\lvert\kappa_{2,2}\rvert$	η_2
0.24	0.1	0.16	0.3	0.9	0.9	-10 dB

Table 3-2. System parameters.

c	underwater sound speed	1500 m/s or 2915.77 knots
P	length of the transmitted pings	400
W	bandwidth of the transmitted pings	200 Hz
L	number of Doppler bins	17
	carrier frequency	900 Hz
	sampling frequency at transmitter and receiver	8000 Hz
P/W	duration of the transmitted pings	2 s

Table 3-3. RMSE of Parameter Estimates Using ULS and EXIP-WLS.

	Target 1		Target 2	
Method	$\hat{\boldsymbol{\theta}}_1$(dB)	$\hat{\mathbf{v}}_1$(dB)	$\hat{\boldsymbol{\theta}}_2$(dB)	$\hat{\mathbf{v}}_2$(dB)
ULS	-9.8561	-19.7429	-5.7636	-15.6197
EXIP-WLS	-13.6826	-22.3587	-8.8532	-18.1237

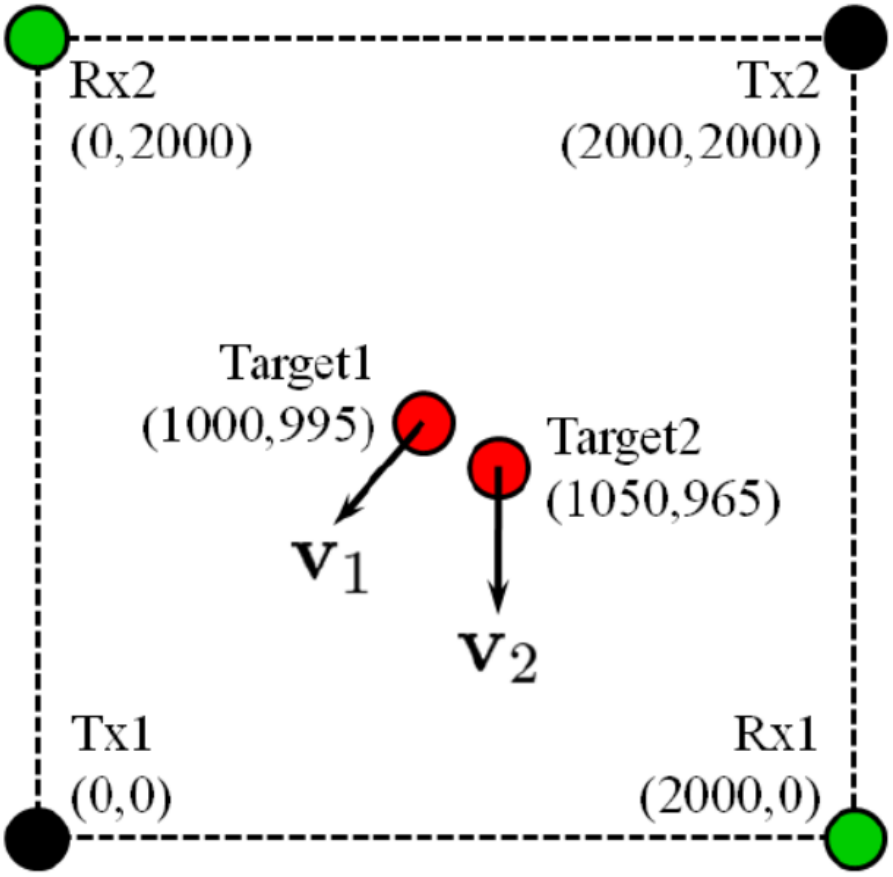

Figure 3-1. The simulation geometry.

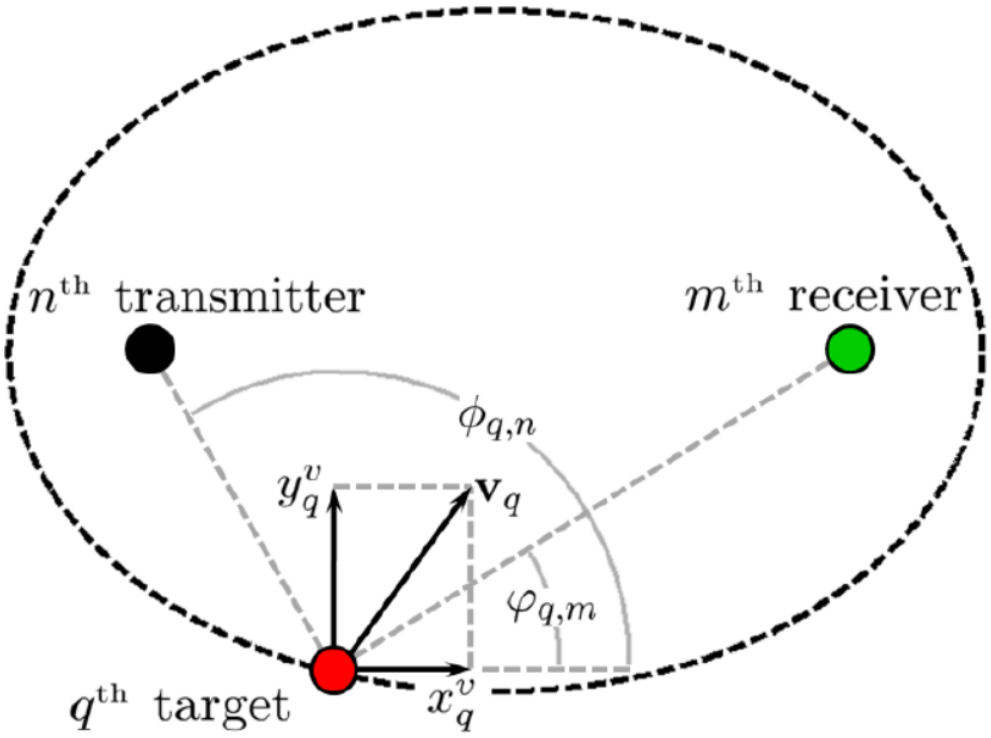

Figure 3-2. A generic active sonar scenario for the nth transmitter, the mth receiver, and the qth target.

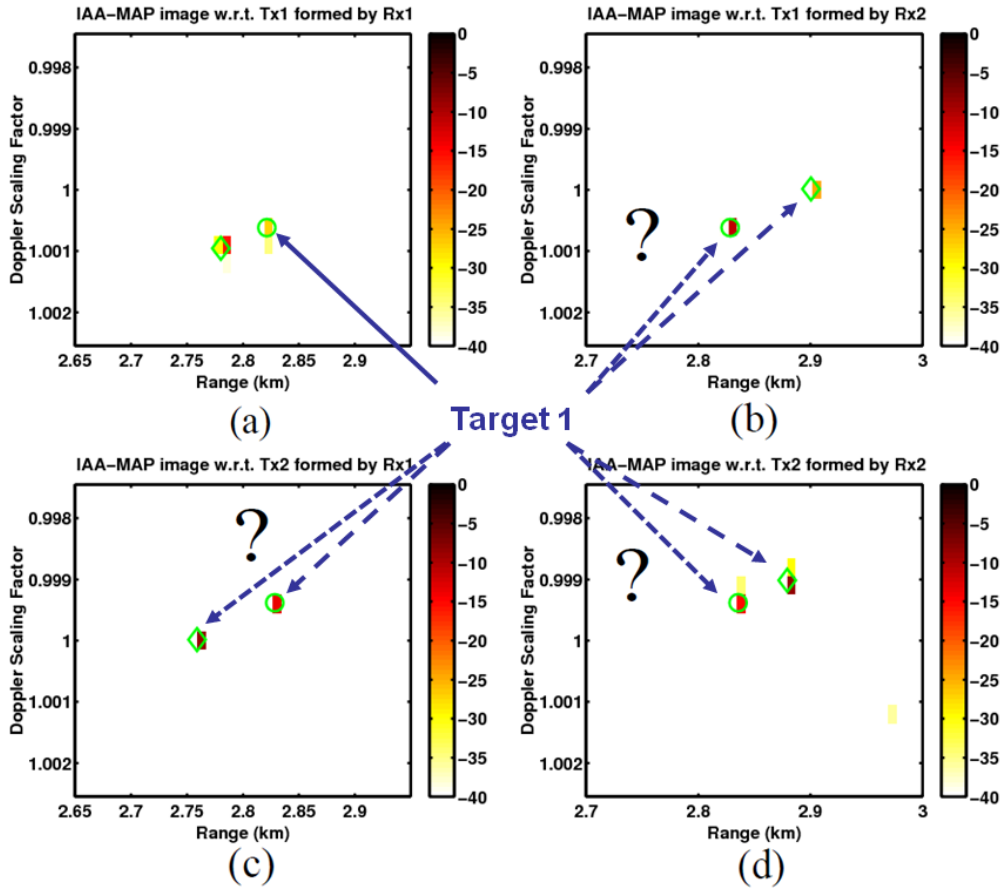

Figure 3-3. Description of the association problem.

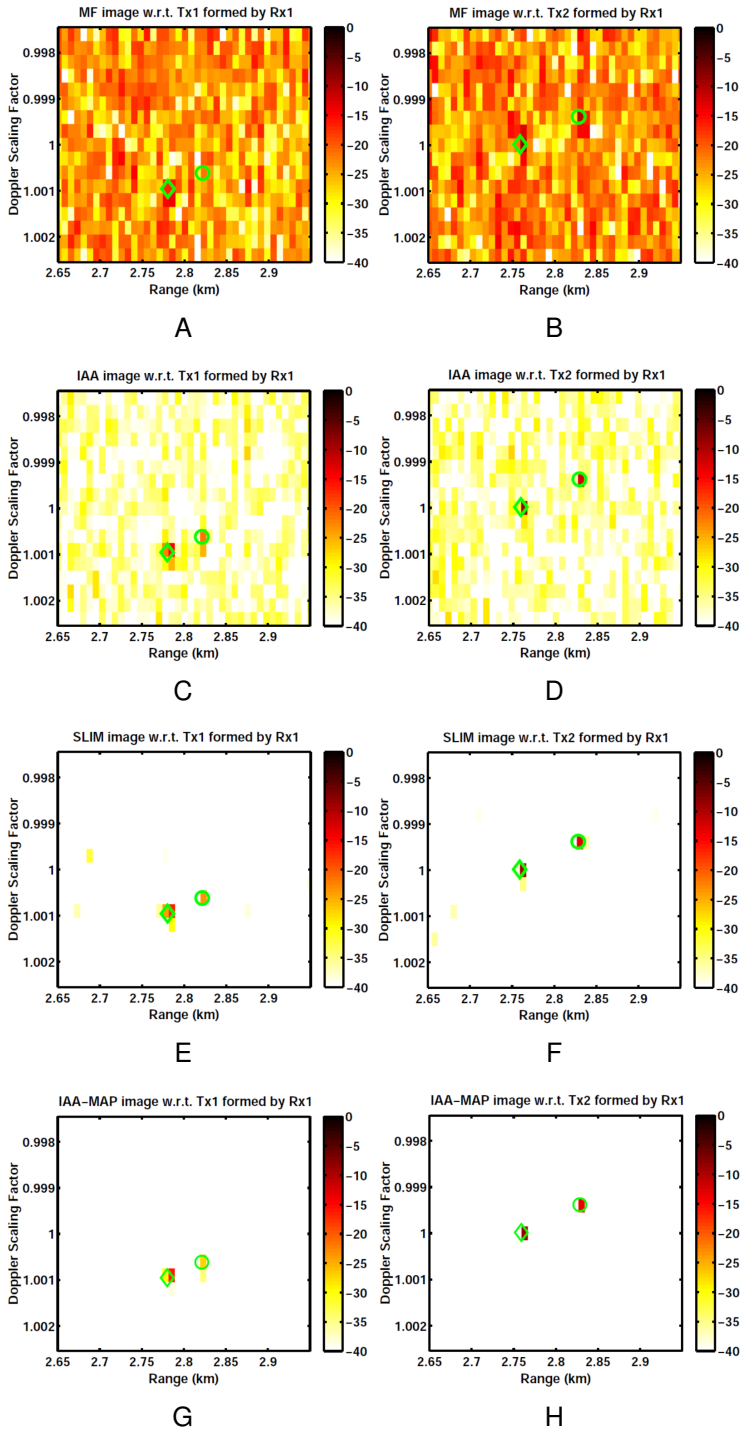

Figure 3-4. Range-Doppler images obtained at the first receiver produced by a multistatic active sonar system using various receiver filters. Circles and diamonds indicate the true locations of the first and second targets, respectively.

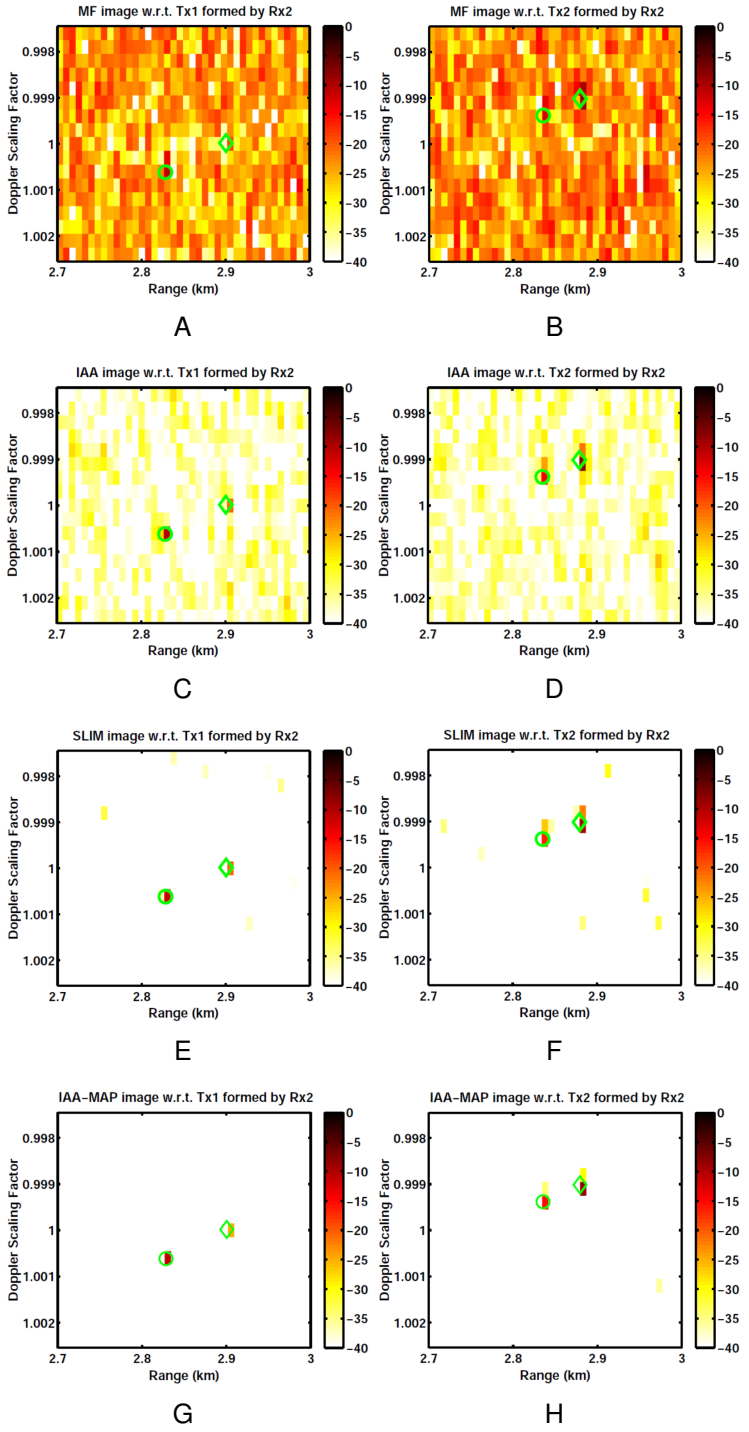

Figure 3-5. Range-Doppler images obtained at the second receiver produced by a multistatic active sonar system using various receiver filters. Circles and diamonds indicate the true locations of the first and second targets, respectively.

CHAPTER 4
WIDEBAND SOURCE LOCALIZATION USING SLIM

Source localization using a sensor array plays an important role in a large variety of signal processing applications involving electromagnetic, acoustic, and seismic sensing. For example as remarked in Chapter 3, the target association problem becomes an easy problem or even disappears entirely provided that the source localization technique can accurately estimate the angle of the targets for a multistatic active sonar system of which each receiver is equipped with a large array. Many advanced source localization techniques, such as MUSIC, Capon, and ESPRIT (see [27, 56, 57] and references therein), have been developed in the past decades. However, most algorithms in the literature were developed under the narrowband assumption, under which the time-difference of arrival (TDOA) of a signal at various sensors is negligible. In other words, it is assumed that a signal arrives at various sensors simultaneously with different phase shifts. However, in many practical applications, such as aeroacoustic array processing [58–61] and sonar [62, 63], this assumption is not valid, and the challenging wideband array processing problem arises.

Several adaptive wideband source localization approaches, including the spatial time frequency distribution based method (e.g., [64]) and the focussing-matrix based coherent signal-subspace (CSS) method (e.g., [65]), have been developed in the literature. However, the former is proposed for angle estimation in the particular case of chirp sources, while for the latter the requirement of preliminary angle estimates and the need for the design of a focusing matrix for each frequency bin are rather complicated tasks.

On the other hand, the sparse signal recovery (SSR) techniques have attracted much interest among researchers recently (e.g., [66–68]). Sparse algorithms, such as ℓ_1 norm minimization (e.g., [67, 69]) and FOCal Underdetermined System Solution (FOCUSS) [68], have been applied to the narrowband source localization problem,

resulting in better localization performance and enhanced capability of resolving closely-spaced sources [68–71]. Among the numerous adaptive SSR algorithms, the recently developed user-parameter free Sparse Learning via Iterative Minimization (SLIM) algorithm [13, 47] has shown satisfactory performances in various applications, such as nonparametric spectral estimation, radar imaging, and channel estimation for underwater acoustic communications [13]. The SLIM algorithm can work with even a single snapshot, arbitrary array geometry, coherent or non-coherent sources, and offers high resolution spatial estimation results at a relatively low computational complexity [13, 72].

To reap the SSR benefits, several SSR-based wideband source localization methods have been developed. In [73], the authors formulate the wideband source localization problem as a joint/group sparsity problem, and then propose a modified CoSaMP [74] method to solve the joint sparse signal recovery problem. However, it is known that CoSaMP and its orthogonal matching pursuit (OMP) variations fail to provide satisfactory performance in the source localization and spectral estimation applications, especially in the presence of closely spaced sources (see, e.g., [75]). A method, named wideband covariance matrix sparse representation (W-CMSR), is proposed in [76], by using the covariance matrix fitting technique. This method requires a priori information on the source correlation functions, which is not available in many practical applications, such as aeroacoustic and passive sonar.

The group LASSO (gLASSO) algorithm [77] can also be applied to the wideband source localization problem. As the conventional LASSO algorithm, gLASSO contains a user parameter balancing the fitting error and the sparsity promoting term. Selecting this user parameter is a difficult task. Furthermore, in [77] the shooting algorithm [78] is utilized to solve the gLASSO optimization problem, which essentially minimizes the cost function with respect to various groups of coefficients cyclically. As we will show via numerical examples, this algorithm suffers from a slow convergence problem, and

fails to provide satisfactory results. We further remark that many theoretical analyses of gLASSO have been performed in the literature [79–82] to investigate its uniqueness and recovery conditions. However, most of their conditions are not satisfied in the source localization applications, where steering vectors could be highly correlated to each other depending on the selected angle searching granularity. To our best knowledge, it is still an open problem to theoretically analyze the behavior and performance of gLASSO, as well as many other SSR algorithms, when the base vectors are sampled from a continuous manifold function.

In this chapter, we present two extensions of the SLIM algorithm in [13, 47] to wideband source localization, referred to as WB-SLIM-0 and WB-SLIM-1. Both algorithms exploit the joint/group sparse structure. We consider wideband sources which emit wideband signals occupying all frequencies of interest. Hence, once we find a signal at a certain angle and a specific frequency, we can expect signals at the same angle and other frequencies. To exploit the joint spatial sparse structure, we utilize a hierarchical Bayesian model and assume the same statistical distribution of spatial pseudo spectra for various frequencies. The cyclic minimization (CM) approach [53] is then used to solve the Maximum-a-Posteriori (MAP) problem. As we will discuss in Section 4.2.3, the WB-SLIM-1 algorithm can be also formulated in a similar form as gLASSO. However, unlike the existing gLASSO algorithm, WB-SLIM-1 is user parameter free and hence doesn't require fine tuning of user-parameter(s). Moreover, the proposed algorithm can converge much faster than the existing gLASSO algorithms[77].

We demonstrate the effectiveness of the proposed WB-SLIM algorithms for acoustic source localization using both the acoustic vector sensor arrays (VSA) [83–85] and the conventional scalar sensor arrays (SSA). Acoustic vector sensors measure scalar pressure along with particle motion, and have attracted much attention from researchers and practitioners alike. This technology features many advantages over the omnidirectional hydrophone sensor, including resolving of spatial left-right ambiguity and

the ability to "undersample" an acoustic wave without spatial aliasing. However, we have noticed that due to the wide beam of a single vector sensor, the ambiguity lobe cannot be eliminated effectively using the conventional data-independent delay-and-sum (DAS) approach, especially when the steering angle is near endfire. This fact implies that DAS cannot detect and localize targets near endfire uniquely, even with a vector sensor array. In this chapter, we will demonstrate that the proposed WB-SLIM algorithms, along with VSA, can effectively resolve the left-right ambiguity problem.

4.1 Data Model

Consider K far-field wideband source signals arriving at a sensor array from directions $\{\theta_k\}_{k=1}^{K}$. Let L be the number of samples of the received signal. At the pre-processing stage, an L-point discrete Fourier transform (DFT) is applied to the time-domain data received at each sensor to convert the wideband signal into L narrowband frequency signals. Then, the array output vector $\{\mathbf{y}_l\}$ in the presence of additive noise can be represented as (see, e.g., [65, 73]):

$$\mathbf{y}_l = \sum_{k=1}^{K} \mathbf{a}_l(\theta_k) x_{k,l} + \mathbf{n}_l, \text{ for } l = 1,\ 2,\ \cdots,\ L \tag{4–1}$$

where $\mathbf{a}_l(\theta_k)$ is the $M \times 1$ steering vector for the signal arriving from θ_k at the lth frequency bin, with f_l as the center frequency, and M is the number of sensors. Specifically, for a uniform linear array (ULA) formed by scalar sensors with inter-element spacing δ, the steering vector can be written as:

$$\mathbf{a}_l(\theta_k) = \left[1 \quad e^{-j2\pi \frac{f_l \delta \cos(\theta_k)}{c}} \quad e^{-j4\pi \frac{f_l \delta \cos(\theta_k)}{c}} \quad \cdots \quad e^{-j2(M-1)\pi \frac{f_l \delta \cos(\theta_k)}{c}}\right]^T, \tag{4–2}$$

where c denotes the propagation speed, and θ_k is defined relative to the endfire. For a vector sensor array (e.g., [83–85]), $\mathbf{a}_l(\theta_k)$ can be written as:

$$\mathbf{a}_l(\theta_k) = \mathbf{a}_{l,\text{array}}(\theta_k) \otimes \mathbf{a}_{\text{vs}}, \tag{4–3}$$

where $\mathbf{a}_{l,\text{array}}$ is the array steering vector for a scalar sensor array with an equivalent spatial configuration and plane wave input, $\mathbf{a}_{\text{vs}}$ denotes the response of a single vector sensor (see [85]), and $\otimes$ denotes the matrix Kronecker product. In (4–1), $x_{k,l}$ denotes the complex-valued amplitude of the signal arriving from θ_k at the lth frequency bin, and $\mathbf{n}_l$ denotes the noise and interference.

In practice, the number of wideband sources K is usually unknown. We use a fine angle grid, denoted by $\{\theta_n\}_{n=1}^{N}$, covering the set of locations of sources. Each point of this grid is considered to be a potential source location. Via estimating the signal power arriving at each potential angle, we obtain spatial pseudo spectra for various frequency bins, from which the sources can be detected and localized. Therefore, the following SSR problem arises:

$$\mathbf{y}_l = \mathbf{a}_l \mathbf{x}_l + \mathbf{n}_l, \quad l = 1, \ldots, L, \tag{4–4}$$

where $\mathbf{a}_l = \left[\mathbf{a}_l(\theta_1), \ldots, \mathbf{a}_l(\theta_N)\right] \in \mathbb{C}^{M \times N}$ with $\mathbf{a}_l(\theta_n)$ denoting the steering vector for the nth point of the scanning grid at the lth frequency bin, $\mathbf{x}_l = \left[x_{1,l}, \; x_{2,l}, \; \ldots, \; x_{N,l}\right]^T \in \mathbb{C}^{N \times 1}$ denotes the pseudo spatial spectrum at the grid points and the lth frequency bin. Note that usually $N \gg K$. Hence, the columns of $\mathbf{a}_l$ form an overcomplete basis for the signal $\mathbf{y}_l$. Generally, $\mathbf{x}_l$ cannot be determined uniquely from (4–4). However, in real applications, the number of sources is relatively small. This leads to a sparse property of $\mathbf{x}_l$ that can be exploited to identify $\mathbf{x}_l$ uniquely.

Note that the data model in (4–4) is different from the multi-snapshot model in [70, 86], where the steering matrices are the same for all snapshots, i.e., $\mathbf{a}_1 = \mathbf{a}_2 = \cdots = \mathbf{a}_L$. Note also that (4–4) can be re-written in the form of the standard SSR data model $\mathbf{y} = \mathbf{a}\mathbf{x} + \mathbf{n}$ by stacking the column vectors $\{\mathbf{y}_l\}$ on top of each other and with the steering matrix $\mathbf{a}$ being a block-diagonal matrix formed by $\{\mathbf{a}_l\}$. The group/block SSR techniques [87, 88] can then be applied. However, most of the existing group/block SSR algorithms,

such as gLASSO [77], are formulated using the regularization technique, which requires fine tuning of user-parameter(s).

4.2 The Wideband SLIM Algorithms

Inspired by the SLIM algorithm in [13, 47], we present in this section two algorithms, referred to as WB-SLIM-0 and WB-SLIM-1.

4.2.1 WB-SLIM-0

To exploit the aforementioned sparsity structure, we utilize the hierarchical Bayesian model [89]. First, we assume that the noise vectors $\{\mathbf{n}_l\}$ are independently identically distributed (i.i.d.) circularly symmetric complex Gaussian random vectors with zero mean and covariance matrix $\eta\mathbf{I}$ with η being an unknown deterministic parameter. We further assume $\{\mathbf{x}_l\}$ to be i.i.d. circularly symmetric complex Gaussian random vectors with zero mean and a diagonal covariance matrix $\mathbf{P} \triangleq \text{diag}\{p_1, p_2, \ldots, p_N\}$. In this subsection, $\{p_n\}$ are assumed to be deterministic unknowns. Note that the joint sparsity structure of $\{\mathbf{x}_l\}$ across frequency bins is imposed via assuming the same covariance matrix $\mathbf{P}$ for all $\{\mathbf{x}_l\}$.

From the above assumptions, we have the following probability density functions (pdf):

$$f(\{\mathbf{y}_l\}|\{\mathbf{x}_l\}, \eta) = \prod_{l=1}^{L} f(\mathbf{y}_l|\mathbf{x}_l, \eta) = \prod_{l=1}^{L} \frac{1}{(\pi\eta)^M} e^{-\frac{1}{\eta}\|\mathbf{y}_l - \mathbf{A}_l\mathbf{x}_l\|^2}, \tag{4–5}$$

and

$$f(\{\mathbf{x}_l\}|\{p_n\}) = \prod_{l=1}^{L} \frac{1}{\pi^N \prod_{n=1}^{N} p_n} e^{-\mathbf{x}_l^H \mathbf{P}^{-1} \mathbf{x}_l}. \tag{4–6}$$

The WB-SLIM-0 estimates of $\{\mathbf{x}_l\}$, $\{p_n\}$ and η are obtained by solving the following maximum a-posteriori (MAP) problem:

$$\min_{\{\mathbf{x}_l\}\{p_n\},\eta} g_{\text{WB-SLIM-0}}\left(\{\mathbf{x}_l\}\{p_n\}, \eta\right), \tag{4–7}$$

where

$$g_{\text{WB-SLIM-0}} \triangleq -\log\left[f(\{\mathbf{y}_l\}|\{\mathbf{x}_l\},\eta)\, f(\{\mathbf{x}_l\}|\{p_n\})\right]. \tag{4–8}$$

From (4–5), (4–6) and after discarding irrelevant constants, $g_{\text{WB-SLIM-0}}$ can be expressed as:

$$g_{\text{WB-SLIM-0}} = LM\log\eta + \frac{1}{\eta}\sum_{l=1}^{L} \parallel \mathbf{y}_l - \mathbf{a}_l\mathbf{x}_l \parallel^2 + L\sum_{n=1}^{N}\log p_n + \sum_{l=1}^{L}\sum_{n=1}^{N}\frac{|x_{n,l}|^2}{p_n}. \tag{4–9}$$

Note that when $p_n \to 0$ or $\eta \to 0$, the cost function in (4–9) can approach $-\infty$ for certain values of $\{\mathbf{x}_l\}$. In other words, this cost function does not have a global minimum over the unconstrained parameter set. To address this problem, we constrain $p_n \geq \epsilon$ and $\eta \geq \epsilon$, with ϵ being a small positive number ($\epsilon = 10^{-16}$ in our numerical examples). We remark that under the constraint that $p_n \geq \epsilon$, minimizing (4–9) will not lead to a strictly sparse solution, i.e., p_n, as well as elements of $\mathbf{x}_l$, will not be exactly zeros. However, as we will show via numerical examples, the so-obtained solution can be considered sparse practically, in the sense that most of the obtained $\{p_n\}$ are much smaller than the rest and hence the sources can be easily separated from noise.

The optimization problem of (4–7) can be solved by using the cyclic minimization (CM) technique [53]. First, given $\{\mathbf{x}_l\}_{l=1}^{L}$ and η, the minimization problem can be decoupled and simplified as follows:

$$\min_{p_n} \quad g_n(p_n) \triangleq L\log p_n + \frac{\sum_{l=1}^{L}|x_{n,l}|^2}{p_n},\ \text{s.t. } p_n \geq \epsilon, \tag{4–10}$$

for $n = 1,\ 2,\ \ldots,\ N$. Differentiating $g_n(p_n)$ with respect to (w.r.t.) p_n yields:

$$\frac{\partial g_n(p_n)}{\partial p_n} = \frac{L}{p_n} - \frac{1}{p_n^2}\sum_{l=1}^{L}|x_{n,l}|^2. \tag{4–11}$$

We can easily verify that $\frac{\partial g_n(p_n)}{\partial p_n} = 0$ when $p_n = \frac{1}{L}\sum_{l=1}^{L}|x_{n,l}|^2$. Furthermore, the cost function $g_n(p_n)$ is monotonically decreasing when $0 < p_n \leq \frac{1}{L}\sum_{l=1}^{L}|x_{n,l}|^2$, and monotonically increasing when $p_n \geq \frac{1}{L}\sum_{l=1}^{L}|x_{n,l}|^2$. Therefore, the optimal solution of

(4–10) is:

$$p_n = \max\left\{\frac{1}{L}\sum_{l=1}^{L}|x_{n,l}|^2, \epsilon\right\}, \quad n = 1, \ldots, N. \tag{4–12}$$

Similarly, given $\{\mathbf{x}_l\}_{l=1}^{L}$ and $\{p_n\}$, the optimization problem reduces to

$$\min_{\eta} \quad g(\eta) \triangleq LM\log\eta + \frac{1}{\eta}\sum_{l=1}^{L} \| \mathbf{y}_l - \mathbf{a}_l\mathbf{x}_l \|^2, \text{ s.t. } \eta \geq \epsilon, \tag{4–13}$$

whose solution can be obtained easily as follows:

$$\eta = \max\left\{\frac{1}{LM}\sum_{l=1}^{L} \| \mathbf{y}_l - \mathbf{a}_l\mathbf{x}_l \|^2, \epsilon\right\}. \tag{4–14}$$

Finally, for given η and p_n, differentiating $g_{\text{WB-SLIM-0}}$ w.r.t. $\mathbf{x}_l$ and setting the derivative to zero yield:

$$\begin{aligned}\mathbf{x}_l &= \left[\mathbf{a}_l^H\mathbf{a}_l + \eta\mathbf{P}^{-1}\right]^{-1}\mathbf{a}_l^H\mathbf{y}_l \\ &= \mathbf{P}\mathbf{a}_l^H\left[\mathbf{a}_l\mathbf{P}\mathbf{a}_l^H + \eta\mathbf{I}\right]^{-1}\mathbf{y}_l, \quad l = 1, \ldots, L.\end{aligned} \tag{4–15}$$

The solution of (4–7) can be obtained via iterating (4–12), (4–14), and (4–15).

4.2.2 WB-SLIM-1

As we will show by numerical examples, WB-SLIM-0 provides a sparse solution. However, the downside of this is that it may fail to detect weak targets, especially at low SNR. In this subsection, we propose a variation of WB-SLIM-0, called WB-SLIM-1, which provides a less sparse but more robust solution.

In addition to the Gaussian distribution assumptions on $\{\mathbf{n}_l\}$ and $\{\mathbf{x}_l\}$ introduced in Section 4.2.1, we further assume that $\{p_n\}_{n=1}^{N}$ are i.i.d. Gamma$(L+1, \frac{1}{L})$ distributed that is

$$f(p_n) \propto p_n^L e^{-Lp_n}, \quad n = 1, \ldots, N. \tag{4–16}$$

Similarly to WB-SLIM-0, after taking the negative logarithm of the joint pdf, we obtain the cost function:

$$g_{\text{WB-SLIM-1}} = LM\log\eta + \frac{1}{\eta}\sum_{l=1}^{L} \| \mathbf{y}_l - \mathbf{a}_l\mathbf{x}_l \|^2 + L\sum_{n=1}^{N} p_n + \sum_{l=1}^{L}\sum_{n=1}^{N} \frac{|x_{n,l}|^2}{p_n}. \tag{4–17}$$

We apply a similar cyclic optimization procedure to (4–17), as detailed below. For fixed $\{\mathbf{x}_l\}$ and η, the optimization problem reduces to:

$$\min_{p_n} \quad Lp_n + \sum_{l=1}^{L} \frac{|x_{n,l}|^2}{p_n} \text{ s.t. } p_n \geq \epsilon. \tag{4–18}$$

By using the same technique as for (4–12), we can easily get the optimal solution for (4–18) as follows:

$$p_n = \max\left\{ \sqrt{\frac{1}{L}\sum_{l=1}^{L} |x_{n,l}|^2}, \epsilon \right\}, \quad \text{for } n = 1, \ldots, N. \tag{4–19}$$

The updating of $\mathbf{x}_l$ and η is exactly the same as for WB-SLIM-0 (see (4–15) and (4–14)).

4.2.3 Discussion

The WB-SLIM-0 and WB-SLIM-1 algorithms are summarized in Table 4-1. Both algorithms are initialized using the conventional delay-and-sum (DAS) estimates.

As shown in Table 4-1, the difference between WB-SLIM-0 and WB-SLIM-1 lies in the $\{p_n\}$ updates, due to the different *priors* assumed for $\{p_n\}$. We remark on the fact that under the constraints $\eta \geq \epsilon$ and $p_n \geq \epsilon$ for $n = 1, \ldots, N$, the cost functions of WB-SLIM-0 and WB-SLIM-1 in (4–9) and (4–17) are bounded from below. By a cyclic minimization (CM) property, the cost functions are monotonically non-increasing at each iteration. This implies that both WB-SLIM-1 and WB-SLIM-0 are convergent in terms of cost function. Our empirical experience suggests that the proposed WB-SLIM algorithms do not provide significant performance improvements after about 20 iterations. We further remark that the cost function in (4–9) is not convex. Hence, convergence to the global optimum is not guaranteed for any algorithm, including those

proposed ones. However, as we will demonstrate numerically, a good estimation result can be achieved via choosing the initialization appropriately.

Note also that ignoring the constraint $p_n \geq \epsilon$ and minimizing the cost functions (4–9) and (4–17) with respect to $\{\mathbf{P}_n\}$, the concentrated cost functions can be written (to within an additive constant), respectively, as follows:

$$g_{\text{WB-SLIM-0}} = LM\log\eta + \frac{1}{\eta}\sum_{l=1}^{L} \| \mathbf{y}_l - \mathbf{a}_l\mathbf{x}_l \|^2 + \sum_{n=1}^{N} \log\left[\sum_{l=1}^{L} |x_{n,l}|^2\right], \tag{4–20}$$

and

$$g_{\text{WB-SLIM-1}} = LM\log\eta + \frac{1}{\eta}\sum_{l=1}^{L} \| \mathbf{y}_l - \mathbf{a}_l\mathbf{x}_l \|^2 + 2\sqrt{L}\sum_{n=1}^{N}\left[\sum_{l=1}^{L} |x_{n,l}|^2\right]^{\frac{1}{2}}. \tag{4–21}$$

Therefore, the WB-SLIM-0 and WB-SLIM-1 algorithms can be reformulated as the minimization of (4–20) and (4–21), respectively, which are extensions of the SLIM-q formulation (with $q = 0$ or 1) in [47]. The original cost functions (4–9) and (4–17) can be interpreted as augmented functions of (4–20) and (4–21), which introduce additional optimization variables (i.e.,$\{p_n\}$) to facilitate the CM technique. This augmentation optimization technique can also be used to solve the gLASSO optimization problem, which yields an algorithm similar to WB-SLIM-1 (Table 4-1) but with fixed η. In our experience, this new gLASSO algorithm can converge much faster than the existing one in the literature [77], where the shooting algorithm is used.

4.3 RELAX

The parametric RELAX [20, 90] algorithm is adopted here to obtain the refined angle and power estimates. The WB-SLIM algorithms produce sparse spatial angle estimates and are able to resolve closely-spaced sources. Hence the number of sources can be reliably determined by a simple thresholding procedure or by order selection algorithms such as the Bayesian information criterion (BIC) [52]. The RELAX algorithm requires information on the number of sources but does not depend on the scanning grid

that covers the region of possible source locations, and hence it can be used to refine the WB-SLIM estimates.

The RELAX algorithm can be formulated as a joint nonlinear least-square problem:

$$\min_{\{\theta_k, x_{k,l}\}} \sum_{l=1}^{L} \| \mathbf{y}_l - \sum_{k=1}^{\hat{K}} \mathbf{a}_l(\theta_k) x_{k,l} \|^2, \tag{4–22}$$

where $\hat{K}$ is the estimated number of sources. Initialized with the WB-SLIM results, RELAX solves the optimization problem (4–22) cyclically. To update the estimates of the kth source, we define:

$$\tilde{\mathbf{y}}_{k,l} = \mathbf{y}_l - \sum_{i \neq k} \mathbf{a}_l(\hat{\theta}_i) \hat{x}_{i,l}, \tag{4–23}$$

where $\{\hat{\theta}_i, \hat{x}_{i,l}\}_{i \neq k}$ are the most recent estimates of the other sources. Then, the optimization problem is reduced to:

$$\min_{\{\theta_k, x_{k,l}\}} \sum_{l=1}^{L} \| \tilde{\mathbf{y}}_{k,l} - \mathbf{a}_l(\theta_k) x_{k,l} \|^2 . \tag{4–24}$$

Solving this optimization problem yields the DAS-type estimates:

$$\hat{\theta}_k = \arg\max_{\theta_k} \sum_{l=1}^{L} |\mathbf{a}_l^H(\hat{\theta}_k) \tilde{\mathbf{y}}_{k,l}|^2, \tag{4–25}$$

and

$$\hat{x}_{k,l} = \frac{\mathbf{a}_l^H(\hat{\theta}_k) \tilde{\mathbf{y}}_{k,l}}{\|\mathbf{a}_l(\hat{\theta}_k)\|^2} \text{ for } l = 1, 2, \ldots, L. \tag{4–26}$$

The RELAX algorithm updates $\{\hat{\theta}_k, \hat{x}_{k,l}\}$ for all sources iteratively using (4–25) and (4–26). We terminate the iteration when the norm of the difference between two consecutive estimates falls below a predefined small threshold (10^{-4} in our numerical examples). The RELAX approach is summarized in Table 4-2.

Owing to the CM approach employed, the RELAX algorithm is locally convergent. Note that RELAX requires only 1D maximizations around the WB-SLIM estimates. This maximization operation can be efficiently implemented using derivative-free uphill search

methods such as the Nelder-Mead algorithm [91], which is incorporated in the MATLAB optimization toolbox as the function “fminsearch”.

4.4 Numerical Examples

In this section, we present several numerical examples to demonstrate the excellent angle estimation performance of the proposed methods. We consider two closely-spaced wideband sources located near the array endfire at 10.11° and 11.02°. We assume that the signals emitted by the two sources are statistically independent with flat power spectra ranging from -10 KHz to 10 KHz. A 128-point FFT is performed at the preprocessing stage to decompose the entire frequency band into $L = 128$ narrow frequency bins. The SNRs of the two sources are 25 dB and 20 dB, respectively, unless otherwise specified. We assume that the speed of sound (in the sea) is 1530 m/s.

We first consider a 20-element scalar-sensor ULA with the inter-element spacing equal to $\delta = 3$ meters. We apply the proposed WB-SLIM-0 and WB-SLIM-1 to the received signal. For comparison purposes, several conventional angle estimation algorithms, namely DAS, NB-SLIM-0 and NB-SLIM-1, are also considered. These methods apply the DAS or the narrowband SLIM algorithms of [13, 47] to each frequency bin, and then combine the obtained spatial pseudo spectra non-coherently. For all the algorithms in this section, the scanning grid is uniform with 0.25° increment between adjacent points. Throughout this chapter, the iteration number of group LASSO is set to 5000, and the iteration numbers of NB-SLIM and WB-SLIM are fixed to 50.

Figure 4-1 shows the spatial pseudo spectra, i.e., $\{p_n\}_{n=1}^N$, obtained by various algorithms. The dashed lines indicate the true angles. From Figures 4-1A-4-1F, we can see clearly that the scalar-sensor array suffers from the left-right ambiguity problem. Furthermore, we note that the data-independent DAS algorithm suffers from the low-resolution problem: it is unable to resolve the two closely-spaced targets. Figure 4-1B shows the spatial pseudo spectra obtained by gLASSO, which represents the best results we got via fine tuning of the gLASSO user-parameter. As we can

see, the gLASSO algorithm fails to detect the two sources correctly. Note that the shooting algorithm has been used to obtain Figure 4-1B. As we discussed above, the augmentation optimization technique can also be used to solve the gLASSO problem. This new gLASSO algorithm yields similar results as the WB-SLIM-1 in Figure 4-1E. The spatial pseudo spectra of NB-SLIM-1 and NB-SLIM-0 are shown in Figures 4-1C and 4-1D, respectively. These two narrow-band SLIM algorithms can (although only barely) resolve the two closely-spaced targets. However, both provide noisy spatial pseudo spectra, which may lead to high false detection rates. The reason for this is that both methods apply the narrowband SLIM algorithm to each frequency bin independently. When the frequency is larger than 510 Hz, the corresponding inter-element spacing is larger than half wavelength. The narrowband SLIM algorithm will then generate ambiguous lobes for frequency bins with frequency larger than 510 Hz. After the non-coherent combination of spatial pseudo spectra, these ambiguous lobes become high sidelobes. In contrast, as shown in Figures 4-1E and 4-1F, both WB-SLIM-0 and WB-SLIM-1 are able to effectively suppress these high sidelobes, provide clean and sparse spatial pseudo spectra, and neatly resolve the two closely-spaced sources. Note that WB-SLIM-0 performs better than WB-SLIM-1 in this example.

Figure 4-2 corresponds to a vector sensor array example. The simulation parameters are exactly the same as those used to obtain Figure 4-1, except that the scalar sensors are replaced by vector sensors. From Figures 4-2A and 4-2B, we can see that, once again, DAS and gLASSO cannot resolve the two closely-spaced sources. The ambiguous lobe around -10 degrees is about 0.3 dB lower than the mainlobe. This means that the vector sensor array in principle has the capability to resolve the left-right ambiguity problem. As we can see from Figures 4-2C and 4-2D, NB-SLIM-1 and NB-SLIM-0 suppress the ambiguous lobe even more to about 10 dB under main lobe. Figures 4-2E and 4-2F shows that the proposed WB-SLIM-0 and WB-SLIM-1 algorithms outperform their narrowband counterparts significantly. Both are able to provide clean

and sparse spatial pseudo spectra, resolve the two closely-spaced sources, and supress the ambiguous lobes. We consider a more challenging example in Figure 4-3, where the SNR of the second source is decreased to 0 dB, i.e. 25 dB lower than for the first one. The other simulation parameters are the same as those used in Figure 4-2. For a better illustration, we show the zoomed-in spatial pseudo spectra in the region $[0, 20]$ degrees. As we can see, only WB-SLIM-1 is able to identify the two sources correctly in this challenging case.

Figure 4-4 shows the performance improvement achieved by using the RELAX algorithm. The simulation parameters are the same as those used in Figure 4-1. We first utilize the WB-SLIM-1 or WB-SLIM-0 algorithm to detect the number of sources and obtain initial angle and amplitude estimates, which are then refined using RELAX. In Figures 4-4A and 4-4B, the red circles indicate the true angles and powers of the sources, and the black stars show the RELAX estimates. For comparison purposes, we also show the spatial pseudo spectra of DAS and WB-SLIM, whose peaks indicate the corresponding angle and power estimates. We display the angle and power estimates obtained in 20 Monte-Carlo runs. From Figures 4-4A and 4-4B, we see that RELAX effectively refines the angle and power estimates of WB-SLIM-1 or WB-SLIM-0, and obtains quite accurate estimates.

Finally, we demonstrate the performance of various algorithms in terms of the detection rate and the root-mean-squared-error (RMSE). For performance comparison purposes, we compute the wideband deterministic Cramer-Rao bound (CRB) for the angle estimates, which is given by [92], as follows:

$$\mathrm{CRB}(\theta) = \frac{\eta}{2}\left[\sum_{l=1}^{L} \mathrm{Re}\Big\{(\dot{\mathbf{a}}_l^H \Pi_{\mathbf{a}_l}^{\perp} \dot{\mathbf{a}}_l) \odot (\mathbf{x}_l \mathbf{x}_l^H)^T\Big\}\right]^{-1} \tag{4–27}$$

where

$$\dot{\mathbf{a}}_l \triangleq \left[\left.\frac{\mathrm{d}\mathbf{a}_l(\theta)}{\mathrm{d}\theta}\right|_{\theta=\theta_1}, \cdots, \left.\frac{\mathrm{d}\mathbf{a}_l(\theta)}{\mathrm{d}\theta}\right|_{\theta=\theta_K}\right], \tag{4–28}$$

and

$$\Pi_{\mathbf{a}_l}^{\perp} \triangleq \mathbf{I} - \mathbf{a}_l\left(\mathbf{a}_l^H\mathbf{a}_l\right)^{-1}\mathbf{a}_l^H. \tag{4–29}$$

We consider the same array and wideband sources for Figure 4-1. The x-axes of Figures 4-5A-4-5C show the SNR of the first source. The SNR the second source is 5 dB smaller than that of the first. We perform 100 Monte-Carlo simulations. A Monte-Carlo trial is deemed failed when one or more sources are not detected or either of the DOA estimates is more than 0.5 degrees away from the corresponding true value. The detection rate is defined as the ratio of the number of trials in which both sources are detected and localized correctly over the total trial number. From Figure 4-5A, we can see that both WB-SLIM-0 and WB-SLIM-1 achieve 100% detection rate when SNR is larger than or equal to 5 dB. However, at low SNR, WB-SLIM-1 outperforms WB-SLIM-0 significantly. Figures 4-5B and 4-5C show that RELAX, initialized by either WB-SLIM-1 or WB-SLIM-0, can achieve good estimation performance. Note that when SNR is less than 5 dB, the RMSE of the WB-SLIM-0 & RELAX estimates is not defined due to the detection failure. Hence, we only provide RMSE when SNR $\geq$ 5 dB for this algorithm. The RMSEs of the angle estimates are approximately equal to RCRB for the stronger source, and are about two times the RCRB for the weak one (note that the deterministic CRB is not necessarily achievable, see, e.g., [92]).

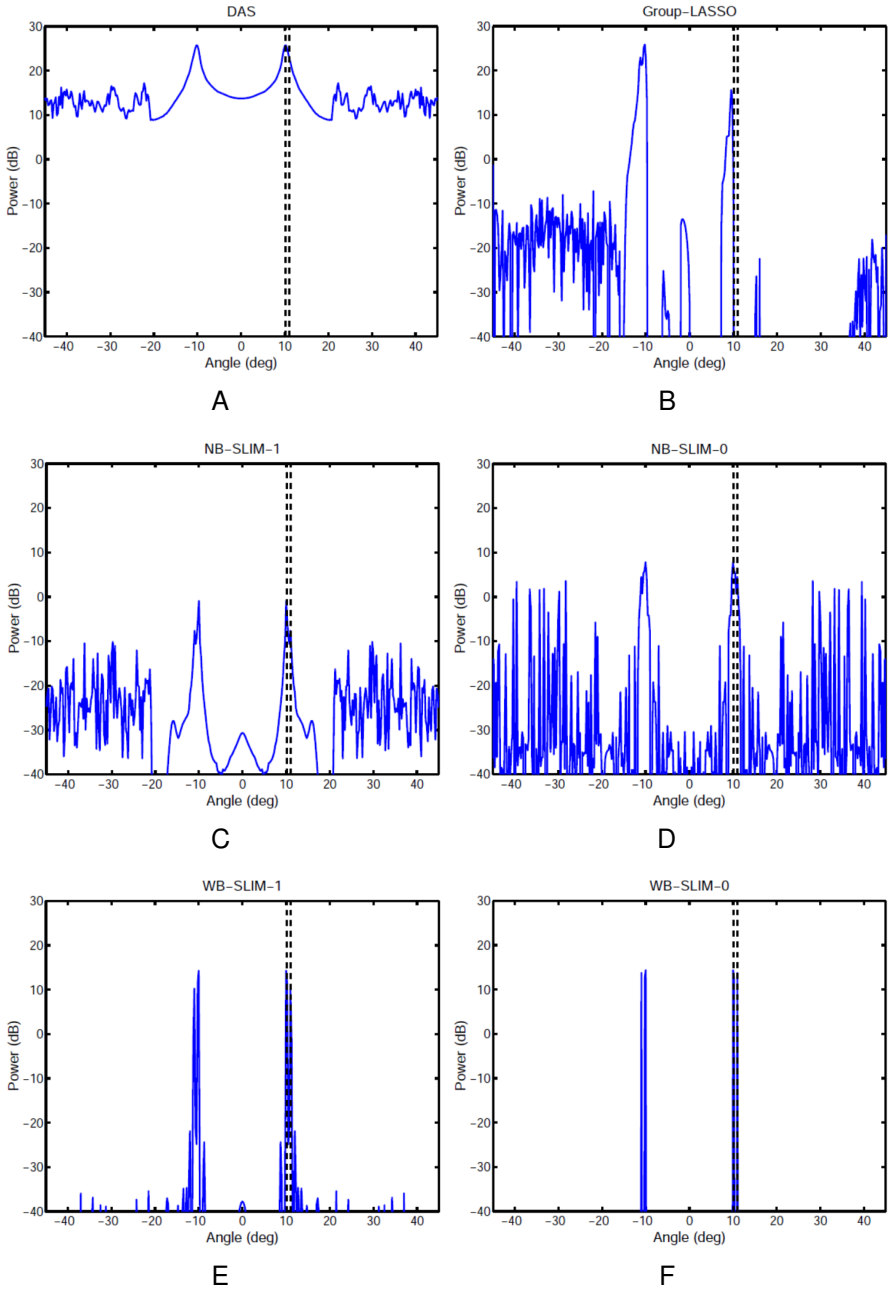

Figure 4-1. Spatial pseudo spectra obtained with a scalar sensor array and various algorithms: A) DAS, B) gLASSO, C) NB-SLIM-1, D) NB-SLIM-0, E) WB-SLIM-1, and F) WB-SLIM-0.

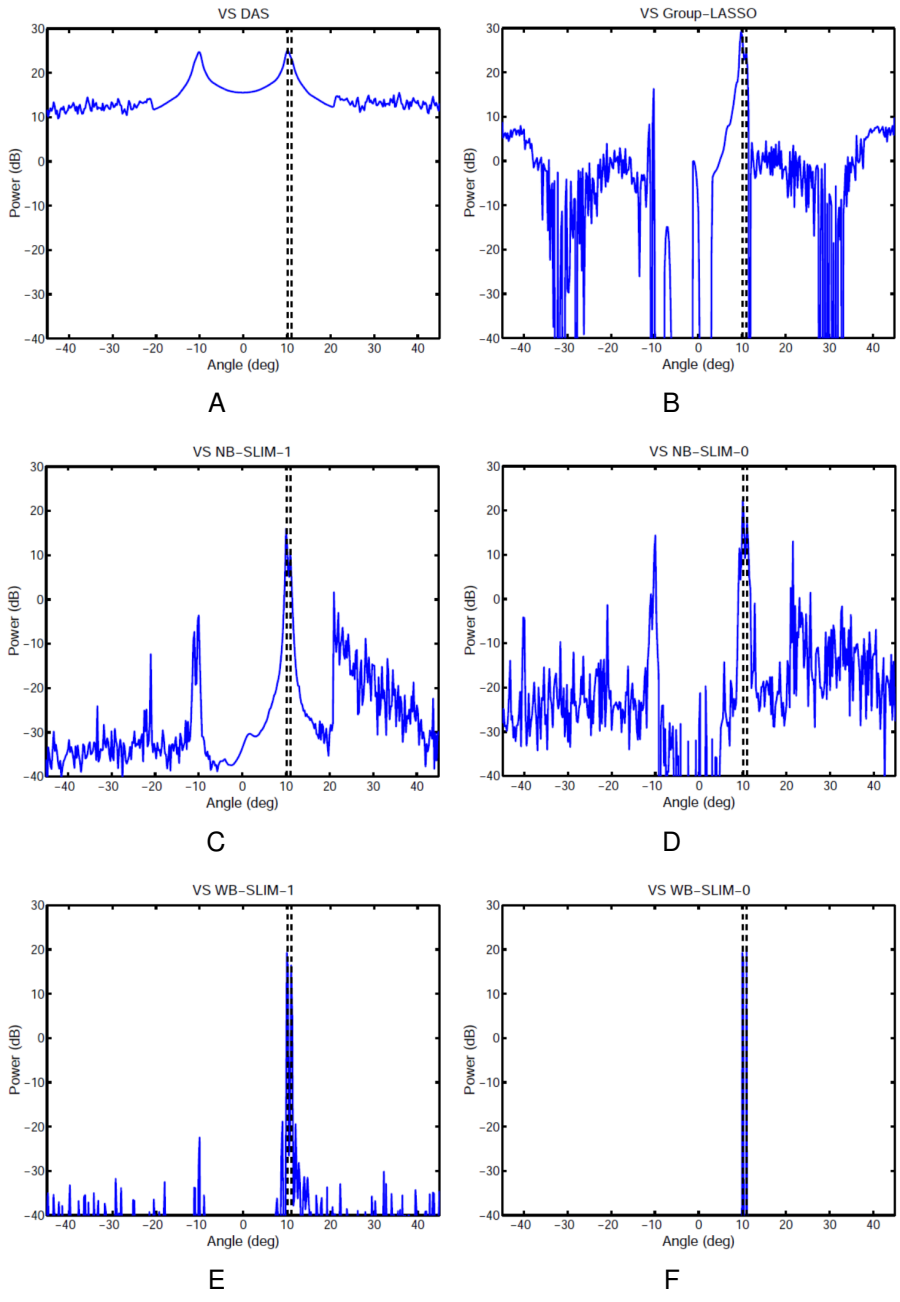

Figure 4-2. Spatial pseudo spectra obtained with a vector sensor array and various algorithms: A) DAS, B) gLASSO, C) NB-SLIM-1, D) NB-SLIM-0, E) WB-SLIM-1, and F) WB-SLIM-0.

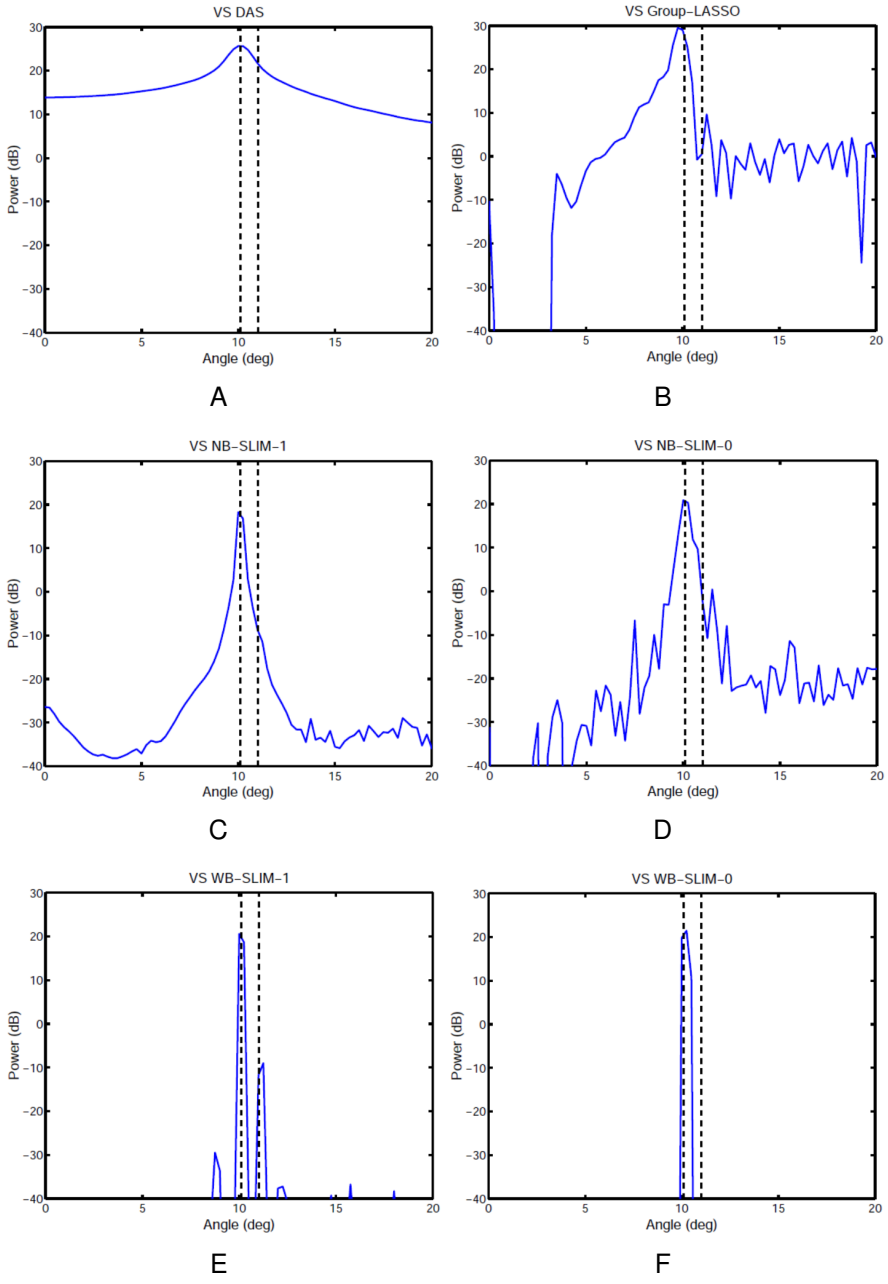

Figure 4-3. Spatial pseudo spectra, in the case of a weak source, obtained by various algorithms: A) DAS, B) gLASSO, C) NB-SLIM-1, D) NB-SLIM-0, E) WB-SLIM-1, and F) WB-SLIM-0.

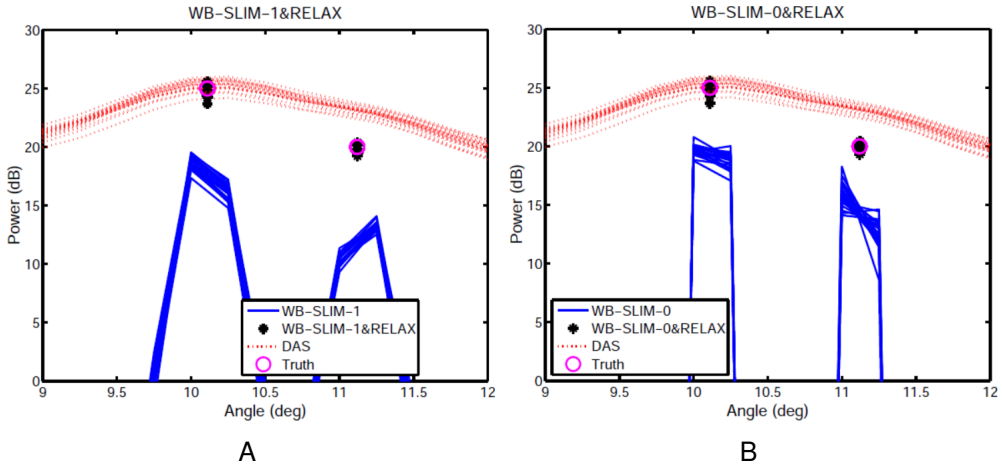

Figure 4-4. Performance enhancement using RELAX. A) WB-SLIM-1 and RELAX, B) WB-SLIM-0 and RELAX.

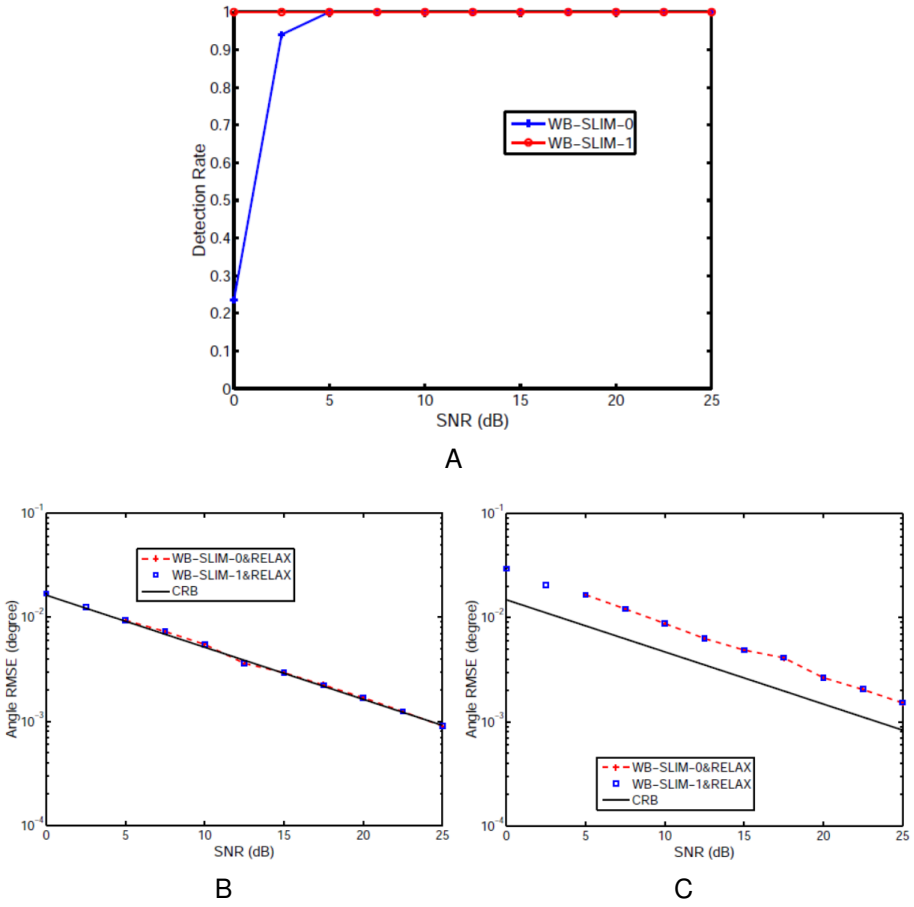

Figure 4-5. Empirical failure rate and RMSEs versus SNR. A) Detection rate, B) RMSE of Source 1, and C) RMSE of Source 2.

Table 4-1. WB-SLIM algorithms.

Initialize $\{\mathbf{x}_l\}_{l=1}^{L}$ and η with the DAS estimates as follows:

$$\begin{aligned}
\mathbf{x}_{n,l}^{(0)} &= \mathbf{a}_l^H(\theta_n)\mathbf{y}_l / \parallel \mathbf{a}_l(\theta_n) \parallel^2, \text{ for } n = 1, \dots, N;\ l = 1, \dots, L; \\
\eta^{(0)} &= \max\left\{ \frac{1}{10LM} \sum_{l=1}^{L} \parallel \mathbf{x}_l^{(0)} \parallel^2, \epsilon \right\}
\end{aligned}$$

Repeat the following steps for $t = 0,\ 1,\ 2,\ \cdots$:

$$\begin{aligned}
p_n^{(t+1)} &= \begin{cases} \max\left\{ \frac{1}{L} \sum_{l=1}^{L} |x_{n,l}^{(t)}|^2, \epsilon \right\} & \text{(WB-SLIM-0)} \\ \max\left\{ \sqrt{\frac{1}{L} \sum_{l=1}^{L} |x_{n,l}^{(t)}|^2}, \epsilon \right\} & \text{(WB-SLIM-1)} \end{cases}, \text{ for } n = 1, \dots, N; \\
\mathbf{x}_l^{(t+1)} &= \mathbf{P}^{(t+1)}\mathbf{a}_l^H(\mathbf{a}_l\mathbf{P}^{(t+1)}\mathbf{a}_l^H + \eta^{(t)}\mathbf{I})^{-1}\mathbf{y}_l, \quad l = 1, \dots, L; \\
\eta^{(t+1)} &= \max\left\{ \frac{1}{LM} \sum_{l=1}^{L} \parallel \mathbf{y}_l - \mathbf{a}_l\mathbf{x}_l^{(t+1)} \parallel^2, \epsilon \right\}.
\end{aligned}$$

until convergence

Table 4-2. The RELAX algorithm.

$\hat{K}$: Number of sources obtained from WB-SLIM
$\{\hat{\theta}_k\}_{k=1}^{\hat{K}}$: Locations of the sources obtained from WB-SLIM
$\{\hat{x}_{k,l}\}_{k=1,l=1}^{\hat{K},\ L}$: Corresponding waveforms obtained from WB-SLIM
repeat
  for $k = 1, \ldots, \hat{K}$
    $\tilde{\mathbf{y}}_{k,l} = \mathbf{y}_l - \sum_{i=1, i\neq k}^{\hat{K}} \mathbf{a}_l(\hat{\theta}_i)\hat{x}_{i,l} \quad l = 1, \ldots, L$
    $\hat{\theta}_k = \arg\max_{\theta_k} \sum_{l=1}^{L} |\mathbf{a}_l^H(\theta_k)\tilde{\mathbf{y}}_{k,l}|^2$
    $\hat{x}_{k,l} = \frac{\mathbf{a}_l^H(\hat{\theta}_k)\tilde{\mathbf{y}}_{k,l}}{\|\mathbf{a}_l(\hat{\theta}_k)\|^2}, \quad l = 1, \ldots, L$
  end for
until (convergence)

CHAPTER 5
CONCLUSIONS AND FUTURE WORK

Various signal processing techniques have been proposed and applied to the receiver design of the MIMO UAC system and the multistatic active sonar system, respectively. In Chapter 2, we are mainly involved in finding the proper model for the acoustic channels subject to both ISI and time scaling effects which are largely induced by the relative motions between the transmitter and receiver arrays. We find out that a preferable way is to parsimoniously model the channel by assuming a common Doppler scaling factor imposed on the propagation paths among all the transmitter and receiver pairs. Temporal resampling has been used to effectively convert the Doppler scaling effects to Doppler frequency shifts and a data-adaptive sparse channel estimation algorithm, referred to as GoSLIM-V, is used to estimate the underlying CIRs and Doppler frequency in a joint manner. For symbol detection, we have investigated the turbo equalization schemes implemented by the LMMSE-based soft-input soft-output equalizer as well as its low complexity approximation.The latter provides only slightly degraded detection performance but at a significantly lower computational complexity compared to the former and is thus preferred.

In Chapter 3, we have focused on two signal processing aspects of a multistatic active sonar system: Range-Doppler imaging and target parameter estimation.
For the former, we have presented the IAA-MAP method to enhance the resolution and suppress sidelobe levels simultaneously. For the latter, we have introduced a generalized K-Means clustering approach for target peak association and applied the extended invariance principle to determine the target position and velocity estimates via weighted least-squares fitting. Moreover, one possible way to mitigate the target association problem is to accurately estimate the angle of the targets by applying advanced source localization method to receivers each equipped with a large array. Since most existing techniques are developed under the narrowband assumption, we

are inspired to derive the WB-SLIM-0 and WB-SLIM-1 algorithms for wideband source localization, based on two different hierarchical Bayesian statistical models. These two algorithms provide high-resolution angle estimates without the need of tuning any user parameters. We have also proposed a wideband RELAX algorithm to refine the angle and power estimates obtained with the WB-SLIM-0 and WB-SLIM-1 beyond the accuracy allowed by the fineness of the grid used in the latter. Both numerical and experimental examples have been provided in Chapters 2, 3, and 4 to demonstrate the effectiveness and the excellent performance of the proposed UAC and active sonar system design.

Note that conventional sonar system as discussed in Chapter 3 is a pulsed active sonar (PAS) system, where a powerful pulse is sent out before a relatively long listing time [42, 43, 93]. The PAS system however has several disadvantages. Firstly, a target at long range requires long listening time because of the low underwater propagation speed of sound. Consequently, there is only a short period of time for detecting targets due to the short pulse duration. Secondly, the power output of the transmitters is high enough to induce environment pollution. For instance, such pollution cold possibly lead to the mass stranding of marine animals [94]. Thirdly, the Doppler resolution is inversely proportional to the pulse duration and is therefore relatively low. In comparison, multistatic continuous active sonar (CAS) systems offer some attractive advantages [95, 96]. Firstly, by exploiting the continuous transmission and the spatial diversity, multistatic CAS systems can provide significantly enhanced target detection and parameter estimation performance. Secondly, lower peak power level is achieved because of continuous transmission, which alleviates detrimental noise pollution. Thirdly, the Doppler resolution of the multistatic CAS system is much higher than the pulsed system. These advantages motivate us to investigate the implementation of the multistatic CAS system in the future.

We also want to design a waveform set which possesses satisfactory auto- and cross-correlation properties to improve the target detection performance and also satisfies spectrum containment restrictions required by the oceanic environment and the hardware system [97–100]. Also, good range-Doppler imaging performance is desired for the subsequent target parameter estimation. The performance of various advanced adaptive receiver filter designs in providing range-Doppler images with both low sidelobe levels and high accuracy will be investigated. We want to compare the sparsity of the range-Doppler images obtained from these various methods and their computational complexities to decide the most appropriate method for the MCAS application. Moreover, the implementation of the MCAS system facilitates the target tracking. The length of the CPI can be adjusted to determine how often we would like to track the target and the detailed target maneuver can be monitored with a rather short CPI. In a nutshell, the design of the probing sequence set and its corresponding receiver filter for an MCAS system form the focus of my future work.

APPENDIX A
THE DERIVATION OF THE DOPPLER SCALING FACTOR

The transmitted signal is reflected from the n^{th} transmitter to the m^{th} receiver by the q^{th} moving target, and thus the Doppler scaling factor between the signal transmitted from the n^{th} transmitter and the one received at the m^{th} receiver can be represented as [93, 101]:

$$\alpha_{n,q,m} = \frac{c + v_s^t(n)}{c - v_t(n)} \times \frac{c + v_r(m)}{c - v_t^r(m)}, \tag{A–1}$$

where $v_s^t(n)$ is the velocity of the target relative to the n^{th} transmitter, and $v_t^r(m)$ is that of the m^{th} receiver relative to the target. In addition, $v_t(n)$ and $v_r(m)$ are the velocities of the n^{th} transmitter and m^{th} receiver, respectively.

Define the phase angle of the target velocity vector $\mathbf{v}_q = [x_q^v, y_q^v]^T$ as $\psi_q = \arctan(y_q^v / x_q^v)$, we can represent $v_s^t(n)$ and $v_t^r(m)$ as $v_s^t(n) = \|\mathbf{v}_q\| \cos(\phi_{q,n} - \psi_q)$ and $v_t^r(m) = \|\mathbf{v}_q\| \cos(\psi_q - \varphi_{q,m})$, respectively. In addition, $v_t(n)$ and $v_r(m)$ equal zero since both the transmitter and receiver are stationary. Therefore, the Doppler scaling factor $\alpha_{n,q,m}$ can be rewritten as:

$$\begin{aligned}
\alpha_{n,q,m} &= \frac{c + v_s^t(n)}{c - v_t^r(m)} \\
&= \frac{c + \sqrt{(x_q^v)^2 + (y_q^v)^2} \cos(\phi_{q,n} - \psi_q)}{c - \sqrt{(x_q^v)^2 + (y_q^v)^2} \cos(\psi_q - \varphi_{q,m})} \\
&= \frac{c + \sqrt{(x_q^v)^2 + (y_q^v)^2} \cos\psi_q \cos\phi_{q,n} + \sqrt{(x_q^v)^2 + (y_q^v)^2} \sin\psi_q \sin\phi_{q,n}}{c - \sqrt{(x_q^v)^2 + (y_q^v)^2} \cos\psi_q \cos\varphi_{q,m} - \sqrt{(x_q^v)^2 + (y_q^v)^2} \sin\psi_q \sin\varphi_{q,m}} \\
&= \frac{c + x_q^v \cos\phi_{q,n} + y_q^v \sin\phi_{q,n}}{c - x_q^v \cos\varphi_{q,m} - y_q^v \sin\varphi_{q,m}}.
\end{aligned} \tag{A–2}$$

APPENDIX B
THE DERIVATION OF THE WEIGHT MATRIX

For ease of exposition, we assume that in the said active sonar system, there are two transmitters, two receivers, and one moving target. Based on the signal model in Section 3.2, the received signal $y_1(t)$ and $y_2(t)$ at the 1^{st} and 2^{nd} receivers can be represented in an unstructured model as:

$$\begin{aligned} y_1(t) &= \kappa_{1,1,1}s_1(\alpha_{1,1,1}(t-\tau_{1,1,1})) + \kappa_{2,1,1}s_2(\alpha_{2,1,1}(t-\tau_{2,1,1})) \\ &\quad +\kappa_{1,1}s_1(t-\tau_{1,1}) + \kappa_{2,1}s_2(t-\tau_{2,1}) + e_1(t), \end{aligned} \tag{B–1}$$

and

$$\begin{aligned} y_2(t) &= \kappa_{1,1,2}s_1(\alpha_{1,1,2}(t-\tau_{1,1,2})) + \kappa_{2,1,2}s_2(\alpha_{2,1,2}(t-\tau_{2,1,2})) \\ &\quad +\kappa_{1,2}s_1(t-\tau_{1,2}) + \kappa_{2,2}s_2(t-\tau_{2,2}) + e_2(t), \end{aligned} \tag{B–2}$$

respectively, where the parameter vector of the unstructured model is

$$\begin{aligned} \Theta_1 = [&\mathrm{Re}\{\kappa_{1,1,1}\}, \mathrm{Im}\{\kappa_{1,1,1}\}, \mathrm{Re}\{\kappa_{2,1,1}\}, \mathrm{Im}\{\kappa_{2,1,1}\}, \mathrm{Re}\{\kappa_{1,1,2}\}, \mathrm{Im}\{\kappa_{1,1,2}\}, \mathrm{Re}\{\kappa_{2,1,2}\}, \\ &\mathrm{Im}\{\kappa_{2,1,2}\}, \mathrm{Re}\{\kappa_{1,1}\}, \mathrm{Im}\{\kappa_{1,1}\}, \mathrm{Re}\{\kappa_{2,1}\}, \mathrm{Im}\{\kappa_{2,1}\}, \mathrm{Re}\{\kappa_{1,2}\}, \mathrm{Im}\{\kappa_{1,2}\}, \mathrm{Re}\{\kappa_{2,2}\}, \\ &\mathrm{Im}\{\kappa_{2,2}\}, \alpha_{1,1,1}, \alpha_{2,1,1}, \alpha_{1,1,2}, \alpha_{2,1,2}, \tau_{1,1}, \tau_{2,1}, \tau_{1,2}, \tau_{2,2}, \tau_{1,1,1}, \tau_{2,1,1}, \tau_{1,1,2}, \tau_{2,1,2}]^T \end{aligned} \tag{B–3}$$

In the sampled discrete form, (B–1) and (B–2) can be represented as

$$y_1(k) = \mu_1(k) + e_1(k), \tag{B–4}$$

and

$$y_2(k) = \mu_2(k) + e_2(k), \tag{B–5}$$

respectively, for $k = 1, 2, \ldots K$, where

$$\begin{aligned} \mu_1(k) &= \kappa_{1,1,1}s_1(\alpha_{1,1,1}(k-k_{1,1,1})) + \kappa_{2,1,1}s_2(\alpha_{2,1,1}(k-k_{2,1,1})) \\ &\quad +\kappa_{1,1}s_1(k-k_{1,1}) + \kappa_{2,1}s_2(k-k_{2,1}), \end{aligned} \tag{B–6}$$

and

$$\begin{aligned}\mu_2(k) &= \kappa_{1,1,2}s_1(\alpha_{1,1,2}(k-k_{1,1,2}))+\kappa_{2,1,2}s_2(\alpha_{2,1,2}(k-k_{2,1,2}))\\ &\quad +\kappa_{1,2}s_1(k-k_{1,2})+\kappa_{2,2}s_2(k-k_{2,2}).\end{aligned} \tag{B–7}$$

In (B–4) and (B–5), K is the length of the received measurements and $s(k) = s(t)|_{t=kT}$ (T is the sampling period). We assume that $\mathrm{E}[\mathbf{e}_i\mathbf{e}_i^H] = \sigma^2\mathbf{I}$, for $i = 1$ and 2. According to the Slepian-Bangs formula [102], the FIM is given as follows:

$$\mathbf{F}_{\Theta_1} = \frac{2K}{\sigma^2}\mathrm{Re}\left\{\sum_{i=1}^{2}\sum_{k=1}^{K} D_{i,k}^H(\Theta_1)D_{i,k}(\Theta_1)\right\}, \tag{B–8}$$

where

$$D_{i,k}(\Theta_1) = \frac{\partial\mu_i(k)}{\Theta_1^T}, \quad \text{for} \quad i = 1, 2, \quad \text{and} \quad k = 1, 2, \ldots, K. \tag{B–9}$$

Since the true values of Θ_1 is unavailable in the actual implementation, we replace them with the estimates obtained from the range-Doppler imaging step. The sequences $s_1(k)$ and $s_2(k)$ are known at the receiver sides.

Once the approximate FIM is obtained, we extract the 4×4 block of $\mathbf{F}_{\Theta_1}$ related to $\{\tau_{1,1,1}, \tau_{2,1,1}, \tau_{1,1,2}, \tau_{2,1,2}\}$ as the weighting matrix $\mathbf{W}_1$, and the block with size 4×4 corresponding to $\{\alpha_{1,1,1}, \alpha_{2,1,1}, \alpha_{1,1,2}, \alpha_{2,1,2}\}$ as $\mathbf{W}_2$.

We finally remark that by plugging (3–4) and (3–5) into (B–1) and (B–2), which are functions of $\{\tau_{1,1,1}, \tau_{2,1,1}, \tau_{1,1,2}, \tau_{2,1,2}\}$ and $\{\alpha_{1,1,1}, \alpha_{2,1,1}, \alpha_{1,1,2}, \alpha_{2,1,2}\}$, the so-obtained equations become functions of $\{x_1^\theta, y_1^\theta, x_1^v, y_1^v\}$ and are referred to as the structured model. Therefore, the corresponding parameter vector of this structured model is

$$\begin{aligned}\Theta_2 &= [\mathrm{Re}\{\kappa_{1,1,1}\}, \mathrm{Im}\{\kappa_{1,1,1}\}, \mathrm{Re}\{\kappa_{2,1,1}\}, \mathrm{Im}\{\kappa_{2,1,1}\}, \mathrm{Re}\{\kappa_{1,1,2}\}, \mathrm{Im}\{\kappa_{1,1,2}\}, \mathrm{Re}\{\kappa_{2,1,2}\},\\ &\quad \mathrm{Im}\{\kappa_{2,1,2}\}, \mathrm{Re}\{\kappa_{1,1}\}, \mathrm{Im}\{\kappa_{1,1}\}, \mathrm{Re}\{\kappa_{2,1}\}, \mathrm{Im}\{\kappa_{2,1}\}, \mathrm{Re}\{\kappa_{1,2}\}, \mathrm{Im}\{\kappa_{1,2}\}, \mathrm{Re}\{\kappa_{2,2}\},\\ &\quad \mathrm{Im}\{\kappa_{2,2}\}, \tau_{1,1}, \tau_{2,1}, \tau_{1,2}, \tau_{2,2}, x_1^\theta, y_1^\theta, x_1^v, y_1^v]^T.\end{aligned} \tag{B–10}$$

REFERENCES

[1] M. Stojanovic and J. Preisig, "Underwater acoustic communication channels: Propagation models and statistical characterization," *IEEE Communications Magazine*, vol. 47, no. 1, pp. 84–89, January 2009.

[2] D. Tse and P. Viswanath, *Fundamentals of Wireless Communication*, Cambridge University Press, New York, NY, 2005.

[3] J. Preisig, "Acoustic propagation considerations for underwater acoustic communications network development," *SIGMOBILE Mobile Computing Communications Review*, vol. 11, no. 4, pp. 2–10, 2007.

[4] J. Catipovic, "Performance limitations in underwater acoustic telemetry," *IEEE Journal of Oceanic Engineering*, vol. 15, no. 3, pp. 205–216, July 1990.

[5] W. Li and J. C. Preisig, "Estimation of rapidly time-varying sparse channels," *IEEE Journal of Oceanic Engineering*, vol. 32, no. 4, pp. 927–939, October 2007.

[6] W. Li, "Estimation and tracking of rapidly time-varying broadband acoustic communication channels," *PhD thesis*, Massachusetts Institute of Technology, Cambridge, MA, 2005.

[7] N. Weste, M. Bickerstaff, T. Arivoli, P. J. Ryan, J. W. Dalton, D. J. Skellern, and T. M. Percival, "A 50 MHz 16-point FFT processor for WLAN applications," *Proceedings of the IEEE 1997 Custom Integrated Circuits Conference*, pp. 457–460, May 1997.

[8] H. Wang and L. Cai, "On adaptive multiband signal detection with GLR algorithm," *IEEE Transactions on Aerospace and Electronic Systems*, vol. 27, pp. 225–233, Mar. 1991.

[9] M. Wax, "Detection and estimation of superimposed signals," March, 1985.

[10] D. Kilfoyle, J. C. Preisig, and A. B. Baggeroer, "Spatial modulation experiments in the underwater acoustic channel," *IEEE Journal of Oceanic Engineering*, vol. 30, no. 2, pp. 406–415, April 2005.

[11] B. Li, S. Zhou, M. Stojanovic, L. Freitag, and P. Willett, "Multicarrier communication over underwater acoustic channels with nonuniform Doppler shifts," *IEEE Journal of Oceanographic Engineering*, vol. 33, no. 2, pp. 198–209, April 2008.

[12] J. Ling, T. Yardibi, X. Su, H. He, and J. Li, "Enhanced channel estimation and symbol detection for high speed multi-input multi-ouput underwater acoustic communications," *Journal of Acoustic Society of America*, vol. 125, no. 5, pp. 3067–3078, May 2009.

[13] J. Ling, X. Tan, T. Yardibi, J. Li, H. He, and M. L. Nordenvaad, "Enhanced channel estimation and efficient symbol detection in MIMO underwater acoustic

communications," in *43th Asilomar Conference on Signals, Systems and Computers*, Pacific Grove, CA, November 1-4, 2009.

[14] M. Stojanovic, J. Catipovic, and J. Proakis, "Phase coherent digital communications for underwater acoustic channels," *IEEE Journal of Oceanic Engineering*, vol. 19, no. 1, pp. 100–111, January 1994.

[15] M. Stojanovic, L. Freitag, and M. Johnson, "Channel-estimation-based adaptive equalization of underwater acoustic signals," *IEEE/MTS Oceans Conference*, vol. 2, pp. 985–990, September 1999.

[16] A. Song, M. Badiey, and V. K. McDonald, "Multichannel combining and equalization for underwater acoustic MIMO channels," *in Proceedings of MTS/IEEE Oceans conference,* Quebec City, Canada, September 2008.

[17] S. Gray, J. Preisig, and D. Brady, "Multiuser detection in a horizontal underwater acoustic channel using array observations," *IEEE Journal of Oceanic Engineering*, vol. 21, no. 3, pp. 148–160, January 1997.

[18] P. W. Wolniansky, G. J. Foschini, G. D. Golden, and R. A. Valenzuela, "V-blast: An architecture for realizing very high data rates over the rich-scattering wireless channel," *Proc. ISSSE-98*, Sept. 29, 1998.

[19] R. L. Cupo, G. D. Golden, C. C. Martin, K. L. Sherman, N. R. Sollenberger, J. H. Winters, and P. W. Wolniansky, "A four-element adaptive antenna array for IS-136 PCS base stations," *47th IEEE Vehicular Technology Conference*, vol. 3, pp. 1577–1581, May 1997.

[20] J. Li and P. Stoica, "Efficient mixed-spectrum estimation with applications to target feature extraction," *IEEE Transactions on Signal Processing*, vol. 44, pp. 281–295, February 1996.

[21] J. Ling, K. Zhao, J. Li, and M. L. Nordenvaad, "Multi-input multi-output underwater communications over sparse and frequency modulated acoustic channels," *Journal of the Acoustical Society of America*, vol. 130, pp. 249–262, July 2011.

[22] M. Tuchler, A. Singer, and R. Koetter, "Minimum mean squared error equalization using a prior information," *IEEE Transactions on Signal Processing*, vol. 50, no. 3, pp. 673–682, March 2002.

[23] M. Tuchler, R. Koetter, and A. Singer, "Turbo equalization: principles and new results," *IEEE Transactions on Communications*, vol. 50, no. 5, pp. 754–767, May 2002.

[24] R. Koetter, A. Singer, and M. Tuchler, "Turbo equalization," *IEEE Signal Processing Magazine*, vol. 21, no. 1, pp. 67–80, January 2004.

[25] K. Zhao, J. Ling, and J. Li, "On estimating sparse and frequency modulated channels for MIMO underwater acoustic communications," *Proceedings of*

49th Annual Allerton Conference on Communication, Control, and Computing, Monticello, IL, pp. 15–22, September 2011.

[26] M. Lundberg and T. Oberg, "Iterative reception for acoustic underwater MIMO communications," *in Proceedings of MTS/IEEE Oceans conference,* Boston, USA, September 2006.

[27] S. Roy, T. Duman, V. McDonald, and J. Proakis, "High-rate communication for underwater acoustic channels using multiple transmitters and space-time coding: Receiver structures and experimental results," *IEEE Journal of Oceanic Engineering*, vol. 32, pp. 663–688, July 2007.

[28] P. Robertson, E. Villebrun, and P. Hoeher, "A comparison of optimal and sub-optimal MAP decoding algorithms operating in the log domain," *IEEE International Conference on Communications,* Seattle, WA, pp. 1009–1013, June 1995.

[29] C. Douillard, C. M. Jezequel, C. Berrou, A. Picart, P. Didier, and A. Glavieux, "Iterative correction of intersymbol interference: Turbo-equalization," *European Transactions on Telecommunications*, vol. 6, pp. 507–511, September 1995.

[30] J. Ling, H. He, P. Stoica, J. Li, and W. Roberts, "Covert underwater acoustic communications," *Journal of Acoustic Society of America*, vol. 128, pp. 2898–2909, November 2010.

[31] B. S. Sharif, O. H. J. Neasham, and A. E. Adams, "A computationally efficient Doppler compensation system for underwater acoustic communications," *IEEE Journal of Oceanic Engineering*, vol. 25, no. 1, pp. 52–61, January 2000.

[32] P. Beaujean and L. R. LeBlanc, "Adaptive array processing for high-speed acoustic communications in shallow water," *IEEE Journal of Oceanic Engineering*, vol. 29, no. 3, pp. 807–823, July 2004.

[33] S. L. Miller and R. J. O'Dea, "Peak power and bandwidth efficient linear modulation," *IEEE Transactions on Communications*, vol. 46, no. 12, pp. 1639–1648, December 1998.

[34] J. A. Högbom, "Aperture synthesis with a non-regular distribution of interferometer baselines," *Astronomy and Astrophysics Supplements*, vol. 15, pp. 417–426, 1974.

[35] J. C. Preisig, "Performance analysis of adaptive equalization for coherent acoustic communications in the time-varying ocean environment," *Journal of the Acoustical Society of America*, vol. 118, no. 1, pp. 263–278, July 2005.

[36] H. He, D. Vu, P. Stoica, and J. Li, "Construction of unimodular sequence sets for periodic correlations," *2009 Asilomar Conference on Signals, Systems and Computers,* Pacific Grove, CA, November 1-4, 2009.

[37] T. Yardibi, J. Li, P. Stoica, M. Xue, and A. B. Baggeroer, "Source localization and sensing: A nonparametric iterative adaptive approach based on weighted least squares," *IEEE Transactions on Aerospace and Electronic Systems*, vol. 46, no. 1, pp. 425–443, Jan. 2010.

[38] W. I. Zangwill, *Nonlinear Programming: A Unified Approach*, Prentice-Hall, Inc., Englewood Cliffs, NJ 07632, 1969.

[39] N. Wiener, *Extrapolation, Interpolation, and Smoothing of Stationary Time Series*, Wiley, New York, NY, 1949.

[40] R. J. McEliece, D. J. C. MacKay, and J.-F. Cheng, "Turbo decoding as an instance of Pearl's "Belief Propagation" algorithm," *IEEE JOURNAL ON SELECTED AREAS IN COMMUNICATIONS*, vol. 16, no. 2, pp. 140–152, February 1998.

[41] J. Ling, X. Tan, J. Li, and M. L. Nordenvaad, "Efficient channel equalization for MIMO underwater acoustic communications," *Proceedings of 6th Sensor Array and Multichannel Signal Processing Workshop,* Ma'ale Hahamisha, Israel, pp. 73–76, October 2010.

[42] M. Swift, J. Riley, S. Lourey, and L. Booth, "An overview of the multistatic sonar program in Australia," *Proc. Int. Symp. on Signal Processing and its Applications,* Brisbane, Australia, pp. 321–324, August 1999.

[43] H. Cox, "Fundamentals of bistatic active sonar," *Proceedings of the NATO Advanced Study Institute on Underwater Acoustic Data Processing,* Kingston, Canada, pp. 3–24, July 1988.

[44] W. C. Knight, R. G. Pridham, and S. M. Kay, "Digital signal processing for sonar," *Proceedings of the IEEE*, vol. 69, no. 11, pp. 1451–1507, November 1981.

[45] N. Levanon and E. Mozeson, *Radar Signals*, Wiley, NY, 2004.

[46] S. Coraluppi, D. Grimmett, and P. de Theije, "Benchmark evaluation of multistatic trackers," *9th International Conference on Information Fusion,* Florence, Italy, pp. 1–7, July 2006.

[47] X. Tan, W. Roberts, J. Li, and P. Stoica, "Sparse learning via iterative minimization with application to MIMO radar imaging," *IEEE Transactions on Signal Processing*, vol. 59, no. 3, pp. 1088–1101, March 2011.

[48] K. R. Pattipati, S. Deb, Y. Bar-Shalom, and R. B. J. Washburn, "A new relaxation algorithm and passive sensor data association," *IEEE Transactions on Automatic Control*, vol. 37, no. 2, pp. 198–213, February 1992.

[49] E. D. Kaplan and C. J. Hegarty, "Understanding GPS: principles and applications," *(Artech House Mobile Communications, Norwood, MA)*, pp. 1–726, 2006.

[50] J. Ling, T. Yardibi, X. Su, H. He, and J. Li, "Enhanced channel estimation and symbol detection for high speed multi-input multi-output underwater acoustic communications," *Journal of the Acoustical Society of America*, vol. 125, no. 5, pp. 3067–3078, May 2009.

[51] W. Roberts, P. Stoica, J. Li, T. Yardibi, and F. A. Sadjadi, "Iterative adaptive approaches to MIMO radar imaging," *IEEE Journal of Selected Topics in Signal Processing*, vol. 4, no. 1, pp. 5–20, Feb. 2010.

[52] G. Schwarz, "Estimating the dimension of a model," *The Annals of Statistics*, vol. 6, pp. 461–464, May 1978.

[53] P. Stoica and Y. Selén, "Cyclic minimizers, majorization techniques, and expectation-maximization algorithm: A refresher," *IEEE Signal Processing Magazine*, pp. 112–114, January 2004.

[54] S. P. Lloyd, "Least squares quantization in PCM," *IEEE Transactions on Information Theory*, vol. 28, no. 2, pp. 129–137, March 1982.

[55] A. L. Swindlehurst and P. Stoica, "Maximum likelihood methods in radar array signal processing," *Proceedings of the IEEE*, vol. 86, pp. 421–441, February 1998.

[56] H. L. Van Trees, *Optimum Array Processing: Part IV of Detection, Estimation, and Modulation Theory*, John Wiley & Sons, New York, NY, 2002.

[57] J. G. Proakis, *Digital Communications*, McGraw-Hill Inc., third edition, 1995.

[58] T. Yardibi, J. Li, P. Stoica, and L. N. Cattafesta, "Sparsity constrained deconvolution approaches for acoustic source mapping," *The Journal of the Acoustical Society of America*, vol. 123, no. 5, pp. 2631–2642, May 2008.

[59] R. Roy and T. Kailath, "Esprit – estimation of signal parameters via rotational invariance techniques," *IEEE Transactions on Acoustics, Speech, and Signal Processing*, vol. ASSP-37, no. 7, pp. 984–995, July 1989.

[60] A. Ruiz, J. M. Cioffi, and S. Kasturia, "Discrete multiple tone modulation with coset coding for the spectrally shaped channel," *IEEE Transactions on Communications*, vol. 40, no. 6, pp. 1012–1029, June 1992.

[61] N. Al-Dhahir, "Single-carrier frequency-domain equalization for space-time block-coded transmissions over frequency-selective fading channels," *IEEE Communications Letters*, vol. 5, no. 7, pp. 304–306, July 2001.

[62] A. B. Baggeroer and H. Cox, "Passive sonar limits upon nulling multiple moving ships with large aperture arrays," *33th Asilomar Conference on Signals, Systems and Computers*, vol. 1, pp. 103–108, 1999.

[63] A. Baggeroer, W. Kuperman, and P. Mikhalevsky, "An overview of matched field methods in ocean acoustics," *IEEE Journal of Oceanic Engineering*, vol. 18, no. 4, pp. 401–424, October 1993.

[64] A. B. Gershman and M. G. Amin, "Wideband direction-of-arrival estimation of multiple chirp signals using spatial time-frequency distributions," *IEEE Signal Processing Letters*, vol. 7, no. 6, pp. 152–155, June 2000.

[65] H. Wang and M. Kaveh, "Coherent signal-subspace processing for the detection and estimation of angles of arrival of multiple wide-band sources," *IEEE Transactions on Acoustics, Speech, and Signal Processing*, vol. ASSP-33, no. 4, pp. 823–831, August 1985.

[66] P. Stoica, P. Babu, and J. Li, "SPICE: A sparse covariance-based estimation method for array processing," *IEEE Transactions on Signal Processing*, vol. 59, no. 2, pp. 629–638, Feb 2011.

[67] D. L. Donoho and M. Elad, "Optimally sparse representation in general (nonorthogonal) dictionaries via ℓ^1 minimization," *Proceedings of the National Academy of Sciences of the United States of America*, vol. 100, no. 5, pp. 2197–2202, March 2003.

[68] I. F. Gorodnitsky and B. D. Rao, "Sparse signal reconstruction from limited data using FOCUSS: A re-weighted minimum norm algorithm," *IEEE Transactions on Signal Processing*, vol. 45, no. 3, pp. 600–616, 1997.

[69] J. A. Tropp, "Just relax: Convex programming methods for identifying sparse signals," *IEEE Transactions on Information Theory*, vol. 51, no. 3, pp. 1030–1051, March 2006.

[70] D. Malioutov, M. Cetin, and A. Willsky, "A sparse signal reconstruction perspective for source localization with sensor arrays," *IEEE Transactions on Signal Processing*, vol. 53, no. 8, pp. 3010–3022, Aug. 2005.

[71] F. Classen and H. Meyr, "Frequency synchronization algorithms for OFDM systems suitable for communication over frequency selective fading channels," *IEEE 44th Vehicular Technology Conference,*Stockholm, Sweden, pp. 1655–1659, June 1994.

[72] S. Suthaharan, A. Nallanathan, and B. Kannan, "Space-time coded MIMO-OFDM for high capacity and high data-rate wireless communication over frequency selective fading channels," *4th International Workshop on Mobile and Wireless Communications Network, 2002*, pp. 424–428, September 2002.

[73] P. T. Boufounos, P. Smaragdis, and B. Raj, "Joint sparsity models for sideband array processing," *SPIE Wavelets and Sparsity XIV,* San Diego, CA, 2011.

[74] D. Needell and J. Tropp, "CoSaMP: Iterative signal recovery from incomplete and inaccurate samples," *Applied and Computational Harmonic Analysis*, vol. 26, pp. 301–321, May 2009.

[75] D. Vu, L. Xu, M. Xue, and J. Li, "Nonparametric missing sample spectral analysis and its applications to interrupted SAR," *IEEE Journal of Selected Topics in Signal Processing*, vol. 6, no. 1, pp. 1–14, Feb 2012.

[76] Z.-M. Liu, Z.-T. Huang, and Y.-Y. Zhou, "Direction-of-arrival estimation of wideband signals via covariance matrix sparse representation," *IEEE Transcations on Signal Processing*, vol. 59, no. 9, pp. 4256–4270, September 2011.

[77] M. Yuan and Y. Lin, "Model selection and estimation in regression with grouped variables," *Journal of the Royal Statistical Society: Series B (Statistical Methodology)*, vol. 68, no. 1, pp. 49–57, February 2005.

[78] W. J. Fu, "Penalized regressions: The bridge versus the lasso," *Journal of Computational and Graphical Statistics*, vol. 7, no. 3, pp. 397–416, February 1998.

[79] F. R. Bach, "Consistency of the group lasso and multiple kernel learning," *The Journal of Machine Learning Research*, vol. 9, no. 6, pp. 1179–1225, June 2008.

[80] X. Lv, G. Bi, and C. Wan, "The group lasso for stable recovery of block-sparse signal representations," *IEEE Transactions on Signal Processing*, vol. 59, no. 4, pp. 1371–1381, April 2011.

[81] E. Appleton, "Automatic synchronization of triode oscillators," *Proc. Cambridge Phil. Soc.*, vol. 21, pp. 231–248, 1922–1923.

[82] G. Hsieh and J. Hung, "Phase-locked loop techniques-a survey," *IEEE Transactions on Industrial Electronics*, vol. 43, pp. 609–615, December 1996.

[83] A. Nehorai and E. Paldi, "Acoustic vector-sensor array processing," *IEEE Transactions on Signal Processing*, vol. 42, no. 9, pp. 2481–2491, Sep 1994.

[84] M. Hawkes and A. Nehorai, "Acoustic vector-sensor beamforming and Capon direction estimation," *IEEE Transactions on Signal Processing*, vol. 46, no. 9, pp. 2291–2304, Sep 1998.

[85] A. J. Poulsen, "Robust vector sensor array processing and performance analysis," *Ph.D. dissertation, Massachusetts Institute of Technology, Boston, Massachusetts*, 2009.

[86] M. Hyder and K. Mahata, "Direction-of-arrival estimation using a mixed $l_{2,0}$ norm approximation," *IEEE Transactions on Signal Processing*, vol. 58, no. 9, pp. 4646–4655, Sept. 2010.

[87] J. Huang, "Structured sparsity: Theorems, algorithms and applications," *Ph.D. dissertation, The State University of New Jersey, New Brunswick, New Jersey*, 2011.

[88] Y. C. Eldar, P. Kuppinger, and H. Bölcskei, "Block-sparse signals: Uncertainty relations and efficient recovery," *IEEE Transactions on Signal Processing*, vol. 58, no. 6, pp. 3042–3054, June 2010.

[89] M. E. Tipping, "Sparse Bayesian learning and the relevance vector machine," *Journal of Machine Learning Research*, vol. 1, pp. 211–244, 2001.

[90] J. Li, P. Stoica, and D. Zheng, "Angle and waveform estimation via RELAX," *IEEE Transactions on Aerospace and Electronic Systems*, vol. 33, pp. 1077–1087, July 1997.

[91] J. A. Nelder and R. Mead, "A simplex method for function minimization," *Computer Journal*, vol. 7, pp. 308–313, 1965.

[92] P. Stoica and A. Nehorai, "MUSIC, maximum likelihood, and Cramer-Rao bound," *IEEE Transactions on Acoustics, Speech, and Signal Processing*, vol. ASSP-37, no. 5, pp. 720–741, May 1989.

[93] S. Coraluppi, "Multistatic sonar localization," *IEEE Journal of Oceanic Engineering*, vol. 31, no. 4, pp. 964–974, October 2006.

[94] Richardson, J. Greene, Malme, and Thomson, *Marine Mammals and Noise*, Academic Press, 1998.

[95] H. A. DeFerrari, H. B. Nguyen, and A. Rogers, "Continuous active pulse compression sonar," *Proceedings of the International Conference Underwater Acoustic Measurements: Technologies and Results*, pp. 1–8, June 2005.

[96] R. van Vossen, S. P. Beerens, and I. E. van der Spek, "Anti-submarine warfare with continuously active sonar," *Sea Technology Magazine*, pp. 33–35, November 2005.

[97] W. Roberts, H. He, J. Li, and P. Stoica, "Probing waveform synthesis and receiver filter design," *IEEE Signal Processing Magazine*, vol. 27, no. 4, pp. 99–112, July 2010.

[98] H. He, J. Li, and P. Stoica, *Waveform Design for Active Sensing Systems – A computational approach*, Cambridge University Press, 2012.

[99] D. Kilfoyle and A. Baggeroer, "The state of the art in underwater acoustic telemetry," *IEEE Journal of Oceanic Engineering*, vol. 25, pp. 4–27, January 2000.

[100] A. B. MacKenzie and L. A. DaSilva, "Application of signal processing to address wireless data demand," *IEEE Signal Processing Magazine*, vol. 29, no. 6, pp. 166–168, 2012.

[101] H. Cox, "Fundamentals of bistatic active sonar," *Proc. NATO Advanced Study Inst. Underwater Acoustic Data Process.*, 1989.

[102] H. L. Van Trees, *Detection, Estimation, and Modulation Theory, Part I*, John Wiley and Sons, Inc., New York, NY, 1968.

BIOGRAPHICAL SKETCH

Kexin Zhao received the degree of Bachelor of Science from the University of Science and Technology of China, Hefei, China, in 2009, and the degree of Master of Science from University of Florida, Gainesville, FL, in 2009, both in electrical engineering. He will graduate with the degree of Doctor of Philosophy from the Department of Electrical and Computer Engineering at University of Florida in May, 2014. His research interests include signal processing and its application to multi-input multi-output underwater acoustic communications and multistatic active sonar systems.